COMPOSANTES RYTHMIQUE ET APÉRIODIQUE DE L'ACTIVITÉ CÉRÉBRALE PENDANT LE SOMMEIL

par

Michael-Christopher FOTI

THÈSE PAR ARTICLES PRÉSENTÉE À L'ÉCOLE DE TECHNOLOGIE SUPÉRIEURE COMME EXIGENCE PARTIELLE À L'OBTENTION DU DOCTORAT EN GÉNIE
Ph. D.

MONTRÉAL, LE 31 MARS 2026

ÉCOLE DE TECHNOLOGIE SUPÉRIEURE
UNIVERSITÉ DU QUÉBEC

PRÉSENTATION DU JURY

CETTE THÈSE A ÉTÉ ÉVALUÉE

PAR UN JURY COMPOSÉ DE :

M. Jean-Marc Lina, directeur de thèse
Département de génie électrique à l'École de technologie supérieure

Mme Rebecca Robillard, codirectrice de thèse
École de psychologie à l'Université d'Ottawa

Mme Nicolas Hagemeister, présidente du jury
Département de génie des systèmes à l'École de technologie supérieure

M. Mohamad Forouzanfar, membre du jury
Département de génie des systèmes à l'École de technologie supérieure

M. Karim Jerbi, examinateur externe
Département de psychologie à l'Université de Montréal

ELLE A FAIT L'OBJET D'UNE SOUTENANCE DEVANT JURY ET PUBLIC

LE 20 MARS 2026

À L'ÉCOLE DE TECHNOLOGIE SUPÉRIEURE

REMERCIEMENTS

Je tiens à exprimer ma profonde gratitude à mon directeur de thèse, Jean-Marc, ainsi qu'à ma co-directrice de thèse, Rebecca, pour leur soutien constant et leurs précieux conseils tout au long de mon parcours. Toujours disponibles et bienveillants, leurs contributions dépassent largement le cadre de mon doctorat et continueront à m'accompagner bien au-delà de cette thèse. Je tiens également à remercier Jonathan Dubé et David Smith pour leur aide et leur soutien constant tout au long de la réalisation de cette thèse.

COMPOSANTES RYTHMIQUE ET APÉRIODIQUE DE L'ACTIVITÉ CÉRÉBRALE PENDANT LE SOMMEIL

Michael-Christopher FOTI

RÉSUMÉ

Les enregistrements d'électroencéphalographie (EEG) pendant le sommeil sont une source importante d'informations sur l'activité cérébrale, permettant de caractériser de nombreux processus cognitifs liés au sommeil et plus généralement, à la santé d'un individu. Les signaux de ces enregistrements résultent de la contribution de plusieurs processus spontanés, en particulier des rythmes transitoires et spectralement bien définis. Ils se superposent à un signal de fond omniprésent, appelé « activité apériodique ». Cette dernière suscite aujourd'hui un intérêt croissant, car elle fait l'objet d'une évaluation plus précise afin d'en faire un signal physiologique à valeur clinique, mais constitue aussi un obstacle à la caractérisation de propriétés propres aux rythmes.

Les méthodes actuelles qui séparent l'activité rythmique et apériodique sont limitées au domaine spectral et s'appliquent généralement à des signaux issus d'une seule électrode. Dans le cadre de cette thèse, des outils numériques ont été développés pour caractériser les activités rythmique et apériodique à différentes échelles spatiales, allant des enregistrements intracrâniens jusqu'aux séquences des topographies du potentiel sur le scalp. La première contribution consistait à développer une méthode de traitement du signal qui extrait un signal rythmique où l'activité apériodique est atténuée par filtrage. La validation de cet outil a été réalisée sur des enregistrements intracrâniens en NREM (non-Rapid Eye Movement). La deuxième contribution consistait à étendre l'application de cet outil aux enregistrements d'EEG du scalp, ce qui est nécessaire, étant donné qu'il s'agit d'une modalité non invasive, largement utilisée dans un contexte clinique. Au final, ces deux contributions offrent aujourd'hui un outil permettant d'obtenir un inventaire des rythmes à partir des signaux EEG sans activité apériodique. Enfin, la dernière contribution consistait à mesurer l'activité apériodique des topographies du scalp en s'appuyant sur l'analyse des micro-états.

L'ensemble des outils offre un cadre méthodologique innovant pour dissocier et analyser les composantes rythmiques et l'activité apériodique des signaux EEG. Ils visent à être intégrés dans un contexte clinique afin d'évaluer et de caractériser diverses pathologies et d'identifier des biomarqueurs fiables.

Mots-clés : électroencéphalographie, sommeil, rythmique, apériodique, analyse spectrale, ondelette, micro-états

RHYTHMIC AND APERIODIC COMPONENTS OF BRAIN ACTIVITIY DURING SLEEP

Michael-Christopher FOTI

ABSTRACT

Electroencephalography (EEG) recordings during sleep are an important source of information about brain activity, enabling characterization of many cognitive processes related to sleep and, more broadly, to an individual's health. The signals from these recordings result from the contributions of multiple spontaneous processes, in particular, transient rhythms with well-defined spectral characteristics. They are superimposed with a background signal, known as ‘aperiodic activity’. The latter is currently attracting growing interest, as it is being evaluated more precisely to establish its physiological relevance, but it also constitutes an obstacle to characterizing the intrinsic properties of the rhythms themselves.

Current methods for separating rhythmic and aperiodic activity are limited to the spectral domain and are typically applied to signals recorded from a single electrode. In this thesis, numerical tools were developed to characterize rhythmic and aperiodic activity across multiple spatial scales, ranging from intracranial recordings to sequences of scalp topographies. The first contribution consisted of developing a signal-processing method that extracts a rhythmic signal in which the aperiodic activity has been filtered out. The validation of this tool was carried out using intracranial recordings during NREM (non–rapid eye movement) sleep. The second contribution involved extending the application of this tool to scalp EEG recordings, which is necessary given that this modality is non-invasive and widely used in clinical settings. Together, these two contributions provide a tool for obtaining an inventory of rhythms without aperiodic activity. Finally, the last contribution consisted of measuring aperiodic activity in scalp topographies using microstate analysis.

Taken together, these tools provide an innovative methodological framework for disentangling and analyzing the rhythmic and aperiodic components of EEG signals. They are intended to be integrated into clinical settings to assess and characterize various pathologies and to identify reliable biomarkers.

Keywords: electroencephalography, sleep, rhythms, aperiodic, spectral analysis, wavelets, micro-states

TABLE DES MATIÈRES

Page

LISTE DES TABLEAUX

Page

LISTE DES FIGURES

LISTE DES ABRÉVIATIONS, SIGLES ET ACRONYMES

CEN	Central Executive Network
DMN	Default Mode Network
EEG	ÉlectroEncéphaloGraphie
EMD	Empirical Mode Decomposition
FastS	Fast Switchers
FFT	Fast Fourier Transform
fBm	Fractional Brownian Motion
fGm	Fractional Gaussian Motion
fMRI	Functional Magnetic Resonance Imaging
FOOOF	Fitting Oscillations & One-Over-F
GABA	Gamma-Aminobutyric Acid
GFP	Global Field Power
iEEG	ÉlectroEncéphaloGraphie Intracrânienne
IMF	Intrinsic Mode Function
IRASA	Irregular-Resampling Auto Spectral Analysis
MASS	Montreal Archive of Sleep Studies
MP	Matching Pursuit
NREM	Non Rapid Eye Movement
PAC	Phase Amplitude Coupling
PSG	PolySomnoGraphy
REM	Rapid Eye Movement

rFastS	Rhythmic Fast Switchers
RnB	Rhythms & Background
rPAC	Rhythmic Phase Amplitude Coupling
rSlowS	Rhythmic Slow Switchers
rSSW	Rhythmic Sleep Slow Wave
RSN	Resting State Network
rTB	Rhythmic Theta Burst
SlowS	Slow Switchers
SSW	Sleep Slow Wave
TB	Theta Burst

LISTE DES SYMBOLES ET UNITÉS DE MESURE

dB	Décibels
Hz	Hertz
µV	MicroVolt
mV	MilliVolt
f	Fréquence
s	Seconde
ψ	Ondellete
$\phi(t)$	Phase instantanée

INTRODUCTION

0.1 Le sommeil

Chez l'humain, une horloge interne d'environ 24 heures régule les fonctions biologiques. Ce rythme circadien influence le moment de l'endormissement en préparant l'organisme au repos, notamment par des variations de la température corporelle et par la sécrétion hormonale, notamment de la mélatonine (Czeisler & Gooley, 2007). Parmi les 24 heures régies par l'horloge circadienne, une partie est consacrée au sommeil, qui représente, en moyenne, sept à neuf heures par nuit chez l'adulte. Le sommeil est une période importante exigée par la physiologie humaine pour permettre à l'individu de bien fonctionner pendant la journée et, de façon générale, de maintenir un état de santé de qualité.

Outre les échelles de temps diurnes et nocturnes, le temps de sommeil présentes, dans son organisations, différentes échelles temporelles. Ainsi, au cours de la nuit, le sommeil s'organise en cycles, chacun comprenant une séquence de différentes phases d'activité cérébrale. Une nuit complète comporte entre 4 et 6 cycles, chacun d'une durée d'environ 90 minutes. Chaque cycle de sommeil est composé de quatre stades regroupés en deux types: le NREM (Non Rapid Eye Movement) et le REM (Rapid Eye Movement). Le stade NREM1 est un état transitionnel entre l'éveil et le sommeil et représente 5 % d'une nuit de sommeil (Patel, Reddy, Shumway, & Araujo, 2025) . Ce stade est suivi du sommeil léger (NREM 2), puis du sommeil profond (NREM 3), avant d'atteindre la phase REM.

Le sommeil profond domine durant le premier cycle et diminue progressivement au cours de la nuit, laissant plus de place au sommeil REM et NREM 2, qui dominent durant la seconde partie de la nuit. Finalement, le sommeil REM, également appelé sommeil paradoxal, est le stade durant lequel l'individu rêve. Au cours de ce stade, l'atonie musculaire empêche l'individu de bouger pendant ses rêves. Le REM est lui-même subdivisé en de courtes période phasiques et toniques. Le REM phasique se caractérise par des mouvements oculaires rapides, tandis que le REM tonique correspond à une période de calme, avec peu de mouvements oculaires.

Le sommeil présente donc différentes échelles de temps, de l'échelle circadienne aux échelles des stades et des phases, organisées dans une séquence appelée hypnogramme, qui représente l'architecture du sommeil d'un individu tel qu'illustré à la figure 0.1.

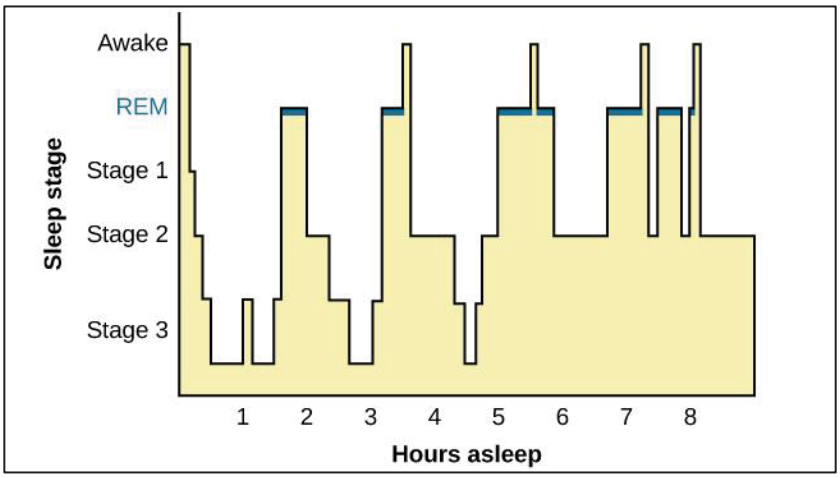

Figure 0.1 Architecture du sommeil
Tiré de McFarlane (2024)

Le sommeil est ainsi un moment privilégié pour mesurer l'activité cérébrale spontanée. Le corps étant au repos et privé de stimuli externes, le sommeil offre un cadre privilégié pour mesurer et comprendre plusieurs processus neuronaux essentiels au bon fonctionnement de l'individu à l'éveil. Il permet également de mesurer des biomarqueurs, par exemple, de la santé cérébrale susceptibles de mieux comprendre et de caractériser certaines conditions cliniques.

0.2 Les types d'enregistrement de l'activité cérébrale

La mesure de l'activité cérébrale peut être réalisée par électroencéphalographie (EEG), à l'aide d'un ensemble d'électrodes mesurant le potentiel électrique induit par l'activité bioélectrique des neurones. Ces électrodes peuvent être placées de façon invasive, c'est-à-dire de façon intracérébrale dans un contexte clinique (épilepsie), ou placées sur le scalp d'un individu. Ces électrodes mesurent l'activité du cerveau, composé de plusieurs milliards de neurones interconnectés. Les neurones sont composés de trois parties principales : le corps cellulaire (ou soma), les dendrites et l'axone. Le corps cellulaire contient les structures nécessaires à la survie

du neurone, dont le noyau, qui régule son fonctionnement. Les dendrites reçoivent les signaux envoyés par d'autres neurones via l'axone qui transmet ces signaux. Au bout de l'axone, on trouve les synapses qui assurent la transmission de signal électrique entre deux neurones.

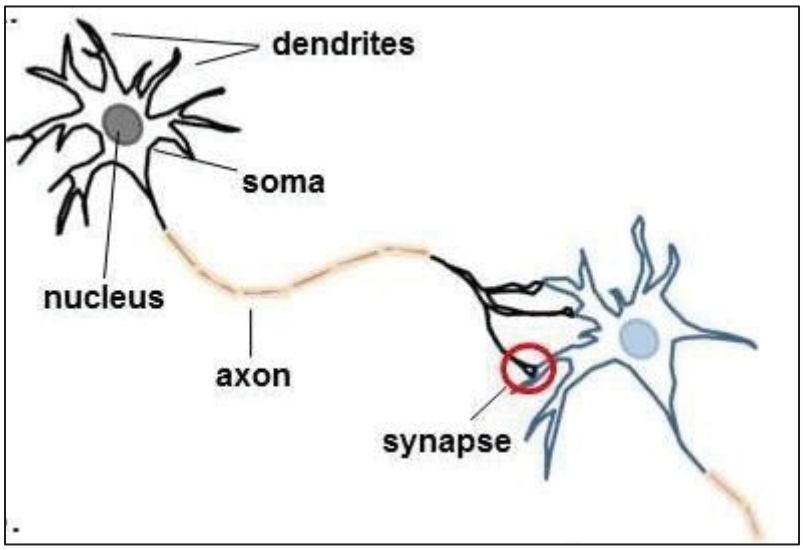

Figure 0.2 Structure illustrant deux neurones
Tiré de Ludwig et al. (2025)

0.2.1 iEEG intracrânien

Dans certaines situations cliniques, notamment dans le cadre de l'évaluation préchirurgicale de l'épilepsie focale, il est possible d'effectuer des enregistrements intracrâniens (iEEG). Ces enregistrements donnent accès à l'activité électrique cérébrale, généralement dans une région ciblée, soupçonnée de provoquer des crises. L'iEEG mesure le potentiel de champ local (LFP), qui reflète la somme des courants synaptiques synchrones, de l'ordre d'une centaine de millivolts, autour de l'électrode (voir Figure 0.3).

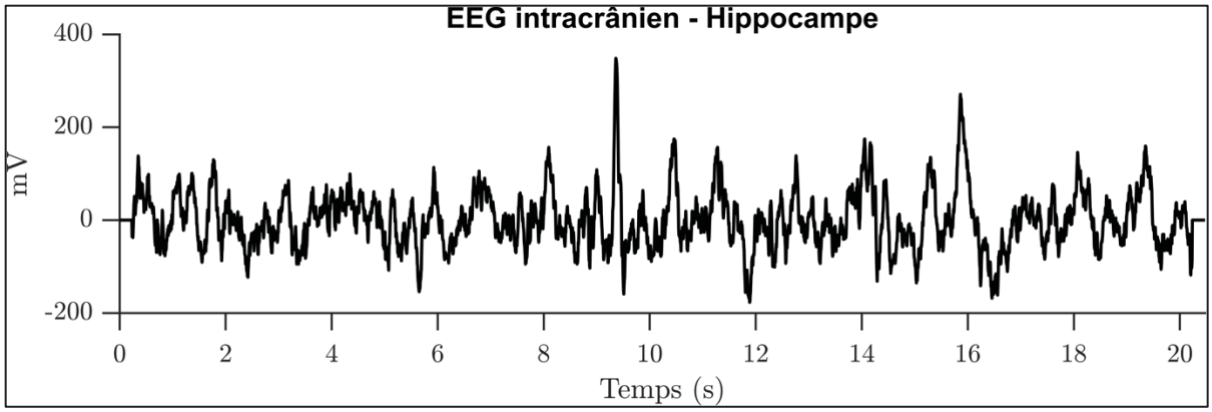

Figure 0.3 Exemple d'un signal intracrânien mesuré sur l'hippocampe

L'iEEG intracrânien offre une excellente résolution temporelle, mais la couverture spatiale est volontairement limitée. En effet, les électrodes sont placées de manière ciblée, en fonction de chaque patient et de la nature de la pathologie. Bien que ces mesures invasives soient obtenues dans un contexte clinique de l'épilepsie, elles peuvent capturer de l'activité cérébrale physiologiquement normale. Ces enregistrements peuvent alors être regroupés pour construire des atlas de l'activité électrique intracrânienne de différentes régions cérébrales saines. Ainsi, la base de données MNI Open IEEG Atlas inclut des enregistrements intracrâniens de 20 patients épileptiques présentant une activité physiologique issue de régions non lésionnelles (von Ellenrieder et al., 2020).

0.2.2 EEG de scalp

En dehors d'un contexte clinique, on peut également mesurer l'activité cérébrale de manière non invasive en plaçant des électrodes sur le scalp (voir Figure 0.4). L'EEG de scalp reflète l'activité électrique cérébrale, principalement générée par les neurones pyramidaux du cortex qui sont les plus proches du scalp. Ces neurones sont majoritaires dans le cortex et orientés perpendiculairement à sa surface. Cette organisation particulière permet de modéliser des regroupements de neurones par des dipôles électriques, produisant une différence de potentiel mesurable au niveau du cuir chevelu à l'aide de l'EEG (Baillet, Mosher, & Leahy, 2001). Le potentiel mesuré sur le scalp sera d'autant plus ample qu'il est produit par la synchronisation d'un grand nombre de neurones et plus généralement, de dipôles d'une région corticale.

La taille d'une électrode est d'environ 10 mm (Luo & Guan, 2018). Placée sur le cortex, elle mesure l'activité électrique résultant de la somme de l'activité neuronale distribuée dans le voisinage de l'électrode (Luo & Guan, 2018). Ce signal présente donc une faible résolution spatiale et peut être plus complexe à interpréter en raison du mélange de plusieurs sources corticales. L'amplitude de cette mesure est de l'ordre de quelques microvolts (µV).

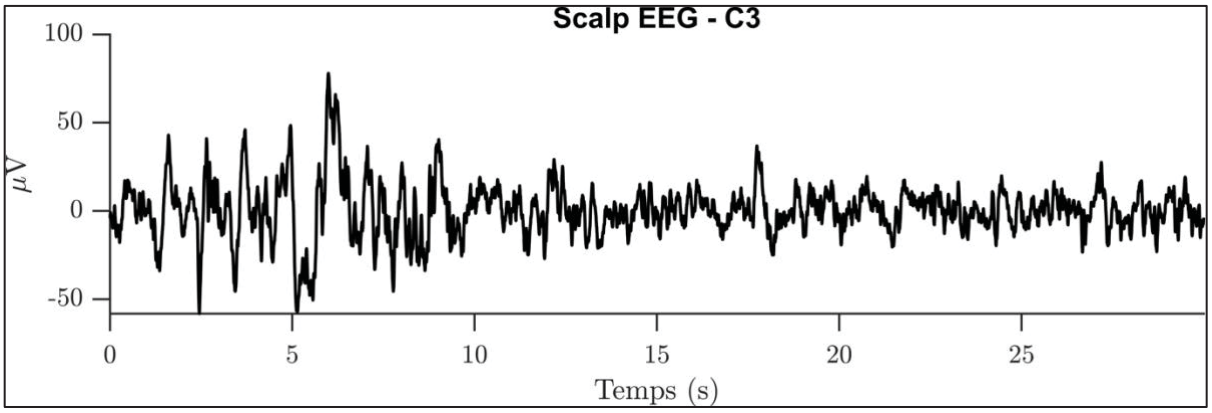

Figure 0.4 Exemple d'un signal EEG de scalp mesuré à l'électrode C3 durant le sommeil NREM3

Le montage d'électrodes EEG de scalp le plus commun est le système '10-20' composé de 19 électrodes à des positions standardisées sur le scalp. L'emplacement des électrodes assure une bonne couverture du scalp et une mesure standardisée**,** comparable et reproductible**.** L'EEG offre une excellente résolution temporelle (jusqu'à la milliseconde), ce qui en fait un outil privilégié pour mesurer l'activité cérébrale au cours du temps. Par contre, l'EEG standard n'est pas un outil d'imagerie, étant donné sa faible résolution spatiale. En revanche, des variantes du système '10-20', telles que les montages à haute densité composés de 128 électrodes, améliorent la résolution spatiale et permettent une localisation des générateurs.

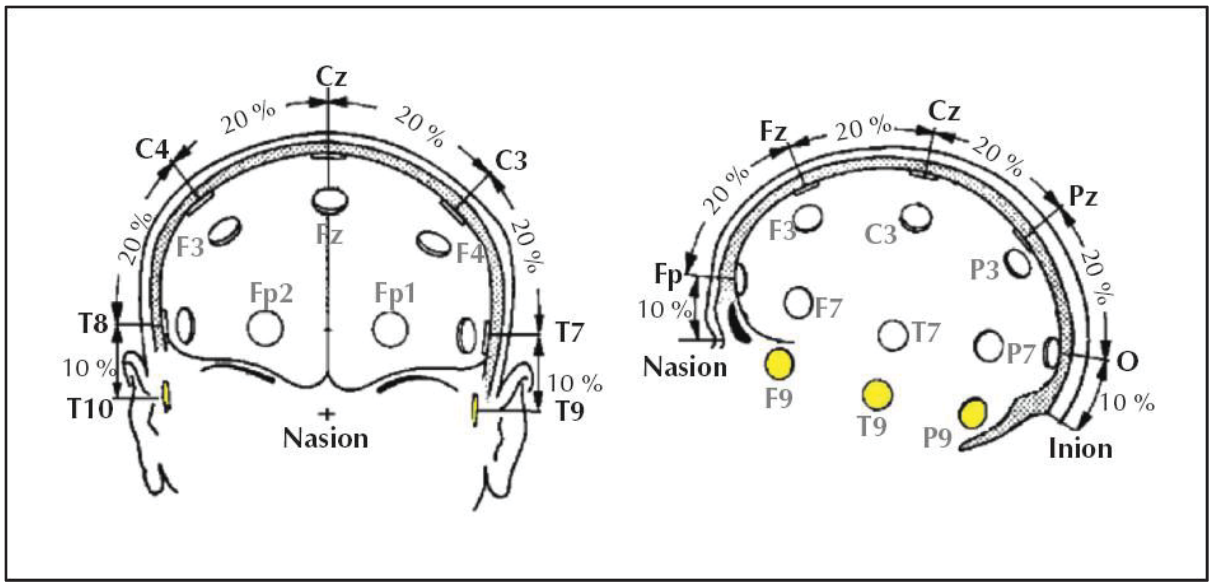

Figure 0.5 Montage EEG 10-20 sur le scalp
Tiré de Beniczky & Schomer (2020)

Ces signaux sont affectés par le bruit (i.e. Hydro-Québec), les mouvements musculaires ou le clignement des yeux, ce qui les rend plus susceptibles aux artefacts. Plusieurs algorithmes de détection et de correction sont nécessaires pour identifier et atténuer ces artefacts afin d'améliorer la qualité de ces signaux.

0.3 Les rythmes du sommeil capturés par les enregistrements EEG

Que ce soient les mesures intracrâniennes ou sur le scalp, les enregistrements électrophysiologiques de l'activité cérébrale pendant le sommeil permettent de capturer plusieurs processus caractéristiques à différentes échelles temporelles. À l'échelle de l'ordre de la seconde, les enregistrements EEG du scalp révèlent des oscillations propres à chaque stade de sommeil. Elles se manifestent de manière transitoire et sporadique, avec une fréquence caractéristique. Durant le NREM 1, on observe des oscillations thêta (4-7 Hz) et une diminution progressive des oscillations alpha (8-10 Hz), caractéristiques de l'état d'éveil (Léger et al., 2018). Le stade NREM 2 est caractérisé par la présence de fuseaux de sommeil (12 - 16 Hz) et complexe K qui sont des ondes biphasiques de grande amplitude souvent couplées avec les fuseaux de sommeil. Le stade NREM 3 se caractérise par une diminution

progressive des fuseaux de sommeil et une augmentation des ondes lentes (1–4 Hz). Le sommeil REM se caractérise par la présence d'ondes thêta. À bien des égards, le REM est similaire à l'état d'éveil, avec un signal à faible amplitude et à haute fréquence.

L'étude des oscillations cérébrales suscite un intérêt important, dans la mesure où leur caractérisation permet de décoder des processus neuronaux, tels que ceux impliqués dans la consolidation de la mémoire. Par exemple, l'application de stimulation transcrânienne, qui induit artificiellement des ondes lentes pendant le sommeil NREM 3, entraîne une amélioration de la mémoire déclarative, un type de mémoire impliquant la récollection d'informations (Marshall, Helgadóttir, Mölle, & Born, 2006). Après l'entraînement à une tâche d'apprentissage, la densité des fuseaux (nombre de fuseaux par minute) durant le sommeil est plus élevée que dans une condition « contrôle » sans apprentissage (Gais, Mölle, Helms, & Born, 2002). Parmi les oscillations caractéristiques du sommeil, les fuseaux de sommeil et les ondes lentes occupent une place particulièrement importante (voir Figure 0.6).

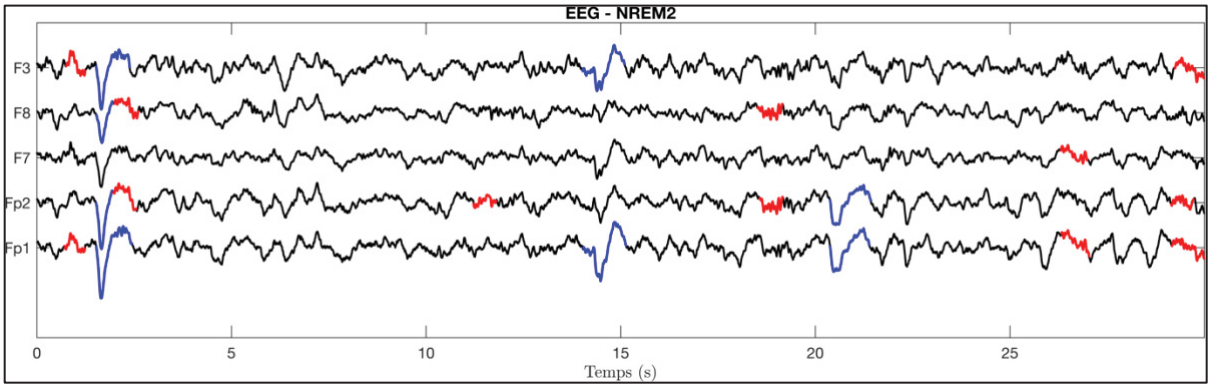

Figure 0.6 Exemple d'oscillations caractéristiques du sommeil en NREM2 enregistrées avec des électrodes frontales (Bleu : ondes lentes ; Rouge : fuseaux)

0.3.1 Les fuseaux de sommeil

Les fuseaux de sommeil sont des oscillations de courte durée (1 à 3 secondes) à une fréquence de 12 à 16 Hz, qui ont lieu principalement durant le sommeil NREM 2. En général, un adulte en santé génère en moyenne 1,88 fuseaux par minute (Purcell et al., 2017). Les fuseaux résultent de l'interaction entre le noyau réticulaire thalamique et les neurones thalamocorticaux

(Léger et al., 2018) . Pendant l'éveil, le thalamus reçoit des signaux excitateurs, qui diminuent ensuite pendant le sommeil NREM. Cette réduction entraîne une hyperpolarisation des neurones thalamiques réticulaires, conduisant à des décharges rythmiques à la fréquence comprise entre 12 et 16 Hz. Ces décharges créent des cycles « inhibition-excitation » dans les neurones thalamocorticaux, qui transmettent des signaux entre le thalamus et le cortex (Schönauer & Pöhlchen, 2018). Ces interactions produisent des fuseaux de sommeil, visibles sur les enregistrements EEG. Les fuseaux peuvent varier en fréquence, avec des fuseaux lents (<13 Hz) situés dans le cortex frontal et des fuseaux rapides (>13 Hz) présentant une distribution recouvrant les régions pariétales et centrales (De Gennaro & Ferrara, 2003). La densité des fuseaux diminue avec l'âge ainsi que dans certaines conditions cliniques telles que la schizophrénie (Ferrarelli et al., 2010).

0.3.2 Les ondes lentes

Selon le modèle de Borbély & Achermann (1999), le sommeil est contrôlé par deux processus en interaction, le processus circadien (horloge diurne - nocturne) et le processus homéostatique (Borbély & Achermann, 1999). Ce processus décrit la pression de sommeil qui s'accumule pendant l'éveil d'une personne. Cette pression se dissipe normalement de manière exponentielle une fois endormie. Les ondes lentes (1–4 Hz) sont directement corrélées à cette pression de sommeil. En effet, un individu privé de sommeil générera davantage d'ondes lentes au début du sommeil. Les ondes lentes sont caractérisées par une phase d'hyperpolarisation durant laquelle les neurones corticaux sont silencieux, suivie d'une phase de dépolarisation durant laquelle les neurones s'activent (Léger et al., 2018). Les ondes lentes émergent principalement dans les régions frontales et se propagent en direction antéropostérieure (Massimini, Huber, Ferrarelli, Hill, & Tononi, 2004). Ces ondes peuvent être classées selon la fréquence associée à la transition entre les phases d'hyperpolarisation et de dépolarisation (Bouchard et al., 2021). Les transitions rapides sont appelées « fast switcher » et les transitions lentes, « slow switcher ». Les « slow switchers » présentent une connectivité cérébrale plus élevée que les « fast switchers », ce qui reflète une synchronisation accrue entre les régions du cerveau (Bouchard et al., 2021). Les ondes lentes contribuent à plusieurs processus. Entre

autres, elles jouent un rôle important dans plusieurs processus liés à la mémoire. Également, elles diminuent en amplitude et en occurrence avec l'âge (Carrier et al., 2011). Ceci est potentiellement dû à une diminution de la force synaptique et à une perte neuronale liée au vieillissement normal (Léger et al., 2018).

0.4 L'activité apériodique

Les activités rythmiques et sporadiques présentées précédemment ont une fréquence et une durée caractéristiques, souvent associées à des fonctions cognitives ou physiologiques spécifiques. Cependant, ces rythmes coexistent avec un signal de fond qui ne présente ni périodicité ni fréquence dominante. Ce signal apériodique est omniprésent dans tous les enregistrements électrophysiologiques et a longtemps été négligé dans l'interprétation des signaux EEG (voir figure 0.7).

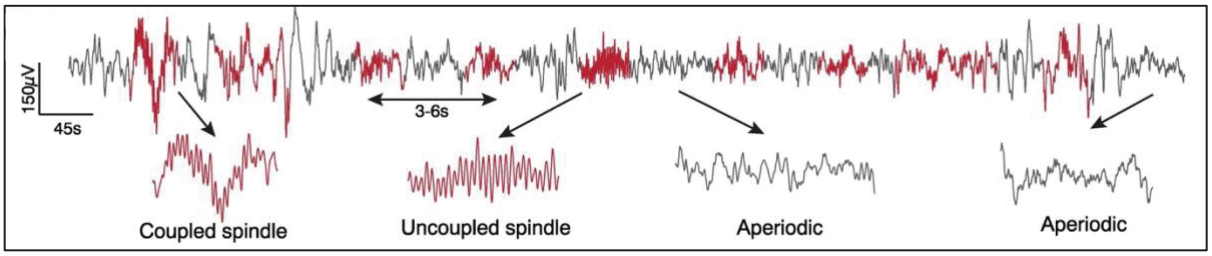

Figure 0.7 Signal illustrant la présence des rythmes caractéristiques du sommeil (rouge) et d'une activité apériodique (noire)
Tiré de Helfrich et al. (2021)

À ce jour, la caractérisation de l'activité apériodique se limite au domaine spectral (Donoghue et al., 2020 ; Wen & Liu, 2016). Elle est caractérisée à partir de l'analyse de Fourier, qui mesure la puissance du signal à chaque fréquence, comme illustré à la figure 0.8. L'activité apériodique, lorsque visualisée en log-log, montre une décroissance régulière de la puissance en fonction de la fréquence (f) qui est modélisable par une loi $\frac{1}{f^{\beta}}$. Le paramètre β caractérise cette décroissance et s'appelle « exposant d'échelle ».

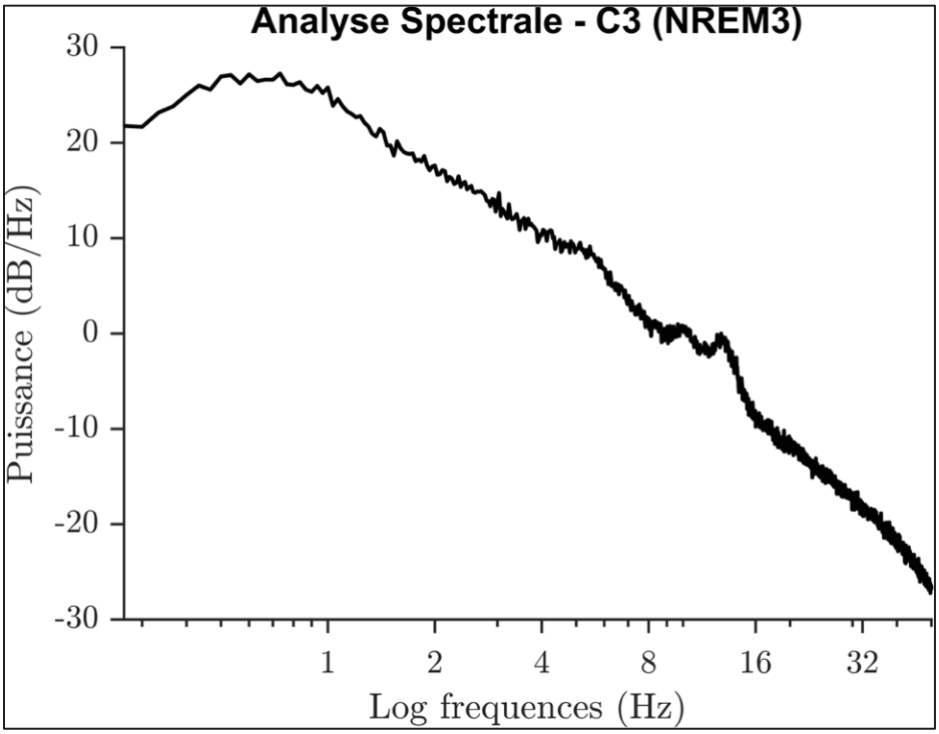

Figure 0.8 Analyse spectrale moyenne (log-log) des signaux NREM3 mesurés à l'électrode C3, illustrant l'activité apériodique, caractérisée par une décroissance de la puissance en fonction de la fréquence

On estime qu'environ 50 % d'une nuit de sommeil est constituée d'activité apériodique (Helfrich et al., 2021). Initialement interprété comme un simple bruit physiologique, ce signal suscite aujourd'hui un intérêt particulier. Sa valeur clinique et son origine sont aujourd'hui des sujets importants en EEG quantitatif. L'exposant d'échelle β a été mesuré localement sur le scalp dans différents états, tels que le vieillissement et les stades de sommeil (Bódizs et al., 2021 ; Helfrich et al., 2021 ; Voytek et al., 2015). Ainsi, l'exposant diminue avec l'âge et augmente au cours des stades de sommeil NREM. Cet exposant peut ainsi servir à caractériser différents états cérébraux d'un individu. Le signal apériodique, en recrutant toutes les fréquences, interfère avec les rythmes canoniques du sommeil. La caractérisation de ces composantes dans le domaine fréquentiel est insuffisante pour expliquer comment elles interfèrent entre elles, car elle exclut l'information de phase et la dynamique temporelle de leur interaction. Ainsi, la caractérisation rigoureuse des rythmes nécessite des méthodes de traitement du signal capables de séparer ces composantes.

0.5 Topographies

En général, l'activité apériodique et rythmique est mesurée de façon locale sur une électrode. Cependant, les électrodes couvrent l'ensemble du scalp et permet à l'EEG de mesurer une activité électrique globale. Celle-ci peut être représentée par une topographie dynamique du potentiel telle qu'illustrée dans la figure 0.9. Pourvu que la couverture des électrodes sur le scalp soit adéquate, une topographie peut être associée à l'activité électrique projetée sur le scalp et en caractériser l'activité physiologique à l'échelle macroscopique.

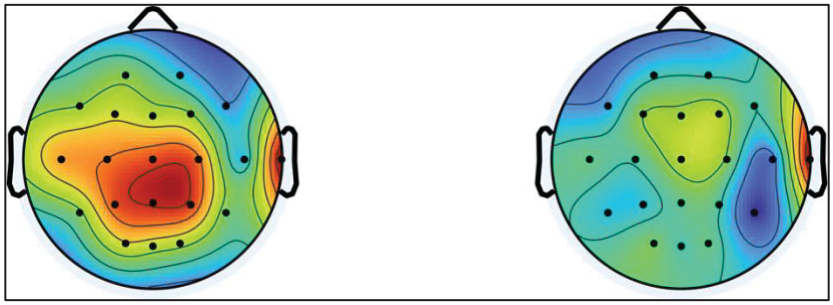

Figure 0.9 Exemple de topographies sur le scalp

La dynamique des topographies peut être obtenue en mesurant l'activité globale du scalp en fonction du temps. Une manière d'obtenir la dynamique de l'activité EEG consiste à calculer, pour chaque échantillon temporel, l'écart-type des amplitudes à travers les électrodes. Cette mesure estime, au fil du temps, la variabilité spatiale de l'activité sur le scalp. Ainsi, lorsque cette mesure est élevée, elle reflète une variation de l'activité bioélectrique au niveau du scalp, ce qui suggère une synchronisation de l'activité neuronale au sein de certaines régions. Une valeur faible indique que l'activité sur le scalp est homogène.

La variance de cette dynamique des topographies peut être synthétisée et expliquée à partir de 4 à 5 topographies, appelées micro-états (Lehmann, Ozaki, & Pal, 1987). La plupart des études sur les micro-états portent sur l'état de repos et la conjoncture actuelle est que les micro-états correspondent à différents réseaux fonctionnels (Britz, Van De Ville, & Michel, 2010). Les réseaux fonctionnels sont des régions du cerveau qui sont activées simultanément lors de tâches cognitives. Par exemple, il y a le réseau du mode par défaut, qui est actif lorsqu'un individu

est en repos et qui recrute le cortex préfrontal médian, le cortex cingulaire postérieur, le précuneus et le lobule pariétal inférieur (Raichle, 2015). Ainsi, caractériser la dynamique des micro-états permet de mieux comprendre le fonctionnement des réseaux fonctionnels. Une étude sur le repos a montré que la dynamique des micro-états est apériodique et qu'elle facilite la transition entre différents réseaux fonctionnels (Van De Ville, Britz, & Michel, 2010). Des études sur les micro-états ont également été menées dans le contexte du sommeil et montrent que les micro-états demeurent similaires entre l'état d'éveil et le sommeil (Brodbeck et al., 2012). Cette signature apériodique de la dynamique des micro-états au repos, qui permet de mieux comprendre le fonctionnement des réseaux à grande échelle, n'a toutefois pas été étudiée en sommeil.

0.6 Les défis du traitement du signal électrophysiologique

Tel qu'indiqué dans la section 0.4, pour comprendre l'intrication entre l'activité apériodique et l'activité rythmique au sein des signaux EEG, les méthodes actuelles ne peuvent pas se limiter aux approches fréquentielles. Afin de séparer ces composantes, on doit recourir à des méthodes telles que l'analyse temps–fréquence avec une famille d'ondelettes spécifiques sensibles à l'activité apériodique. Ces approches permettent d'accéder à l'information spectrale tout en préservant la résolution temporelle du signal EEG. Ce cadre méthodologique est ainsi essentiel au développement d'algorithmes de traitement du signal visant à isoler et à caractériser la composante rythmique des enregistrements EEG.

Un autre aspect important, abordé dans la section 0.5, porte sur l'analyse des micro-états. Ceux-ci sont associés aux topographies instantanées de l'EEG. Cette approche résulte en des séquences de micro-états dont la durée varie irrégulièrement dans le temps. Tel que mentionné, il a été montré que les transitions des micro-états au repos reflètent une activité de nature apériodique. Toutefois, l'organisation temporelle irrégulière des micro-états limite l'applicabilité des méthodes fréquentielles classiques fondées sur un échantillonnage régulier. Dans ce contexte, une méthode spectrales adaptées aux séries temporelles irrégulièrement échantillonnées, telle que l'analyse de Lomb–Scargle est essentielle. Ceci permet d'obtenir

une estimation spectrale robuste et constitue ainsi une approche appropriée et originale pour l'étude des propriétés des micro-états. Ainsi, à partir de l'analyse de Lomb-Scargle, il sera possible de démontrer et caractériser l'activité apériodique des séquences de micro-états.

0.7 Objectif de la thèse

Ainsi, les signaux EEG présentent une activité rythmique et apériodique, pouvant être caractérisée à la fois localement et globalement. La caractérisation de ces composantes demeure un défi méthodologique majeur, compte tenu de la complexité des signaux EEG. L'objectif de cette thèse est de développer des outils numériques visant à optimiser le décodage des composantes rythmiques et apériodiques des signaux EEG en sommeil. L'objectif à plus long terme est leur application à des populations cliniques, afin d'identifier des biomarqueurs robustes issus des composantes apériodiques et rythmiques pour différentes pathologies.

Un premier outil numérique a d'abord été développé et évalué dans le contexte d'enregistrements intracrâniens acquis chez des sujets épileptiques. Dans un deuxième temps, le même algorithme a été modifié pour l'appliquer à l'EEG du scalp chez des sujets sains. Finalement, un dernier outil est proposé pour mesurer l'activité apériodique de manière globale, à l'aide des micro-états, également chez des sujets sains. Les outils numériques présentés dans cette thèse pourront caractériser les composantes rythmiques et apériodiques à différentes échelles spatiales. Les chapitres suivants abordent les différents aspects et développements méthodologiques proposés.

Chapitre 1 : Contexte théorique et revue de littérature

Dans ce chapitre, le contexte théorique présentera les outils numériques qui seront utilisés dans le cadre de la thèse. Ensuite, la revue de littérature consistera à décrire l'état de l'art des méthodologies actuelles permettant de séparer l'activité rythmique et apériodique, ainsi qu'à présenter les études caractérisant l'activité apériodique durant le sommeil. L'objectif est de

contextualiser les limites de la littérature existante et de préciser en quoi les chapitres suivants contribueront à combler ces lacunes.

Chapitre 2 : Signal rythmique au niveau intracrânien en sommeil NREM

L'objectif de ce chapitre est de présenter une approche de traitement du signal pour estimer la contribution rythmique des enregistrements intracrâniens du sommeil, au-delà des méthodes actuelles fondées sur l'analyse spectrale. En disposant d'un signal axé sur les rythmes, dans lequel l'activité apériodique a été éliminée, il est possible d'effectuer des analyses approfondies des rythmes du sommeil. L'applicabilité de l'algorithme est évaluée à l'aide de l'analyse spectrale rhythmique, de la détection d'ondes lentes et du couplage phase-amplitude sigma-delta.

Ce travail a été accepté au journal scientifique à comité de lecture *eNeuro* :

Dubé, J., Foti, M., Jaffard, S., Latreille, V., Frauscher, B., Carrier, J., & Lina, J. M. (2026). Rhythms and Background (RnB): The spectroscopy of sleep recordings. *eNeuro*.

Ce travail a également été présenté à Séville lors du congrès de la Société européenne de recherche sur le sommeil en octobre 2024 :

Foti, M. C., Smith, D., Higginson, C., Vu, T. D., Morin, C., Lina, J. M., & Robillard, R. (2024). Arrhythmic and rhythmic components of the sleep electroencephalogram: Preliminary results from a wavelet approach to compare healthy sleep and insomnia. *Journal of Sleep Research*, *33*(S1), P622.

Une demande de brevet pour l'algorithme a été déposée en août 2024 : « *System and numerical method for electrophysiological oscillatory rhythms extraction and characterization ».*

Ce travail a également reçu le « *Best Paper Award »* lors de la 12e Conférence internationale sur le traitement d'image, les ondelettes et leurs applications à des problèmes réels (IWW 2025).

Chapitre 3 : Signal rythmique au niveau du scalp en sommeil NREM

Les enregistrements EEG du scalp mesurent l'activité corticale issue de régions voisines. Ceci présente un signal combinant des composantes rythmiques et apériodiques plus complexes. Tout de même, l'EEG du scalp est non invasif et couramment utilisé en contexte clinique. Il est donc important que l'algorithme d'extraction des signaux rythmiques présenté au chapitre 2 fonctionne sur les enregistrements du scalp. L'objectif de ce chapitre est d'étendre l'application de l'algorithme afin d'obtenir des signaux rythmiques physiologiquement fiables à partir des signaux EEG du scalp. Ceci est évalué en analysant l'analyse spectrale rythmique, l'activité apériodique, ainsi que la détection des fuseaux de sommeil du signal rythmique.

Ce travail a été soumis au journal scientifique à comité de lecture *IEEE Transactions on Biomedical Engineering*:

Foti, M.C., Smith, D., Robillard, R., & Lina, J.-M. (2026). *Wavelet-based assessment of the rhythmic EEG activity during NREM sleep* [Manuscript submitted to IEEE Transactions on Biomedical Engineering].

Chapitre 4 : L'analyse spectrale et l'activité apériodique des topographies des micro-états

Les micro-états offrent un codage instantané des signaux EEG en intégrant les informations provenant de l'ensemble des électrodes selon des topographies canoniques. Le codage obtenu pour chaque micro-état est toutefois irrégulier. L'objectif de ce chapitre est de présenter une méthode permettant d'analyser spectralement ce codage irrégulier des topographies associées aux micro-états et d'en quantifier l'activité apériodique. On évalue également un aspect

neurophysiologique du sommeil en examinant l'activité apériodique associée aux micro-états EEG durant le sommeil NREM et en étudiant les effets d'âge.

Ce travail a été soumis au journal scientifique à comité de lecture *Brain Topography*:

Foti, M.C., Smith, D., Robillard, R., & Lina, J.-M. (2026) *Spectral analysis and scale-free activity of topographical microstates during NREM sleep* [Manuscript in review at *Brain Topography*].

CHAPITRE 1

CONTEXTE THÉORIQUE ET REVUE DE LITTÉRATURE

Ce chapitre présente l'état de l'art à propos de l'activité cérébrale apériodique et des topographies de l'EEG (micro-états), afin de situer ce travail dans la littérature existante. Il introduit également les outils numériques nécessaires aux développements méthodologiques de cette thèse qui serviront en particulier à extraire un signal rythmique des enregistrements EEG et à caractériser l'activité apériodique au niveau des topographies.

En premier lieu, on introduit l'analyse de Fourier dans le contexte de l'électrophysiologie ainsi que la caractérisation des composantes rythmiques et apériodiques des spectres. On présente ensuite l'invariance d'échelle temporelle, qui décrit la manière dont l'activité apériodique se manifeste au niveau du signal. On présente l'interprétation physiologique actuelle de l'activité apériodique, ainsi que les méthodes décrites dans la littérature pour caractériser la composante au niveau du spectre. On introduit ensuite les outils numériques nécessaires (les ondelettes) permettant d'aller au-delà des méthodes habituelles. Finalement, sachant qu'il est nécessaire de séparer l'activité rythmique et apériodique au niveau du signal, on présente une méthode de traitement de signal de détection des rythmes spécifiques à partir du signal rythmique. Finalement, on décrit les études portant sur l'activité apériodique et son intérêt clinique en sommeil.

En deuxième lieu, on présente l'analyse multifractale qui sera utilisée dans le cadre des micro-états. On présente les « micro-états » et les outils d'analyse spectrale (Lomb-Scargle) qui seront utilisés pour caractériser la composante apériodique de ces topographies fondamentales de l'EEG de scalp. On termine en montrant comment l'analyse spectrale, dans le contexte des micro-états, est liée aux méthodes d'analyse de Fourier classiques en neurosciences.

1.1 Analyse de Fourier des signaux physiologiques

Pour un signal échantillonné à une fréquence d'échantillonnage f_s et composé de N échantillons, la transformée de Fourier décrit le contenu spectral à des fréquences multiples de $\Delta f = \frac{f_s}{N}$, i.e., $f_k = k\Delta f$ où $k = 0,1,\dots N-1$. Pour un signal réel, les fréquences utiles vont jusqu'à la fréquence de Nyquist, $f_k < f_s/2$. Les coefficients de Fourier sont obtenus par l'équation,

$$\hat{s}(f) = \sum_n s[n] e^{-i2\pi f n} \tag{1.1}$$

où $s[n]$correspond au signal à l'instant n/f_s et $\hat{s}(f)$ correspond aux coefficients de Fourier complexes. Les coefficients de Fourier caractérisent chaque fréquence d'un signal par une amplitude et une phase. L'analyse spectrale porte uniquement sur l'amplitude et la puissance spectrale de la fréquence *f* est définie par,

$$P(f) = \frac{1}{N}|\hat{s}(f)|^2 \tag{1.2}$$

En théorie, la transformée de Fourier n'est légitime que pour un signal stationnaire. Toutefois, lorsqu'on considère un signal sur une fenêtre de N échantillons, les propriétés statistiques des signaux EEG varient avec le temps. En pratique, plus la durée d'analyse est courte, plus le signal rencontre la propriété de stationnarité. Si on veut identifier des modes spectraux $P(f)$ avec précision, il faut une durée d'analyse longue. Le calcul de la puissance spectrale nécessite donc un compromis entre la résolution spectrale (Δf) et la durée de la fenêtre d'analyse des signaux EEG. D'habitude, les analyses EEG reposent sur des fenêtres d'une durée de 4 à 20 secondes. Le choix de cette durée dépend de la résolution spectrale requise pour tirer des conclusions pertinentes sur la structure du spectre. À partir de l'analyse spectrale d'un signal, nous pouvons calculer l'énergie en sommant les puissances sur les bandes de fréquence canoniques de l'électrophysiologie (Figure 1.1 et Table 1.1). Ces bandes ont une valeur physiologique, car plusieurs mécanismes cérébraux s'y manifestent (Buzsáki & Draguhn, 2004). Par exemple, dans la bande alpha, la fréquence de 10 Hz est caractéristique de l'état de repos avec les yeux fermés (Garcia-Rill et al., 2016). La bande gamma est associée aux mécanismes d'attention (Jensen, Kaiser, & Lachaux, 2007). Un autre exemple, durant le

sommeil, où les fuseaux de sommeil se manifestent à une fréquence de 12 à 16 Hz et sont caractéristiques de la bande sigma (Fernandez & Luthi, 2019). Ainsi, il faut une résolution spectrale suffisante pour distinguer les mécanismes cérébraux.

En neuroscience, on distingue souvent deux types d'énergie: l'énergie absolue et l'énergie relative. L'énergie absolue d'une bande spectrale $b = [f_{min}, f_{max}]$ est définie par,

$$\mathrm{E}_b = \sum_{f_k \in [f_{min}, f_{max}]} |P(f_k)|^2 \tag{1.3}$$

L'énergie relative décrit l'énergie contenue dans chaque bande $[f_{min}, f_{max}]$ par rapport à l'énergie totale du signal selon,

$$\mathrm{E}_{rel} = \frac{\mathrm{E}_b}{\sum E_{b'}} \tag{1.4}$$

Tableau 1.1 Bande de fréquences « b » canonique en neurosciences

Slow Waves	Delta (δ)	Thêta (θ)	Alpha (α)	Sigma (σ)	Bêta (β)	Gamma
(0.5 - 1) Hz	(1 - 4) Hz	(4 - 8) Hz	(8 - 12) Hz	(12 - 16) Hz	(16- 32) Hz	(30- 100) Hz

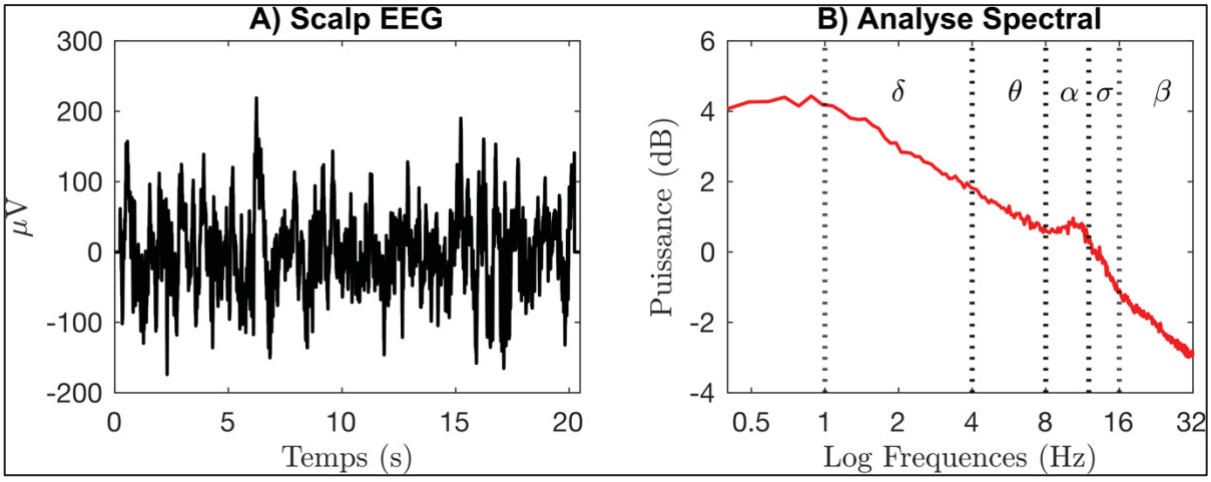

Figure 1.1 A) Signal EEG mesuré durant le sommeil ($f_s = 256$) B) Puissance spectrale correspondante du signal EEG de A)

Tel qu'illustré dans la figure 1.2, les spectres physiologiques présentent deux caractéristiques importantes dans le domaine log-log: des pics de fréquence, également appelés « résonances », et une décroissance spectrale. Les résonances du spectre rendent compte d'oscillations rythmiques transitoires et sporadiques dans le temps, caractéristiques d'une activité physiologique oscillatoire. Ces pics présentent une fréquence centrale ainsi qu'une largeur de bande. Plus ces oscillations sont de courte durée, plus cette bande de fréquence est large. Cette largeur de pic correspond donc à des bouffées d'oscillations d'activité rythmique transitoires. D'autre part, sur une échelle log-log, la puissance spectrale décroît de façon presque linéaire en fonction de la fréquence. Cette décroissance reflète une activité dépourvue de périodicité et de fréquence caractéristiques. Elle se manifeste sous la forme d'un fond spectral qui se comporte donc selon $P(f) \sim \frac{1}{f^{\beta}}$ où le paramètre spectral β est un exposant caractérisant ce fond apériodique pour lequel aucune échelle temporelle n'est spécifique. Comme on peut le voir sur la figure 1.2, on note que le spectre peut dévier d'une loi $\frac{1}{f^{\beta}}$ avec une atténuation des basses fréquences. Cette atténuation pourrait être partiellement liée au filtre passe-haut du système d'acquisition, susceptible de perturber la structure du spectre aux basses fréquences (Gerster et al., 2022). Néanmoins, le fonds spectral $1/f$ a une valeur physiologique (Lendner et al., 2020) sur la partie linéaire en représentation log-log. Ainsi, le spectre $P(f)$ peut toujours s'écrire sous la forme,

$$P(f) = \frac{C}{f^{\beta}} e^{R(f)} \tag{1.5}$$

où $\frac{C}{f^{\beta}}$ exprime la décroissance spectrale avec C qui est l'ordonnée à l'origine. Le facteur $e^{R(f)}$ correspond aux résonances du spectre. Ainsi, cette formulation définit à la fois les résonances et l'activité apériodique du spectre.

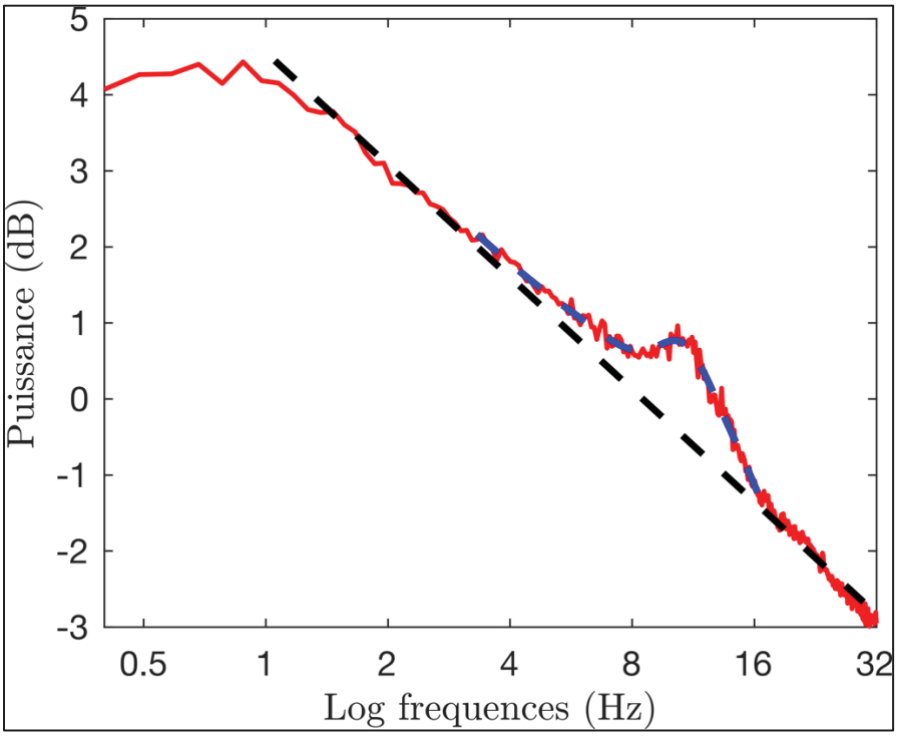

Figure 1.2 Description des composantes rythmique et apériodique de la puissance spectrale (Bleu : modélisation d'un pic de fréquence; noir: modélisation de la composante apériodique)

1.2 L'invariance d'échelle

Il existe une propriété permettant de décrire la décroissance spectrale : l'autosimilarité. Un signal autosimilaire est invariant d'échelle et satisfait par conséquent la relation,

$$s(at) \approx a^H s(t) \tag{1.6}$$

où a est un paramètre d'échelle permettant d'exprimer le signal à différentes résolutions. L'équation 1.6 établit une relation entre deux processus, $s(at)$ et $s(t)$. L'autosimilarité signifie qu'ils sont statistiquement équivalents à un facteur d'échelle de a^H où le paramètre H s'appelle exposant de Hurst et caractérise aussi la régularité du signal $s(t)$. En effet, la régularité décrit la propriété de lissage d'un signal, c'est-à-dire l'absence de variations abruptes dans le signal dans une opération de « grossissement » (échelle). L'autocorrélation quantifie le degré de similarité du processus avec lui-même mesuré à des instants différents. Plus l'autocorrélation

est maintenue sur une longue durée, plus il y aura de régularité et la valeur de H sera plus élevée.

Il existe quelques exemples de signaux invariants d'échelle. Le bruit gaussien fractionnaire (fGn) est un processus gaussien à accroissements stationnaires dont les échantillons sont corrélés. Un mouvement brownien fractionnaire (fBm) est le signal obtenu par la somme cumulée (intégrale) d'un fGn. Plus le signal fBm présente des corrélations temporelles à long terme, plus il est régulier, avec une atténuation des variations soudaine du signal.

On montre (Raymond & Bassingthwaighte, 1999) que l'exposant de Hurst est lié à la pente spectrale (β) de ces signaux. Pour le fGn, on obtient $\beta = 2H - 1$. Lorsque $H = 0.5$, $\beta = 0$ ce qui correspond à un spectre plat et donc du bruit blanc. Étant donné que le signal fBm correspond à l'intégrale d'un fGn, l'intégration agit comme une opération de lissage qui augmente la régularité, d'où $\beta = 2H + 1$ pour un fBm. Vu la non-stationnarité des signaux EEG, les assimiler à un brownien fractionnaire conduit à les modéliser par un fBm avec $\beta = 2H + 1$. Ains, l'invariance d'échelle est une symétrie d'un signal dont les propriétés statistiques ne changent pas sous l'action d'un changement d'échelle temporelle. Cette propriété est associée à un comportement apériodique qui se manifeste aussi au niveau spectral. Ainsi, l'exposant spectral β est directement est relié à l'invariance d'échelle présente au niveau du signal temporel.

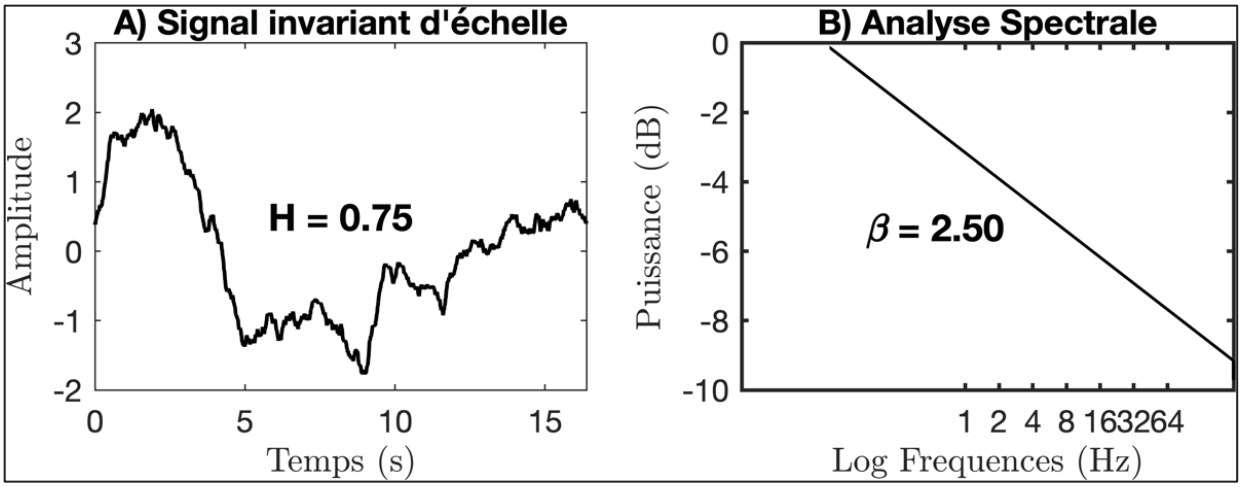

Figure 1.3 Exemple d'un signal simulé invariant d'échelle avec un exposant de Hurst de 0.75. B) Spectre correspondant présentant un exposant d'échelle β de 2.5, conforme à la relation attendue entre β et H

1.3 Activité apériodique physiologique

L'activité apériodique des signaux EEG, caractérisée par l'exposant d'échelle β (ou l'exposant H), fait l'objet de nombreux travaux visant à comprendre son origine physiologique. Actuellement, deux conjectures importantes existent pour interpréter la composante apériodique: le rapport excitation-inhibition (E/I) et les réseaux de connectivité fonctionnelle. L'activité excitatrice est induite par la libération de neurotransmetteurs excitateurs, tels que le glutamate, qui se lient à des récepteurs de la membrane postsynaptique en entraînant une dépolarisation. L'activité inhibitrice est plutôt causée par la libération de neurotransmetteur GABA (acide gamma-aminobutyrique), qui se lie à ses récepteurs post-synaptiques et réduit l'excitabilité neuronale en provoquant une hyperpolarisation. Cette activité inhibitrice maintient l'équilibre des réseaux neuronaux. Les signaux synaptiques excitateurs augmentent la probabilité de décharge neuronale, tandis que les signaux synaptiques inhibiteurs la réduisent. Le ratio E/I reflète l'homéostasie[1] neuronale et reste stable malgré les fluctuations continues des signaux synaptiques (Gao, Peterson, & Voytek, 2017). L'équilibre E/I influence le spectre large bande en raison de ces dynamiques neuronales. En effet, une pente du spectre

[1] La capacité d'un système à conserver un état d'équilibre

plus élevée indique une diminution de l'excitation et une augmentation de l'inhibition (Gao et al., 2017). Toutefois, une revue systématique a montré qu'il faut être prudent face à cette hypothèse en raison de l'hétérogénéité des résultats rapportés par les études (Donoghue, 2025). En effet, l'activité apériodique peut refléter un changement du rapport E/I, toutefois cet effet ne semble pas spécifique : des variations du ratio E/I peuvent ne pas entraîner de variation de pente spectrale (Donoghue, 2025).

Une étude menée par Brake et al. (2024) présente une autre interprétation fondée sur des simulations modélisant les interactions synaptiques interneurones. Des réseaux de neurones ont été simulés afin de montrer qu'en contrôlant le degré de corrélation entre les neurones, un signal EEG apériodique émerge lorsqu'ils sont davantage corrélés. Ainsi, ces simulations numériques suggèrent que l'activité apériodique dépend du degré de corrélation entre les neurones, et donc de la connectivité du réseau (Brake et al., 2024). En plus des effets liés à la connectivité du réseau, Brake et al. (2024) soutiennent l'hypothèse que l'inhibition contribue fortement aux basses fréquences du spectre de l'EEG (Gao et al., 2017). Cependant, ils montrent que l'exposant spectral ne constitue pas un marqueur fiable de l'équilibre E/I, car des paramètres membranaires indépendants de l'E/I, tels que la conductance de fuite, modifient la pente spectrale dans leurs simulations. La conductance de fuite correspond au passage continu des ions à travers les membranes neuronales.

Cette interprétation est soutenue par des enregistrements d'EEG réalisés sous anesthésie au propofol, dont les effets sur le spectre sont cohérents avec les simulations (Brake et al., 2024) Contrairement aux études reliant directement l'exposant spectral à l'équilibre E/I, ces résultats suggèrent que l'exposant spectral reflète une combinaison de mécanismes, résultant de l'interaction entre les processus synaptiques locaux et la connectivité des réseaux neuronaux.

1.4 Méthode spectrales pour caractériser l'exposant d'échelle

Dans le cadre de l'analyse des signaux EEG, les méthodes actuelles pour caractériser les activités rythmique et apériodique ont été développées dans le domaine spectral du signal à l'aide de différentes approches d'analyse du spectre de Fourier.

1.4.1 L'algorithme « Fitting Oscillations & One Over F » (FOOOF)

L'approche FOOOF exprime la puissance spectrale $P(f)$ selon le modèle additif suivant,

$$log\ (P(f)) = L(f) + \sum_{n=1}^{D} G_n(f) \tag{1.7}$$

où $L(f)$ est la partie spectre apériodique et chaque $G_n(f)$ est une gaussienne qui représente un mode oscillatoire à bande étroite (Donoghue et al., 2020). On suppose *D* modes oscillatoires dans le spectre alors que la puissance apériodique L(f) est modélisée par l'expression,

$$L(f) = log\left(\frac{C}{\kappa + f^{\beta}}\right) \tag{1.8}$$

où C est l'ordonnée à l'origine du spectre, β est l'exposant spectral et κ est un paramètre modélisant la possible déviation d'une loi $\frac{1}{f^{\beta}}$. Lorsque $\kappa \neq 0$ et $\kappa > f^{\beta}$, on a $\kappa + f^{\beta} \approx \kappa$ aux basses fréquences, ce qui donne un spectre plat dans cette partie du spectre. Pour les hautes fréquences, $\kappa + f^{\beta} \approx f^{\beta}$ et le spectre suit une loi $\frac{1}{f^{\beta}}$. Le paramètre κ vise à modéliser le plateau observé aux basses fréquences du spectre (voir Figure 1.2).

Les gaussiennes $G_n(f)$ décrivent les pics rythmiques et sont définies sous la forme,

$$G_n(f) = A_n e^{\frac{-(f-f_{c_n})^2}{2{\sigma_n}^2}} \tag{1.9}$$

A_n correspond à l'amplitude du pic oscillatoire et σ_n est la dispersion spectrale associée à la gaussienne n du spectre. Ainsi, l'algorithme de FOOOF modélise les composantes rythmiques et apériodiques du spectre, comme illustré à la figure 1.4. Les pics de fréquence f_{c_n} sont identifiés et modélisés de manière itérative à l'aide de gaussiennes, dont la somme constitue la composante spectrale rythmique du spectre. La composante apériodique est estimée par

régression du spectre $log(P(f))$, en négligeant l'influence des pics de puissance. La combinaison de ces deux composantes spectrales permet d'obtenir une modélisation finale du spectre. L'algorithme FOOOF nécessite de définir plusieurs paramètres, tels que le nombre de pics à identifier, l'intervalle de fréquences des pics à analyser, le seuil de détection des pics, ainsi que l'inclusion ou non d'une modélisation d'un « genou » dans le spectre. L'ajustement des paramètres requiert une bonne compréhension du spectre à analyser. Par exemple, selon le seuil choisi, les oscillations détectées par l'algorithme vont différer (Wainio-Theberge, Wolff, Gomez-Pilar, Zhang, & Northoff, 2022). De même, lorsque FOOOF est appliqué au spectre d'un enregistrement EEG, celui-ci est généralement trop bruité pour que FOOOF identifie correctement les oscillations (Wainio-Theberge et al., 2022). Actuellement, l'algorithme de FOOOF est la méthode la plus utlisée dans la littérature. Cependant, son application porte généralement sur des spectres moyennés, ce qui ignore l'information liée à la non-stationnarité de l'autosimilarité des signaux.

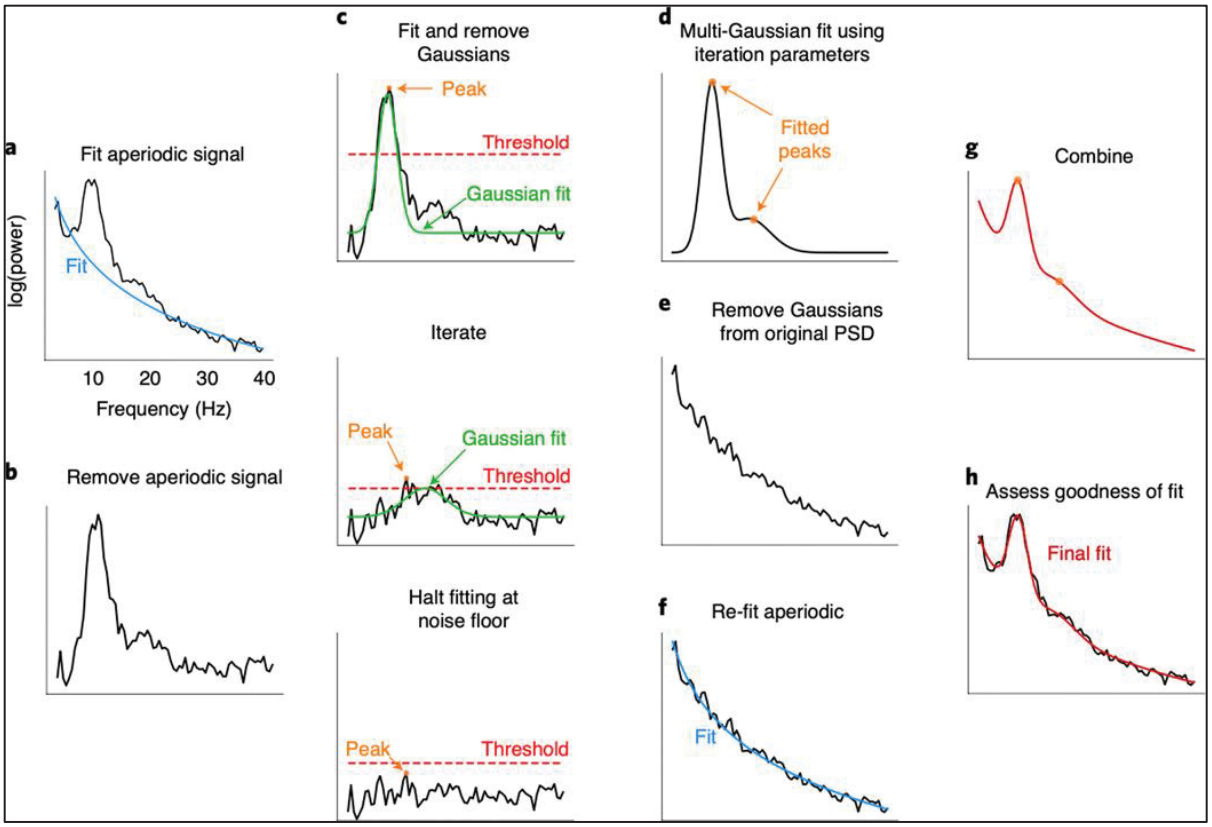

Figure 1.4 Algorithme de FOOOF. A) Modélisation du spectre apériodique B) Spectre résiduel obtenu après avoir soustrait la modélisation du spectre apériodique C) Chaque pic oscillatoire du spectre résiduel est identifié et modélisé par une gaussienne. D) Les gaussiennes identifiées sont combinées E) Les gaussiennes sont ensuite soustraites du spectre original afin d'obtenir un spectre apériodique. F) Le spectre apériodique est ensuite modélisé par une régression linéaire. G) Combinaison des gaussiennes et de la modélisation apériodique H) Évaluation du modèle

Tiré de Donoghue et al. (2020)

1.4.2 L'algorithme « Irregular Resampling Auto-Spectral Analysis » (IRASA)

Contrairement à FOOOF qui modélise la puissance spectrale, la méthode IRASA repose sur le signal et d'un modèle additif de sa transformée de Fourier,

$$\hat{s}(f) = \int s(t)e^{-i2\pi ft}dt = B(f)e^{i\alpha(f)} + O(f)e^{i\varphi(f)} \tag{1.10}$$

où $B(f)$ et $\alpha(f)$ correspondent à l'amplitude et à la phase du mode de Fourier du signal apériodique. $O(f)$ et $\varphi(f)$ correspondent à l'amplitude et à la phase du mode de Fourier du signal rythmique. À partir de l'équation 1.10, la puissance des modes de Fourier est donc,

$$\begin{aligned} P(f) \;=\; |\hat{s}(f)|^2 &= \big(B(f)e^{i\alpha} + O(f)e^{i\varphi}\big)\big(B(f)e^{-i\alpha} + O(f)e^{-i\varphi}\big) \\ &= B(f)^2 + O(f)^2 + 2B(f)O(f)\,cos\big(\alpha(f) - \varphi(f)\big) \\ &= \; B(f)^2\left(1 + \frac{O(f)^2}{B(f)^2} + 2\frac{O(f)}{B(f)}cos\big(\alpha(f) - \varphi(f)\big)\right) \\ &= \; B(f)^2 e^{R(f)} \end{aligned} \tag{1.11}$$

Ainsi, $\mathrm{B}(f)^2$ correspond au spectre apériodique défini par $\frac{c}{f^\beta}$ et le facteur $e^{R(f)}$ représente la partie rythmique.

L'algorithme IRASA propose de rééchantillonner le signal par un facteur d'échelle a ($s(t) \rightarrow s(at)$), qui préserve la propriété d'invariance d'échelle $1/f$ et atténue le rôle des composantes rythmiques du spectre. En effet, la transformée de Fourier de $s(at)$ correspond à,

$$\hat{s}_a(f) = \int s(at)e^{-i2\pi ft}dt \;=\; \frac{1}{a}\int s(t')e^{-\frac{i2\pi ft\prime}{a}}dt' =\; a^{-1}\hat{s}(f/a) \tag{1.12}$$

Ainsi, pour une échelle a et son inverse $\frac{1}{a}$, on obtient deux spectres,

$$P_a(f) = a^{\beta-2}\frac{C}{f^\beta}e^{R\left(\frac{f}{a}\right)} \tag{1.13}$$

$$P_{a^{-1}}(f) = a^{-\beta+2}\frac{C}{f^\beta}e^{R(af)} \tag{1.14}$$

dont la moyenne géométrique donne,

$$Q_a(f) = \sqrt{P_a(f)P_{a^{-1}}(f)} = \frac{C}{f^{\beta}} e^{\frac{R\left(\frac{f}{a}\right)+\mathrm{R}(af)}{2}} \tag{1.15}$$

Ce double rééchantillonnage est répété pour différentes échelles $\{a_i\}$ et son inverse $1/a_i$, où $i = 1, \dots, n$. La moyenne géométrique est calculée sur cet ensemble de paires de spectres. On a alors un ensemble de spectre défini par,

$$\begin{aligned} Q_{\{a_i\}}(f) &= \sqrt{\prod P_{a_i}(f)P_{a_i{}^{-1}}(f)} \\ &= \frac{C}{f^{\beta}} e^{\frac{1}{2}\sum R\left(\frac{f}{a_i}\right)+\mathrm{R}(a_i f)} \\ &\cong \frac{C}{f^{\beta}}(1+\epsilon) \end{aligned} \tag{1.16}$$

La stratégie de rééchantillonnage consiste à faire tendre ϵ vers 0 afin d'isoler la composante apériodique. Ainsi, l'estimation du spectre apériodique est $Q_{a_i}(f) \cong \frac{c}{f^{\beta}}$ obtenue en calculant la médiane à travers tous les spectres rééchantillonnés $Q_{a_i}(f)$,

$$B^*(f)^2 \cong mediane_a\left(Q_{a_i}(f)\right) \tag{1.17}$$

Finalement, les auteurs d'IRASA proposent d'utiliser la différence entre le spectre initial moyen $P(f)$ et le spectre apériodique estimé $B^*(f)$ afin d'obtenir le spectre rythmique (Wen & Liu, 2016), à partir de l'équation 1.11,

$$O^*(f)^2 \cong P(f) - B^*(f)^2 - 2B(f)O(f)\,cos\big(\alpha(f) - \varphi(f)\big) \tag{1.18}$$

Le terme $2B(f)O(f)\,cos\big(\alpha(f) - \varphi(f)\big)$, incluant l'information de phase, est négligeable à condition de moyenner $\mathrm{P}(f)$ sur plusieurs fenêtres, en raison des interférences de phase qui varient d'une fenêtre à l'autre.

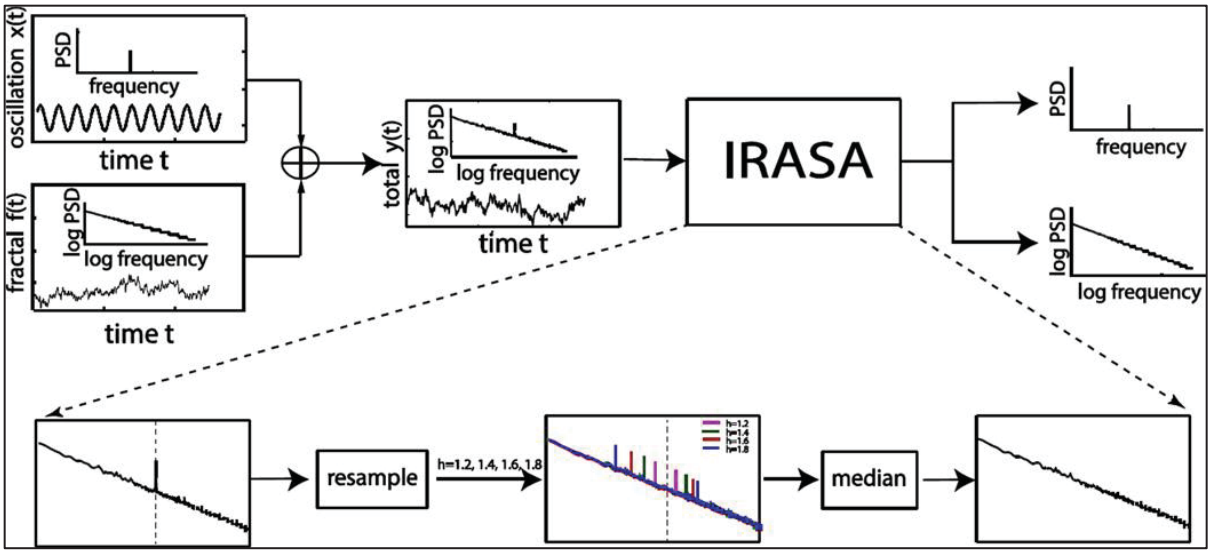

Figure 1.5 Un signal EEG est considéré comme la somme d'une composante rythmique et apériodique. L'algorithme IRASA applique plusieurs rééchantillonnages du signal selon des facteurs a et 1/a. Pour chaque paire (a, 1/a), on calcule les spectres de puissance moyens. Ensuite, pour chaque fréquence, on extrait la médiane des spectres moyens pour isoler le spectre apériodique. La composante rythmique est ensuite obtenue par soustraction entre le spectre original et le spectre apériodique
Tiré de Wen & Liu (2016)

IRASA et FOOOF décrivent les composantes apériodiques et rythmiques dans le domaine spectral, en ignorant l'information de phase des modes de Fourier. Une limite de ces approches est que le spectre de Fourier n'est pas propre à un signal particulier. On ne dispose pas des signaux associés à ces composantes, ce qui limite notre compréhension de leurs interférences et du rôle des phases. Ainsi, comme l'indiquent les auteurs d'IRASA, le domaine spectral n'est pas approprié et la dynamique spectrale résolue en temps doit être introduite. Le seul formalisme où l'on trouve à la fois les notions spectrales et temporelles est celui des analyses en temps-fréquence par ondelettes. Ainsi, pour mieux appréhender l'interaction entre ces composantes, il faut recourir à des méthodes de traitement du signal dans le domaine du temps-fréquence afin d'obtenir la dynamique locale des signaux. Ceci nécessite de passer du domaine de Fourier à celui des ondelettes.

1.5 La transformée par ondelettes

1.5.1 Un rappel sur la transformée par ondelette continue

Un signal $s(t)$ peut être représenté par un développement en petites ondes, appelées ondelettes $\psi(t)$, qui décrit son contenu fréquentiel en fonction du temps. Cette représentation est définie par des coefficients par ondelettes, qui quantifient la contribution de chaque ondelette au signal (Figure 1.6).

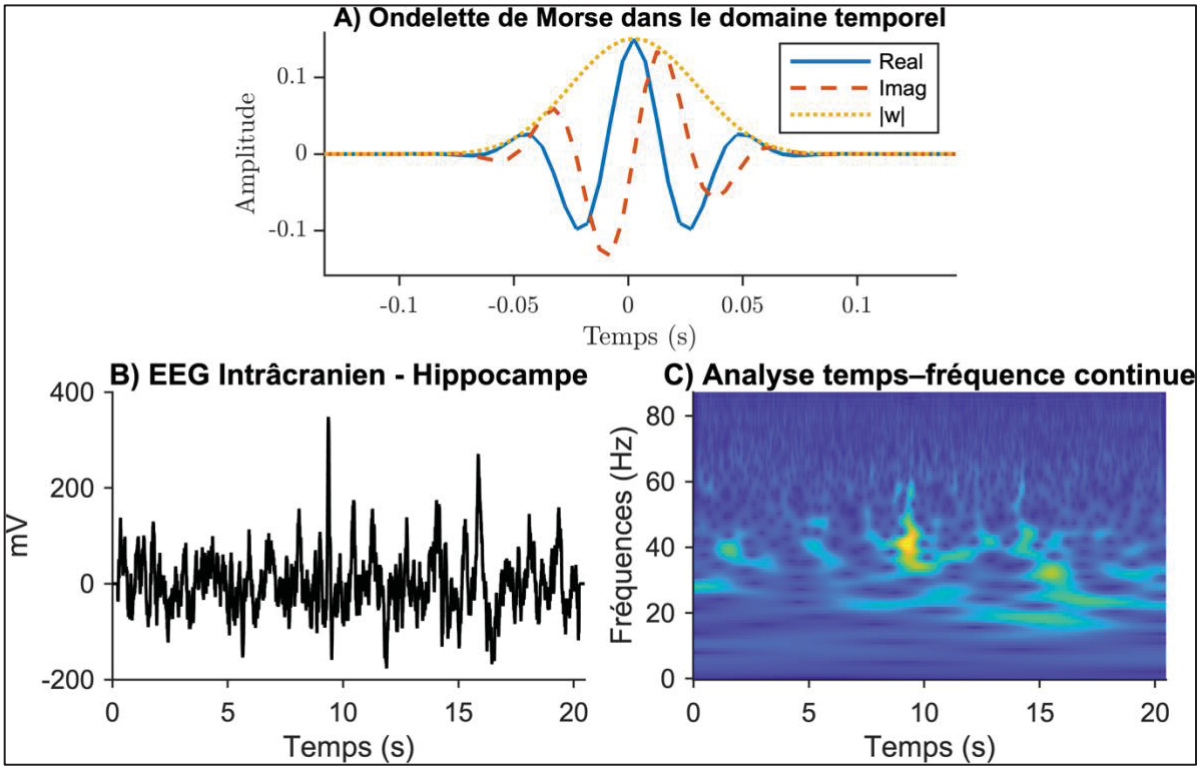

Figure 1.6 A) Une ondelette de Morse[2] utilisé pour décompose le signal en (B) B) Exemple d'un signal EEG B) Décomposition du signal EEG en plan temps-fréquence continu

On définit un dictionnaire d'ondelettes par les translations et les dilatations d'une ondelette mère $\psi(t) = \frac{1}{\sqrt{a}}\,\psi\left(\frac{t-b}{a}\right)$, afin de pouvoir caractériser les oscillations locales à différentes

[2] La description de l'ondelette de Morse utilisée dans le cadre de la thèse figure en annexe.

échelles d'un signal. Le signal est représenté par des coefficients qui mesurent la corrélation entre le signal et chaque ondelette,

$$w_{a,b} = \int_t s(t)\overline{\psi_{a,b}(t)}dt \tag{1.19}$$

La variable a dilate l'ondelette mère et le paramètre b translate l'ondelette. En dilatant l'ondelette mère ($a > 1$), on caractérise le signal à une échelle plus large sensible aux basses fréquences du signal analysé. Le facteur $\frac{1}{\sqrt{a}}$ garantit que l'ondelette conserve une énergie constante, qu'elle soit dilatée ou non.

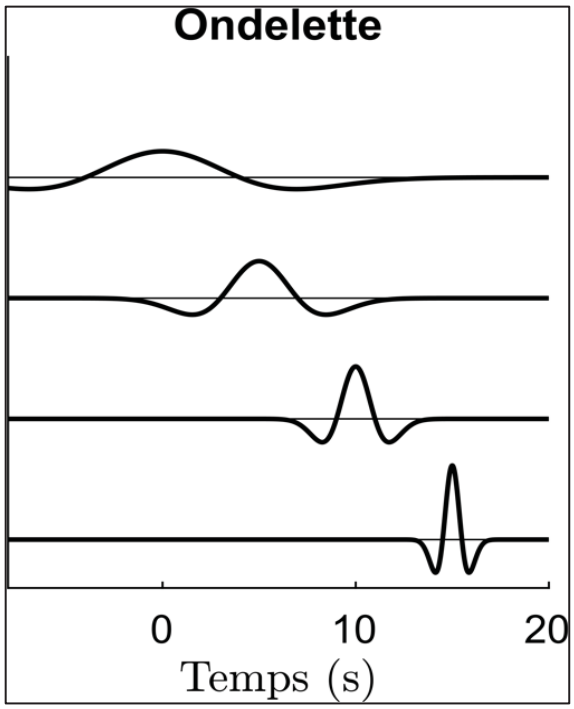

Figure 1.7 Dilatation ($a > 1$) et compression ($a < 1$) d'une ondelette translatée dans le temps

Formellement, le signal $s(t)$ peut être reconstruit à partir des coefficients selon l'équation ci-dessous,

$$s(t) = \frac{1}{C_\psi} \int_{a=0}^{\infty} \int_b w_{a,b}\, \psi_{a,b}(t) db \frac{da}{a^2} \tag{1.20}$$

où $C_\psi = \int_0^\infty \frac{|\hat{\psi}(f)|^2}{f} df < \infty$. On contrôle la divergence à $\omega = 0$ en imposante la condition $\hat{\psi}(0) = 0$.

L'ondelette doit donc osciller et être de moyenne nulle,

$$\hat{\psi}(0) = \int \psi(t) dt = 0 \tag{1.21}$$

Également, l'ondelette permettant de faire l'analyse d'un signal doit avoir une énergie fini (dans L^2),

$$\int |\psi(t)|^2 dt < \infty \tag{1.22}$$

Cela garantit l'existence d'une transformée de Fourier bien définie, ce qui permet la décomposition en temps-fréquences des signaux.

Lorsqu'on conçoit des ondelettes, une propriété importante est celle des moments nuls,

$$\int t^r \psi(t) dt = 0 \text{ pour } r = 0,1 \dots R \tag{1.23}$$

qui signifie que les coefficients par ondelettes sont nuls pour les signaux polynomiaux de degré $\leq R$. On donne ainsi la capacité d'être sensible à la régularité du signal d'un polynôme de degré R.

La condition Strang-Fix exprime la condition des moments nuls dans le domaine de Fourier,

$$\hat{\psi}(f) = f^{R+1} \hat{g}(f) \text{ avec } \hat{g}(0) \neq 0 \tag{1.24}$$

Ici, $\hat{g}(f)$ est une fonction d'échelle dont le support est localisé. La multiplication par f^{R+1} dans le domaine fréquentiel correspond à une dérivée d'ordre $R + 1$ dans le domaine temporel. Par conséquent, cette dérivation élimine tous les polynômes de degré R. Une ondelette $\psi(t)$ peut donc se construire à partir de la dérive de degré R d'une fonction $g(t)$ non oscillante mais localisée (intégrale différente de zéro et à un support compact).

1.5.2 La transformée par ondelette discrète

Les principes de la transformée par ondelettes continue se généralisent au domaine discret. Dans ce cas, le paramètre de dilatation est $a = 2^j$ et celui de translation est $b = k2^j$ où j correspond à un indice d'échelle et k à un indice de translation (j , $k \in \mathbb{Z}$). Le signal est décomposé en coefficients d'ondelettes tels qu'illustrés à la figure 1.8. Ils sont définis selon l'équation 1.19,

$$w_{j,k} = \int_{-\infty}^{\infty} s(t)\overline{\psi_{j,k}(t)}dt \tag{1.25}$$

où $\psi_{j,k} = \frac{1}{\sqrt{2^j}}\,\psi\left(\frac{t-k\,2^j}{2^j}\right)$

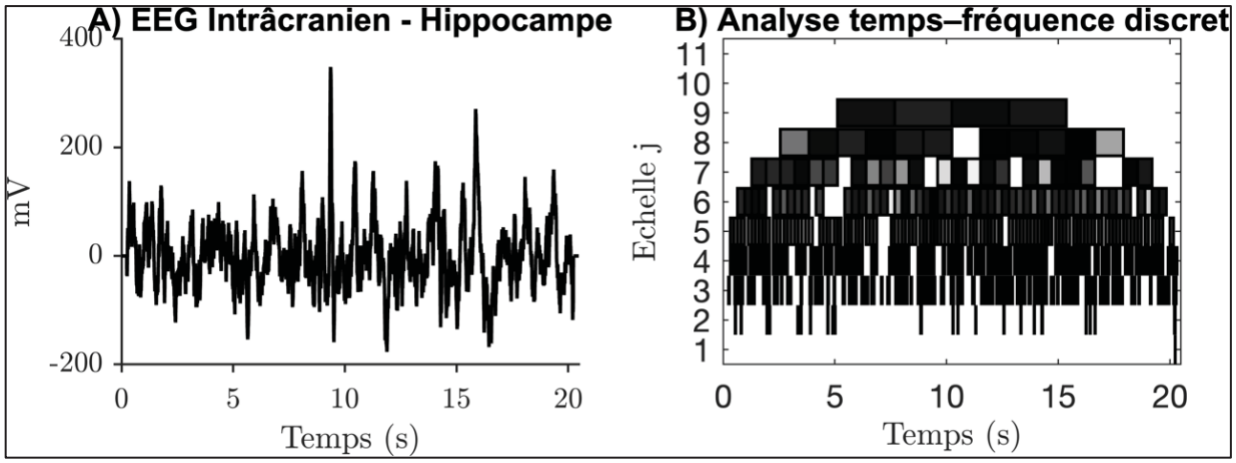

Figure 1.8 Exemple d'un signal EEG B) Décomposition du signal EEG en plan temps-fréquence discret. Chaque coefficient (boîte noire) à une échelle *j* et un temps *k* caractérise localement l'information du signal A)

Le signal peut être reconstruit à partir des coefficients d'ondelettes,

$$s(t) = \sum_j \sum_k w_{j,k}\ \psi_{j,k}\left(\frac{t-k2^j}{2^j}\right) \tag{1.26}$$

Concrètement, étant donné l'échantillonnage d'un signal de durée finie (N échantillons), on dispose d'un nombre fini d'échelles J déterminé par $J = \lfloor log_2 N \rfloor - 1$.

Ainsi, la reconstruction du signal est définie par,

$$s(t) = s_r(t) + \sum_{j \leq J} \sum_{k} w_{j,k}\, \psi\left(\frac{t - k2^j}{2^j}\right) \tag{1.27}$$

$s_r(t)$ correspond au signal reconstruit à partir de la somme des coefficients associés aux basses fréquences et $w_{j,k}$ représente les coefficients associés aux hautes fréquences du signal.

En pratique, l'analyse par ondelettes discrètes repose sur une opération de filtrage qui décompose le signal à différentes résolutions. Les filtres associés à l'ondelette discrète sont des filtres passe-bande qui sont le résultat d'une combinaison d'un filtre passe-haut ($\bar{g}[n]$) et d'un filtre passe-bas ($\bar{h}[n]$) (Mallat, 1989). Ces filtres sont associés à des fonctions de transfert $H(z)$ et $G(z)$ par les relations,

$$H(z) = \sum_{n} \bar{h}[n] z^n \tag{1.28}$$

$$G(z) = \sum_{n} \bar{g}[n] z^n \tag{1.29}$$

La longueur du filtre est proportionnelle au nombre de moments nuls R. Le processus de décomposition peut être effectué à l'aide d'une multitude de filtres, notamment ceux de Daubechies (Daubechies, 1988). On montre que les filtres Daubechies consistent à résoudre la relation,

$$P(z) - P(-z) = z \tag{1.30}$$

où $z = e^{i\omega}$ et $P(z) = \frac{z}{2}\bar{H}(z)\bar{H}(z^{-1})$. Cette relation implique que $\bar{H}(-1) = 0$. La première solution de Daubechies correspond à la solution de Haar,

$$H(z) = \sqrt{2}\left(\frac{1+z}{2}\right) \tag{1.31}$$

Une autre des solutions de Daubechies est,

$$H(z) = \sqrt{2}\left(\frac{1+z}{2}\right)^2 \frac{z^{-1} - z_1}{1 - z_1} \tag{1.32}$$

Dans cette équation, l'exposant 2 correspond au nombre de moments nuls (ici $R = 2$) et $z_1 = 2 - \sqrt{3}$. Pour les autres solutions de Daubechies, l'exposant augmente par valeurs entières.

Le filtre passe-haut est déterminé à partir du filtre $H(z)$ selon,

$$G(z) = -zH(-z)^* \tag{1.33}$$

L'équation 1.33 assure aussi l'orthogonalité des ondelettes qui permet de décorréler les coefficients par ondelettes.

Tel qu'illustré par la figure 1.9, le signal d'entrée $(a_o[n])$ est filtré avec des filtres passe-haut $(\bar{g})$ et passe-bas $(\bar{h})$ et ensuite décimé par 2. On obtient alors deux niveaux de coefficients : les coefficients d'approximation $(a_1[n])$ et les coefficients de détail $(d_1[n])$. Ce processus est ensuite répété sur les coefficients d'approximation du niveau d'échelle précédent, pour décomposer le signal à différentes échelles. Chaque échelle de décomposition correspond approximativement à une plage de fréquences du signal qui peut être déterminée à partir de sa fréquence d'échantillonnage,

$$\begin{aligned} f_{low\ bound} &= \frac{f_s}{2^{j+1}} \\ f_{up\ bound} &= \frac{f_s}{2^j} \end{aligned} \tag{1.34}$$

où j est l'indice d'une échelle. Finalement, le signal $\tilde{a}_0[n]$ peut être reconstruit par une synthèse d'ondelettes, à l'aide de filtre passe-haut $(\tilde{h})$ et passe-bas $(\tilde{g})$ complémentaire et d'un sur-échantillonnage par 2. Les filtres de synthèse ($\tilde{h}$ et $\tilde{g}$) sont équivalents aux filtres d'analyse inversés dans le temps,

$$\begin{aligned} \tilde{h}[n] &= \bar{h}[-n] \\ \tilde{g}[n] &= \bar{g}[-n] \end{aligned} \tag{1.35}$$

Le signal $\tilde{a}_0[n]$ reconstruit par synthèse est équivalent au signal d'entrée a_o. Contrairement aux ondelettes continues, les ondelettes discrètes produisent un ensemble de coefficients permettant leur traitement numérique.

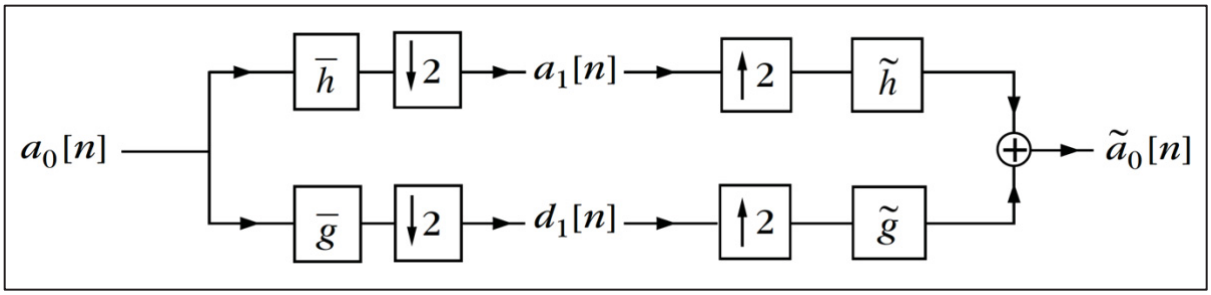

Figure 1.9 Analyse et synthèse des ondelettes
Tiré de Mallat (2009)

Les coefficients peuvent être construits à partir de filtres, au-delà de ceux de Daubechies qui offrent des filtres à moments nuls entiers. Parmi ceux-ci, figurent les filtres spline fractionnaires, moins courants dans la littérature, qui permettent d'obtenir des ondelettes aux moments nuls fractionnaires.

1.5.3 La transformée par ondelette discrète fractionnaire

Les ondelettes splines fractionnaires introduites par Blu et Unser reposent sur des filtres construits à partir des B-splines, qui sont des fonctions polynomiales par morceaux. La transformée de Fourier d'une B-spline est donnée par,

$$\hat{\beta}_\alpha(\omega) = \left(\frac{1 - e^{-i\omega}}{i\omega}\right)^{\alpha+1} \tag{1.36}$$

où $\omega = 2\pi f$. Par exemple pour $\alpha = 0$, on obtient,

$$\hat{\beta}_0(\omega) = \frac{1 - e^{-i\omega}}{i\omega} = e^{-i\frac{\omega}{2}} \frac{sin\left(\frac{\omega}{2}\right)}{\omega/2} \tag{1.37}$$

Cette expression est essentiellement celle d'un sinus cardinal pour $\frac{\omega}{2}$ et représente la transformée de Fourier de la B-spline d'ordre $\alpha = 0$ qui coïncide avec la fonction d'échelle de Haar (fonction créneau). Blu et Unser ont ensuite généralisé cette construction en introduisant une famille d'ondelettes basée sur les B-splines, satisfaisant une relation d'échelle.

En effet, l'équation 1.36 obéit à une relation à deux échelles,

$$\hat{\beta}_\alpha(2\omega) = \left(\frac{1-e^{-2i\omega}}{2i\omega}\right)^{\alpha+1} = \left(\frac{1-e^{-2i\omega}}{1-e^{-i\omega}}\right)^{\alpha+1} \frac{1}{2^{\alpha+1}} \left(\frac{1-e^{-i\omega}}{i\omega}\right)^{\alpha+1} \quad (1.38)$$
$$= H(\omega)\hat{\beta}_\alpha(\omega)$$

Ainsi, la version contractée de la fonction $\hat{\beta}_\alpha(\omega)$, notée $\hat{\beta}_\alpha(2\omega)$, s'obtient en multipliant $\hat{\beta}_\alpha(\omega)$ par un filtre $H(\omega)$. Pour obtenir une famille de fonctions d'échelle dont les versions translatées $H(\omega)$ sont orthogonales entre elles, on renormalise $H(\omega)$,

$$H(\omega) = \sqrt{2}\left(\frac{1+e^{-i\omega}}{2}\right)^{\alpha+1} \sqrt{\frac{A^{2\alpha+1}(e^{i\omega})}{A^{2\alpha+1}(e^{2i\omega})}} \quad (1.39)$$

où $A^\alpha(e^{j\omega}) = \sum_k \left|\hat{\beta}_\alpha(\omega + 2k\pi)\right|^2$. Cette normalisation assure ainsi une représentation non redondante du signal. À partir de la relation 1.33 on obtient alors le filtre passe-haut correspondant,

$$G(\omega) = e^{-i\omega}\sqrt{2}\left(\frac{1-e^{i\omega}}{2}\right)^{\alpha+1} \sqrt{\frac{A^{2\alpha+1}(-e^{-i\omega})}{A^{2\alpha+1}(-e^{-2i\omega})}} \quad (1.40)$$

Les filtres $H(\omega)$ et $G(\omega)$, sont orthogonaux entre eux. Cette propriété est essentielle, car elle permet de séparer efficacement l'information du signal à différentes échelles et d'obtenir des coefficients d'ondelettes peu corrélés. De plus, dans le filtre $G(\omega)$, le facteur $\left(\frac{1-e^{-i\omega}}{2}\right)^{\alpha+1}$ permet de filtrer les composantes polynomiales du signal jusqu'au degré α. Dans ce facteur, $e^{-i\omega} \cong 1 - i\omega$, ainsi, on a un comportement $\left(\frac{\omega}{2}\right)^{\alpha+1}$. Cette relation généralise l'équation 1.24, mais avec un exposant fractionnaire. Ce facteur se comporte comme une dérivée fractionnaire de degré $\alpha + 1$, car une dérivée correspond, dans le domaine fréquentiel, à une multiplication des coefficients par le facteur $(2\pi f)^{\alpha+1}$. En décomposant un signal à l'aide de ces filtres, chaque coefficient est décrit selon l'équation (Blu & Unser, 2003),

$$w_{j,k} \cong 2^{j\left(\alpha+\frac{3}{2}\right)} \partial^{\alpha+1} s\left(k2^j\right) \quad (1.41)$$

L'équation 1.41 met de l'avant la dérivée fractionnaire notée $\partial^{\alpha+1}$. On a alors une représentation où les coefficients par ondelettes sont associés à un ordre fractionnaire à toutes les échelles et à tous les instants du signal $s\left(k2^j\right)$.

1.6 Signaux rythmiques et l'algorithme Matching Pursuit

Une méthode introduite par Farrokhi & Daliri (2022) utilise les dérivées fractionnaires pour séparer les composantes apériodique et rythmique d'un signal EEG. Ils estiment l'activité apériodique β avec l'algorithme IRASA et appliquent une dérivée fractionnaire d'ordre $\frac{\beta}{2}$ au signal EEG complet, ce qui atténue l'activité apériodique. L'ordre est de $\frac{\beta}{2}$, puisque la puissance est le carré de l'amplitude. Ainsi, on obtient,

$$A(f) = \frac{1}{f^{\frac{\beta}{2}}} \tag{1.42}$$

Cette dérivée permet de détecter plus facilement les fréquences centrales des pics du spectre. Cependant, la dérivée fractionnaire s'applique au signal complet, contrairement aux filtres fractionnaires en ondelettes de Blu et d'Unser, qui permettent de calculer des dérivées fractionnaires localement et limitent ainsi la distorsion de phase. Cette différence est centrale dans le travail proposé au chapitre 2. Pour chaque fréquence centrale correspondant à un pic du spectre identifié, un signal oscillatoire est estimé. Ces composantes oscillatoires sont ensuite soustraites itérativement au signal EEG. Une fois l'ensemble des composantes oscillatoires retirées, le résidu correspond à la composante apériodique du signal.

Cette méthodologie iterative d'un algorithme « glouton » s'apparente, dans son principe, à l'algorithme du « Matching Pursuit » (MP), utilisé en EEG pour détecter des oscillations rythmiques caractéristiques du sommeil (P. J. Durka & Blinowska, 1995 ; Schönwald, de Santa-Helena, Rossatto, Chaves, & Gerhardt, 2006).

L'algorithme MP repose sur un « dictionnaire d'atomes » $\{D_i(t)\}$. Chaque « atome » d'indice i est un signal élémentaire localisé par une durée (d_i), à un instant (t_i) et une fréquence (f_i). Le dictionnaire est conçu à partir d'atomes qui représentent les rythmes oscillatoires à détecter. L'algorithme MP sélectionne itérativement l'atome d'un dictionnaire d'atomes $\{D_i(t)\}$ le plus corrélé à un signal résiduel $r_n(t)$. Au départ, $r_0(t)$ correspond au signal EEG.

À chaque itération, l'indice de l'atome présentant la plus forte corrélation avec le résidu est sélectionné,

$$i^* = argmax_i(|\langle r_n, D_i \rangle|) \tag{1.43}$$

La contribution de l'atome d'indice i^* est ensuite soustraite du signal résiduel et mise à jour pour l'itération suivante,

$$r_{n+1}(t) = r_n(t) - \langle r_n, D_{i^*} \rangle D_{i^*}(t) \tag{1.44}$$

Le processus est répété jusqu'à ce qu'un critère d'arrêt soit atteint. Pour chaque atome sélectionné $D_{i^*}(t)$, les fréquences caractéristiques ainsi que les positions temporelles correspondantes sont extraites. Étant donné l'ensemble des atomes $\{D_{1^*}, D_{2^*} \ldots . D_{k^*}\}$, on peut reconstruire un signal,

$$s^*(t) = \sum_{i^*=1}^{k^*} c_{i^*} D_{i^*}(t) \tag{1.45}$$

Cette somme pondérée des atomes sélectionnés est le signal $s^*(t)$ des rythmes détectés. L'algorithme MP s'adapte à la morphologie des rythmes oscillatoires selon le dictionnaire établi. Ainsi, on fera l'hypothèse, dans le chapitre 3, que l'algorithme MP sera plus approprié pour obtenir l'inventaire des rythmes en l'absence d'interférence avec une activité aperiodique.

1.7 L'activité apériodique du sommeil

En EEG clinique, différentes pathologies sont caractérisées par un ralentissement spectral de l'EEG, défini par une augmentation de l'activité lente (delta/thêta) et une diminution des rythmes rapides (alpha/bêta) du spectre et quantifié par ce ratio,

$$r = \frac{p_\delta + p_\theta}{p_\alpha + p_\beta} \tag{1.46}$$

Par exemple, les patients atteints d'Alzheimer présentent, durant le sommeil REM, une augmentation des ondes delta et thêta et une diminution des ondes alpha et bêta (Hassainia, Petit, Nielsen, & Gauthier, 2008). Ce ratio, bien qu'il tienne compte des composantes apériodique et rythmique, reflète surtout un changement de la composante apériodique, car celle-ci domine la distribution spectrale. Ainsi, plus la pente apériodique est élevée, plus le ratio (r) augmente.

Aujourd'hui, de nombreux travaux caractérisent ces composantes séparément afin de définir les états de vigilance, les pathologies et de mieux comprendre les mécanismes sous-jacents de l'activité cérébrale. Bien que l'origine de l'exposant d'échelle soit complexe, celui-ci subit des modifications mesurables pendant le sommeil**.** La composante apériodique du spectre varie selon les stades du sommeil, avec un exposant qui augmente de l'éveil au sommeil NREM et diminue du sommeil NREM au sommeil REM (Schneider et al., 2022). Par contre, une autre étude a mis en évidence une augmentation de l'exposant du stade NREM3 au sommeil REM, que ce soit en EEG intracrânien ou en EEG du scalp (Lendner et al., 2020). Cette divergence de résultats est probablement attribuable au fait que l'exposant est calculé sur des bandes de fréquence différentes dans ces travaux. L'exposant a été mesuré au cours des deux phases du sommeil REM tonique et phasique. Ainsi, l'exposant apériodique est plus élevé dans le sommeil REM phasique que dans le REM tonique lorsqu'il est mesuré entre 2 et 30 Hz (Rosenblum, Bogdány, et al., 2025). La pente varie également selon les cycles de sommeil (Rosenblum, Jafarzadeh Esfahani, et al., 2025) .

L'exposant reflète un processus physiologique, avec une diminution de l'exposant observée avec le vieillissement (Voytek et al., 2015). En effet, en sommeil NREM, l'exposant diminue avec l'âge, indépendamment du sexe et du quotient intellectuel (Bódizs et al., 2021). L'exposant diminue également avec l'âge pendant le sommeil REM, mais les hommes présentent des exposants plus faibles que les femmes à travers l'ensemble des stades du sommeil (Kozhemiako et al., 2022). Une autre étude a rapporté que l'exposant est plus élevé dans les régions postérieures pour les jeunes, mais qu'il tend à augmenter dans les régions antérieures avec l'âge (Favaro et al., 2023).

Sur le plan clinique, les patients souffrant de dépression sous médication ont montré des exposants plus faibles en NREM que dans leur état non médicamenté, ainsi que par rapport aux sujets contrôle à travers tous les stades du sommeil (Rosenblum et al., 2023). En comparant des conditions pathologiques, les sujets présentant des troubles du sommeil, en particulier la parasomnie, présentent une pente élevée par rapport aux sujets atteints d'épilepsie

hypermotrice pendant le sommeil NREM3 (Pani et al., 2021). Les patients souffrant d'insomnie ont une pente qui diminue durant le sommeil NREM par rapport aux sujets contrôles (Andrillon et al., 2020). Ceci pourrait indiquer une augmentation de l'excitabilité, caractéristique de l'hyperexcitabilité chez les patients souffrant d'insomnie (Andrillon et al., 2020). Toutefois, aucune différence de pente apériodique n'a été établie entre des sujets souffrant de stress et des sujets contrôles à l'aide d'un appareil EEG portatif (Blaskovich et al., 2024).

En sommeil NREM, Helfrich et al. (2021) proposent que les rythmes transitoires sont suivis d'une prédominance d'activité apériodique. À cet égard, ils s'appuient sur les travaux d'Antony et al. (2018), qui ont montré qu'un signal auditif présenté environ 2.5 secondes après un fuseau favorisait la rétention de la mémoire, tandis qu'un signal présenté immédiatement après (< 1 s) perturbait la consolidation de la mémoire. Sur cette base, Helfrich et al. (2021) suggèrent que l'activité apériodique favoriserait l'intégration de l'information au sein des réseaux neuronaux, tandis que l'activité rythmique favoriserait la consolidation de la mémoire. Une autre étude a montré que l'exposant d'échelle augmente pendant le sommeil REM et que cette augmentation est corrélée à une meilleure rétention de la mémoire (Lendner et al., 2023).

Ces études démontrent la complexité de l'activité apériodique et mettent en évidence son rôle clinique. Toutefois, en estimant l'activité apériodique à partir du spectre de Fourier, ces travaux ne répondent pas à la question de l'interférence entre ces processus. Par conséquent, il faut étendre ces analyses au domaine temporel du signal afin de résoudre l'interférence entre les composantes apériodique et rythmique et permettre de mieux décoder les mécanismes sous-jacents à ces composantes.

1.8 L'analyse multifractale

L'analyse multifractale est un modèle capable de rendre compte de l'activité apériodique. Elle consiste à décrire un signal par un ensemble d'exposants d'échelle reflétant ses régularités

locales. Il est possible de calculer une fonction de structure généralisant les moments statistiques des coefficients d'ondelette $L_{j,k}$ à chaque échelle,

$$S_q(j) = \frac{1}{N_j}\sum_k |L(j,k)|^q \tag{1.47}$$

N_j est le nombre de coefficients à l'échelle j. $L_{j,k}$ sont des coefficients leaders qui sont définis comme la valeur absolue maximale parmi un ensemble spécifique de coefficients voisins afin d'obtenir une caractérisation robuste de l'invariance d'échelle (Jaffard, Lashermes, & Abry, 2007). Ainsi, pour chaque valeur q ($q \in R^*$), on évalue $S_q(j)$ pour chaque échelle 2^j. En présence d'invariance d'échelle, on montre que la fonction de structure suit une loi de puissance (Wendt, Abry, & Jaffard, 2007),

$$S_q(j) \cong C_q 2^{\zeta(q)j} \tag{1.48}$$

où $\zeta(q)$ est la fonction d'exposant d'échelle. Ainsi,

$$log_2\left(S_q(j)\right) \cong \zeta(q)j + log_2(C_q) \tag{1.49}$$

Pour chaque valeur q, $log_2\left(S_q(j)\right)$ présente une relation linéaire où $\zeta(q)$ corresponds à la pente et $log_2(C_q)$ à l'ordonnée à l'origine. De plus, $\zeta(q)$ peut-être définie à partir des premiers termes d'un développement de Taylor,

$$\zeta(q) \cong c_1 q + c_2 \frac{q^2}{2} \tag{1.50}$$

Le premier paramètre c_1 caractérise l'auto-similarité du signal des échelles avec un exposant unique, tandis que c_2 (négatif) mesure la dispersion multifractale. À partir du formalisme multifractale, la relation entre l'exposant d'échelle β et c_1 est établie selon la démonstration suivante. Dans le cas dit « monofractal » ($c_2 = 0$), on a,

$$S_2(j) \cong C_2 2^{\zeta(2)j} \cong C_2 2^{2c_1 j} \cong C_2 (2^j)^{2c_1} \tag{1.51}$$

L'échelle 2^j étant inversement proportionnelle à la fréquence $\left(2^j \propto \frac{1}{f_j}\right)$, on obtient,

$$S_2(j) \sim C_2 \frac{1}{f_j^{2c_1}} \tag{1.52}$$

et par conséquent,

$$\beta = 2c_1 \tag{1.53}$$

Un signal physiologique n'a jamais un $c_2 = 0$. L'analyse multifractale permettrait également de caractériser statistiquement l'étalement de l'exposant c_1 avec le parametre c_2.

1.9 Micro-états

Très tôt, l'analyse multifractale a été appliquée à l'électrophysiologie (Lopes & Betrouni, 2009), mais plus récemment cette analyse a été appliquée à la dynamique du potentiel électrique déployé sur le scalp (Van De Ville et al., 2010). Pour caractériser ce potentiel de scalp, les micro-états ont été définis par un ensemble fini de topographies mesurant la distribution spatiale du potentiel électrique (Lehmann, Ozaki, & Pal, 1987). On s'intéresse aux topographies et à la persistance de celles-ci. Les micro-états sont stables pendant 60 à 120 ms (Koenig et al., 2002). Les micro-états ont d'abord été étudiés à l'éveil, au repos. Quelques études ont également analysé les micro-états durant le sommeil (Bréchet, Brunet, Perogamvros, Tononi, & Michel, 2020 ; Brodbeck et al., 2012 ; Kuhn et al., 2015 ; Xu et al., 2020).

Les micro-états reposent sur le Global Field Power (GFP) défini par la variance du potentiel électrique mesuré à travers les électrodes à chaque instant t,

$$GFP(t) = \sqrt{\frac{1}{n}\sum_{i=1}^{n}\left(V_i(t) - \bar{v}(t)\right)^2} \tag{1.54}$$

où $V_i(t)$ correspond au potentiel électrique d'une électrode au temps t, $\bar{v}(t)$ correspond à la moyenne des électrodes au temps t et n représente le nombre d'électrodes.

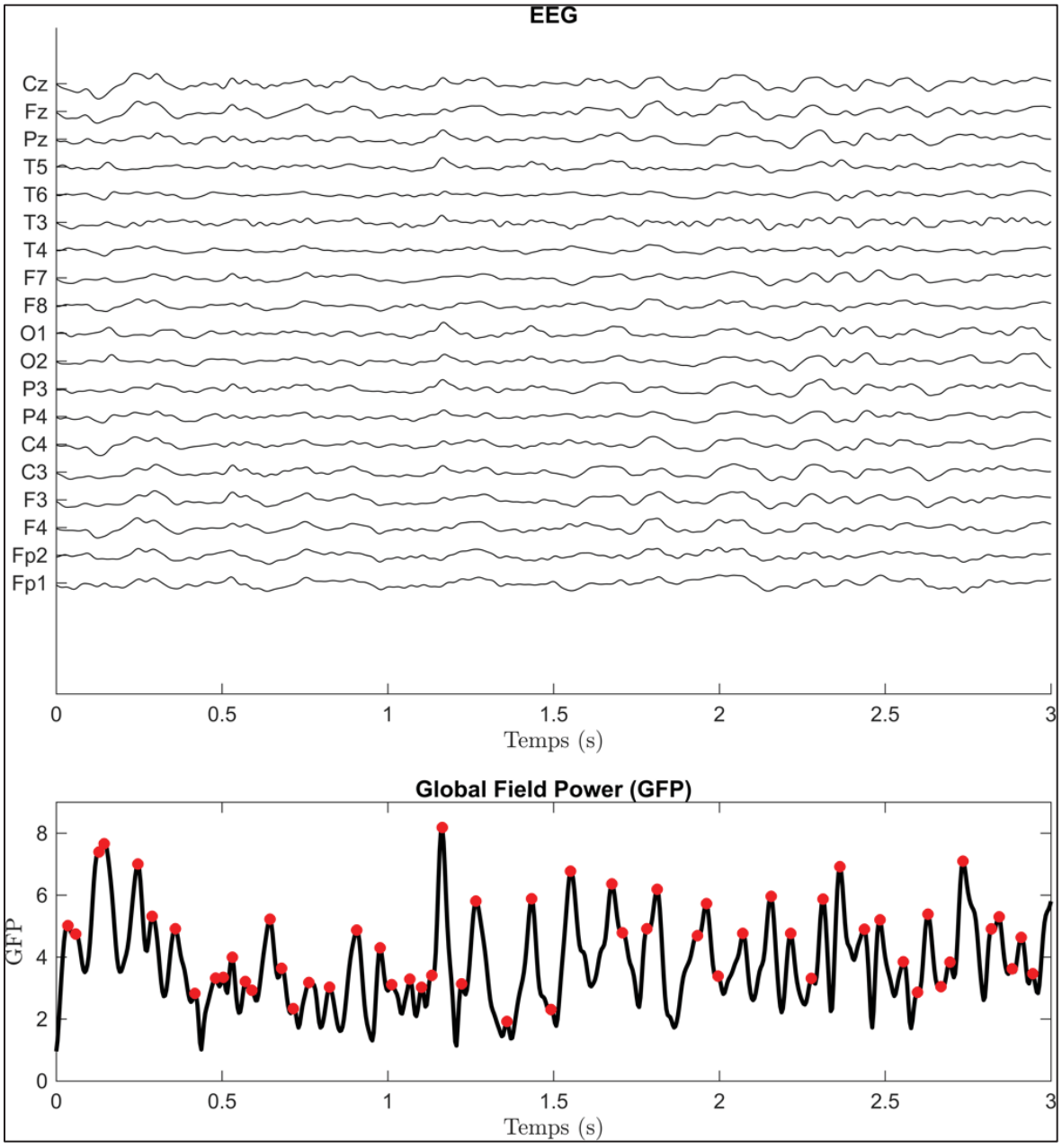

Figure 1.10 Segment d'EEG de 3 secondes, enregistré sur 19 électrodes, avec l'évolution temporelle du GFP. Les points rouges indiquent les maxima locaux du GFP

Les potentiels du scalp associés aux maxima locaux du GFP sont inventoriés, puis classés à l'aide d'un algorithme de clustering (k-means modifié). Chaque classe permet ainsi d'obtenir un nombre de topographies canoniques (quatre à sept) qui caractérisent la variance des données. Les topographies canoniques sont nommées selon les lettres de l'alphabet (A, B, C, D). Le micro-état A présente une orientation postérieure gauche, antérieure droite, le micro-

état B, une orientation postérieure droite, antérieure gauche, le micro-état C, une orientation antérieure postérieure et le micro-état D, un maximum central (Michel & Koenig, 2018).

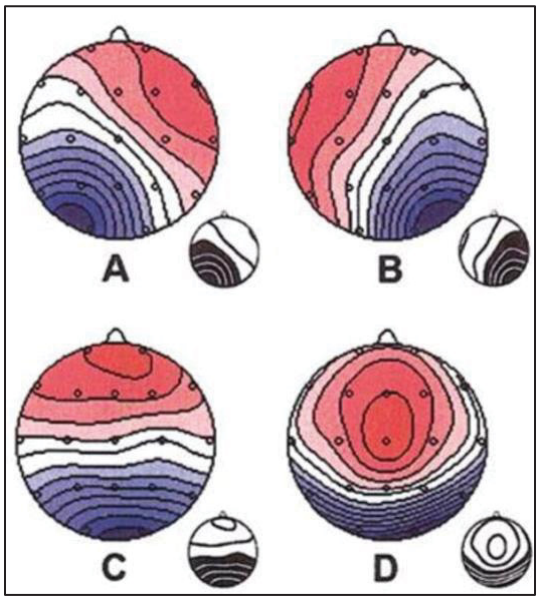

Figure 1.11 Illustrations des
quatre micro-états canoniques.
Tiré de Koenig et al. (2002)

En général, les micro-états canoniques sont assez reproductibles d'une étude à une autre. Ce sont donc des caractéristiques fondamentales de l'activité bioélectrique du cerveau. Les études mettent en correspondance leurs topographies avec celles rapportées dans la littérature, afin de favoriser la comparaison entre les travaux. Finalement, pour chaque échantillon temporel, on associe le micro-état le plus corrélé aux topographies EEG. On obtient ainsi un codage de la séquence des topographies à l'aide d'un petit nombre de topographies canoniques issues du clustering.

Un travail important de Britz et al. (2010) a établi la conjecture selon laquelle les micro-états A-D sont corrélés à des réseaux fonctionnels à l'aide d'enregistrements simultanés EEG-IRMf à l'état de repos. Un réseau fonctionnel regroupe un ensemble de régions cérébrales synchronisées lors de certaines fonctions à l'état de repos. Par exemple, le mode par défaut (DMN) est un réseau actif dans l'état de repos (Raichle, 2015). Il recrute les régions du cortex

préfrontal médian antérieur, du cortex cingulaire postérieur et du gyrus angulaire. Le mode de saillance antérieur impliquant des régions associées au traitement des réponses à des stimuli (Seeley et al., 2007). Il recrute des régions cérébrales composées de l'insula antérieure (IA) et du cortex cingulaire antérieur dorsal (dACC). On retrouve également le réseau auditif, le réseau visuel, le réseau du contrôle exécutif central et le réseau d'attention dorsal.

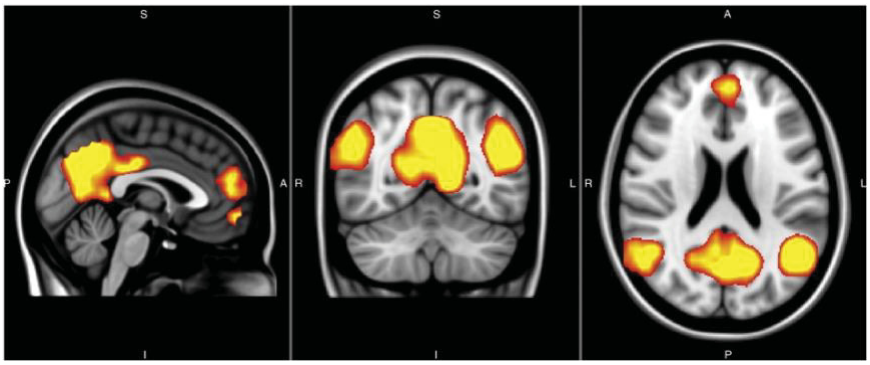

Figure 1.12 Exemple du réseaux fonctionnel du mode par défaut
Tiré de Hafkemeijer et al. (2012)

Selon Britz et al. (2010), le micro-état A est associé au réseau auditif, le micro-état B correspond au réseau visuel, le micro-état C au réseau de saillance et le micro-état D aux réseaux du DMN. Depuis ce travail, des études ont tenté de reproduire ces correspondances, mais ont rapporté des divergences. En effet, une étude a plutôt montré que les micro-états ne correspondent pas à un seul réseau fonctionnel, mais peuvent être corrélés à plusieurs réseaux fonctionnels (Yuan, Zotev, Phillips, Drevets, & Bodurka, 2012). De plus, Custo et al. (2017) ont identifié sept micro-états (A-G). Ils ont constaté que les micro-états A-B-F-D correspondent à ceux de Britz et al. (2010). Ils ont attribué les micro-états C-E-F à des régions du DMN et le micro-état G, au réseau sensorimoteur. Une étude sur le sommeil a mis en évidence une association entre les micro-états B-C-D, respectivement associés au réseau auditif, au réseau de contrôle exécutif et au réseau de saillance (Xu et al., 2020). De plus, en caractérisant l'organisation temporelle des micro-états (durée moyenne, occurrence, durée totale, variance de chaque micro-état et les probabilités de transition d'un micro-état à un autre), on pourrait décrire la dynamique des réseaux fonctionnels associés aux micro-états (Khanna, Pascual-Leone, Michel, & Farzan, 2015).

Récemment, des travaux ont également cherché à caractériser le contenu fréquentiel associé à la dynamique des micro-états. Les approches proposées consistent à calculer les plans temps-fréquence des signaux EEG et à extraire, à l'aide de séquences de micro-états, la puissance à chaque instant des occurrences des micro-états (Javed, Croce, Zappasodi, & Gratta, 2019 ; Li et al., 2021). Une étude portant sur le sommeil a comparé l'information mutuelle (AIF) des séquences de micro-états à la fonction d'autocorrélation (ACF) des composantes principales des signaux EEG (Wiemers, Laufs, & von Wegner, 2024). Les études ont montré que le contenu fréquentiel des séquences de micro-états associées aux signaux EEG comprend des rythmes caractéristiques de l'état de vigilance.

Une analyse multifractale d'enregistrements EEG d'individus au repos, portant sur la caractérisation des séquences de micro-états, a montré que ces séquences sont autosimilaires (Van De Ville et al., 2010). Ils définissent un signal qui encode la dynamique des micro-états en codant la séquence des micro-états par +1 et -1 pour deux groupes (i.e., A-B et C-D). Cette partition est arbitraire et n'a pas d'incidence sur les résultats de l'étude. Ils ont ainsi obtenu une série temporelle finale en calculant la somme cumulative des séquences de micro-états encodées. L'analyse multifractale de cette série temporelle montre que la dynamique des micro-états obtenue au repos est autosimilaire. Étant donné que les micro-états sont possiblement liés à des réseaux, la dynamique apériodique pourrait favoriser la transition entre différents réseaux fonctionnels.

La majorité des études caractérisent l'activité apériodique à partir des données d'une seule électrode, ce qui limite la compréhension de son rôle à l'échelle spatiale. Des méthodes mesurant la composante apériodique en exploitant l'information de toutes les électrodes permettraient de mieux comprendre les processus neuronaux à grande échelle. À ce jour, aucune étude n'a caractérisé la composante apériodique de la dynamique des micro-états durant le sommeil. Ceci permettrait de mieux comprendre comment les réseaux recrutés durant le sommeil s'organisent et d'évaluer potentiellement des troubles du sommeil.

1.10 Lomb-Scargle

Les séquences des micro-états sont échantillonnées a des instants t_n espacés de façon irrégulière. Ainsi, les méthodes classiques d'analyse spectrale, fondées sur la FFT, ne peuvent pas être utilisées pour obtenir la puissance spectrale. L'algorithme de Lomb-Scargle $P_{LS}(f)$, conçu pour l'analyse spectrale de signaux $s(t_n)$ irrégulièrement échantillonnés (Scargle, 1982), s'impose donc naturellement dans ce contexte. Afin de produire une analyse de Fourier habituelle pour des signaux $s(t_n)$ irrégulièrement échantillonnés, on adopte les contraintes suivantes (VanderPlas, 2018) :

1) Lorsque les données sont échantillonnées régulièrement, $P_{LS}(f)$ doit correspondre à l'analyse spectrale classique de Fourier
2) $P_{LS}(f)$ ne doit pas dépendre d'un décalage temporel.

On propose, dans la section suivante, la démonstration de l'algorithme de Lomb-Scargle.

1.10.1 La preuve de Lomb-Scargle

Pour chaque fréquence f, on considère un modèle sinusoïdal de la forme,

$$y(t;f) = A_f \cos 2\pi f\,(t-\tau_f) + B_f \sin 2\pi f\,(t-\tau_f) \tag{1.55}$$

aux données irrégulièrement espacées y_n observées aux instants t_n, $n = 1,2,\dots,N$. $\tau_f$est un paramètre de déphasage qui sera calculé tel que la meilleure approximation des données est obtenue par les moindres carrés,

$$(A_f, B_f) = Argmin_\theta \left(y_n - y(t_n;f)\right)^2 = (Y - X\theta)^t (Y - X\theta) \tag{1.56}$$

où on a défini :

$$Y = \begin{bmatrix} y_1 \\ \vdots \\ y_N \end{bmatrix};\ X = \begin{bmatrix} \cos 2\pi f(t_1-\tau_f) & \sin 2\pi f(t_1-\tau_f) \\ \vdots & \vdots \\ \cos 2\pi f(t_N-\tau_f) & \sin 2\pi f(t_N-\tau_f) \end{bmatrix} \text{ et } \theta = \begin{bmatrix} A_f \\ B_f \end{bmatrix} \tag{1.57}$$

La minimisation optimale est de la forme,

$$\theta^* = (X^t X)^{-1} X^t Y \tag{1.58}$$

où l'opération matricielle $X^t\ X$ est,

$$X^t\ X = \begin{bmatrix} \sum_{n=1}^{N} c_n^2 & \sum_{n=1}^{N} c_n s_n \\ \sum_{n=1}^{N} c_n s_n & \sum_{n=1}^{N} s_n^2 \end{bmatrix} \tag{1.59}$$

Avec $c_n = \cos 2\pi f\big(t_n - \tau_f\big)$, $s_n = \sin 2\pi f\big(t_n - \tau_f\big)$ et

$c_n s_n = \cos 2\pi f(t_n - \tau_f) \sin(2\pi f\big(t_n - \tau_f\big).$

Dans cette matrice, on a,

$$\begin{aligned} \sum_{n=1}^{N} c_n s_n &= \sum_{n=1}^{N} \frac{1}{2} \sin\big(4\pi f t_n - 4\pi f \tau_f\big) \\ &= \sum_{n=1}^{N} \frac{1}{2} [\sin(4\pi f t_n) \cos\big(4\pi f \tau_f\big) - \cos\big(4\pi f \tau_f\big) \sin(4\pi f t_n)] \\ &= \frac{1}{2}\left[sin\ 4\pi f \tau_f \sum_{n=1}^{N} \cos 4\pi f t_n - \cos 4\pi f \tau_f \sum_{n=1}^{N} \sin 4\pi f t_n\right] \end{aligned} \tag{1.60}$$

On constate ainsi que, pour une valeur de τ_f, on peut annuler $\sum_{n=1}^{N} c_n s_n$. En effet,

$$\begin{aligned} \frac{1}{2}\left[\sin 4\pi f \tau_f \sum_{n=1}^{N} \cos 4\pi f t_n - \cos 4\pi f \tau_f \sum_{n=1}^{N} \sin 4\pi f t_n\right] &= 0 \\ \frac{\sin 4\pi f \tau_f}{\cos 4\pi f \tau_f} &= \frac{\sum_{n=1}^{N} \sin 4\pi f t_n}{\sum_{n=1}^{N} \cos 4\pi f t_n} \\ \tan\ (4\pi f \tau_f) &= \frac{\sum_{n=1}^{N} \sin 4\pi f t_n}{\sum_{n=1}^{N} \cos 4\pi f t_n} \end{aligned} \tag{1.61}$$

Donc,

$$\tau_f = \frac{1}{4\pi f}\ arctan \frac{\sum_{n=1}^{N} sin\ 4\pi f t_n}{\sum_{n=1}^{N} cos\ 4\pi f t_n} \tag{1.62}$$

La matrice X^tX devient alors diagonale $\begin{bmatrix} C & \\ & S \end{bmatrix}$ avec $C = \sum_{n=1}^{N} c_n^2$ et $S = \sum_{n=1}^{N} s_n^2$. On obtient ainsi,

$$\begin{bmatrix} A_f^* \\ B_f^* \end{bmatrix} = \begin{bmatrix} 1/C & 0 \\ 0 & 1/S \end{bmatrix} \begin{bmatrix} \sum_{n=1}^{N} y_n c_n \\ \sum_{n=1}^{N} y_n s_n \end{bmatrix} \tag{1.63}$$

c'est-à-dire,

$$\begin{aligned} A_f^* &= \tfrac{1}{C}\textstyle\sum_{n=1}^{N} y_n c_n = \tfrac{1}{C}\sum_{n=1}^{N} y_n \cos 2\pi f\left(t_n - \tau_f\right) \\ B_f^* &= \frac{1}{S}\sum_{n=1}^{N} y_n s_n = \frac{1}{S}\sum_{n=1}^{N} y_n \sin 2\pi f\left(t_n - \tau_f\right) \end{aligned} \tag{1.64}$$

Pour finalement obtenir la formule Lomb-Scargle,

$$P_{LS}(f) = \frac{1}{2}\left[\frac{\left[\sum_{n=1}^{N} y_n \cos 2\pi f\left(t_n - \tau_f\right)\right]^2}{\sum_{n=1}^{N} \cos 2\pi f\left(t_n - \tau_f\right)^2} + \frac{\left[\sum_{n=1}^{N} y_n \sin 2\pi f\left(t_n - \tau_f\right)\right]^2}{\sum_{n=1}^{N} \sin 2\pi f\left(t_n - \tau_f\right)^2}\right] \tag{1.65}$$

1.10.2 Relation entre la transformée de Fourier et Lomb-Scargle

Cette section vise à montrer qu'à partir de Lomb-Scargle, lorsqu'un signal est échantillonné régulièrement, on retrouve la formule classique de Fourier. Pour un signal régulièrement échantillonné, on a la situation suivante,

$$f_k = \frac{kf_s}{N} \text{ où } k = 0{,}1 \dots N-1 \qquad (1.66)$$
$$t_n = \frac{n}{f_s} \text{ où } n = 0{,}1 \dots N-1$$

Lorsque les signaux sont réguliers, $\tau_f = 0$. Pour déterminer A_f ; il faut d'abord simplifier,

$$\sum_{n=0}^{N-1} \cos^2(2\pi f(t_n)) \qquad (1.67)$$

$$\sum_{n=0}^{N-1} \cos^2\left(2\pi \frac{kn}{N}\right) = \sum_{n=0}^{N-1} \frac{\cos\left(4\pi \frac{kn}{N}\right)}{2} + \frac{1}{2}$$
$$= \frac{1}{2}\sum_{n=0}^{N-1} \Re\left(e^{i4\pi\frac{kn}{N}}\right) + \frac{N}{2}$$

Si on pose $z_n = e^{i2\pi\frac{kn}{N}}$, cette expression devient,

$$\frac{1}{2}\Re\left(\sum_{n=0}^{N-1} z_n^2\right) + \frac{N}{2} = \frac{1}{2}\Re\left(\frac{1-z^{2N}}{1-z^2}\right) + \frac{N}{2} \qquad (1.68)$$

Cette équation est valide pour $z^2 \neq 1$. On peut déterminer que, $z^{2N} = e^{i4\pi k} = 1$ et par conséquent, $\sum_{n=0}^{N-1} z^{2n} = 0$. On obtient ainsi,

$$A_f^2 = \frac{2}{N} \qquad (1.69)$$

Le même processus est répété pour B_f, pour lequel on obtient: $B_f^2 = \frac{2}{N}$. Alors, si $A_f^2 = \frac{2}{N}$, $B_f^2 = \frac{2}{N}$ et $\tau_f = 0$, la formule de Lomb-Scargle est,

$$P_{LS}(f) = \frac{1}{N}\left(\sum_n s(t_n)\cos(2\pi f(t_n))\right)^2 + \frac{1}{N}\left(\sum_n s(t_n)\sin(2\pi f(t_n))\right)^2 \qquad (1.70)$$

et correspond bien à la formule de Fourier classique pour un échantillonnage régulier.

CHAPITRE 2

RHYTHMS AND BACKGROUND (RNB): THE SPECTROSCOPY OF SLEEP RECORDINGS

Michael Foti[1], Jonathan Dubé[2,3],Stéphane Jaffard[4], Véronique Latreille[5], Birgit Frauscher[6], Julie Carrier[1,2], Jean-Marc Lina[1,2,7]

[1] Département de génie électrique, École de technologie supérieure, Montréal, QC, H3C1K3, Canada
[2] Département de psychologie, Université de Montréal, Montréal, QC, H3C1J7, Canada
[3] Centre d'Études Avancées en Médecine du sommeil, Hop. Sacré-Cœur de Montréal, Montréal, QC, H4J1C5, Canada
[4] LAMA, Université Paris-EST Créteil, France
[6] Département de neurologie et neurochirurgie, Institut-Hôpital neurologiques de Montréal, Université de McGill, Montréal, QC, H3A2B4, Canada
[7] Centre de Recherches Mathématique, Université de Montréal, Montréal, QC, H3C1J7, Canada

Article publié dans la revue *eNeuro* le 13 janvier 2026, disponible au https://doi.org/10.1523/ENEURO.0235-25.2025

2.1 Abstract

Non-rapid eye movement (NREM) sleep is characterized by the interaction of multiple oscillations essential for memory consolidation, alongside a dynamic arrhythmic 1/f scale-free background that may also contribute to its functions. Recent spectral parametrization methods, such as FOOOF (Fitting-One-and-Over-f) and IRASA, enable the dissociation of rhythmic and arrhythmic components in the spectral domain; however, they do not resolve these processes in the time domain. Instantaneous measures of frequency, amplitude, and phase-amplitude coupling are thus still confounded by fluctuations in arrhythmic activity. This limitation represents a significant pitfall for studies of NREM sleep, often relying on instantaneous estimates to investigate the coupling of specific oscillations. To address this limitation, we introduce 'Rhythms & Background' (*RnB*), a novel wavelet-based methodology designed to dynamically denoise time-series data of arrhythmic interference. This enables the extraction of purely rhythmic time series, suitable for enhanced time-domain analyses of sleep rhythms. We

first validate *RnB* through simulations, demonstrating its robust performance in accurately estimating spectral profiles of individual and multiple oscillations across a range of arrhythmic conditions. We then apply *RnB* to publicly available intracranial EEG sleep recordings, showing that it provides an improved spectral and time-domain representation of hallmark NREM rhythms. Finally, we demonstrate that *RnB* significantly enhances the assessment of phase-amplitude coupling between cardinal NREM oscillations, outperforming traditional methods that conflate rhythmic and arrhythmic components. This methodological advance offers a substantial improvement in the analysis of sleep oscillations, providing greater precision in the study of rhythmic activity critical to NREM sleep functions.

2.2 Introduction

Brain rhythms from electroencephalograms (EEG) and other electrophysiological techniques reveal the synchronized rhythmic activity from neural ensembles. These rhythms are often identified using the spectral peaks of the power spectrum (Buzsáki, 2004). A noteworthy case is non-rapid eye movement (NREM) sleep, which is characterized by cardinal rhythms such as sleep slow waves (SSWs, 0.5-4 Hz, delta), theta bursts (6–10 Hz), sleep spindles (8–16 Hz, sigma), and sharp-wave ripples (100–200 Hz). NREM sleep rhythms are organized in complex wave sequences, with organized phase-amplitude coupling across frequencies occurring locally and between remote brain regions (Helfrich et al., 2019 ; Klinzing et al., 2016). For instance, sleep spindles are organized by the phase of SSWs and occur preferentially during the transition period of SSWs towards their upstate. Phase-amplitude coupling between delta and sigma rhythms during NREM sleep is increasingly recognized as a crucial component of overnight memory consolidation, and the loss of this phase coupling in aging may contribute to impaired memory consolidation (Helfrich, Mander, Jagust, Knight, & Walker, 2018).

New evidence suggests that “arrhythmic” brain activity recorded from the EEG plays complementary roles to brain rhythms for NREM sleep functions (Helfrich et al., 2021). Arrhythmic activity recruits a broad range of frequencies and is usually expressed as a $1/f^{\beta}$ decay in the power spectral density (He, 2014). This “scale-free” arrhythmic component is

usually estimated using the spectral slope (β) expressed in the log-log power spectrum. The steepness of β has been shown to change across sleep stages (Helfrich et al., 2021 ; Kozhemiako et al., 2022 ; Lendner et al., 2020 ; Niethard, Brodt, & Born, 2021), and to show age-dependent changes, which can predict cognitive impairment (Finley et al., 2024 ; Hernandez et al., 2024). Importantly, changes in β may alter the spectral peaks' characteristics in the Fourier domain typically attributed to brain rhythms. For instance, older humans exhibit higher fast-frequency power in their EEG spectrum due to a flatter β slope, rather than increased fast oscillations (Voytek et al., 2015). Methods such as Fitting-Oscillations-One-and-Over-F (FOOOF) and Irregular Resampling Auto Spectral Analysis (IRASA) have been recently introduced to dissociate rhythmic and arrhythmic changes in the power spectrum, respectively from their peaks and β characteristics (Donoghue et al., 2020 ; Wen & Liu, 2016). Rightly so, these methods are widely used across neuroscience (Donoghue, Schaworonkow, & Voytek, 2022 ; Ostlund et al., 2022).

At the signal level, arrhythmicity manifests as ubiquitous 'desynchronized' scale-free fluctuations in electrophysiological recordings visible "in between" transient rhythmic oscillations, and on which they are also superimposed (Helfrich et al., 2021). These scale-free brain fluctuations introduce noise into multiple signal processing methods by reducing the reliability of phase and amplitude narrowband estimates associated with brain rhythms (Donoghue et al., 2022 ; Jurkiewicz, Hunt, & Żygierewicz, 2021). As scale-free power dominates in lower frequencies, slow fluctuations create transient events that are erroneously detected as slow waves (Samaha & Cohen, 2022). Although methods such as FOOOF and IRASA are increasingly used to distinguish rhythmic and arrhythmic activity at the level of the power spectrum (Pani, Saba, & Fraschini, 2022), no method currently addresses the disentanglement of rhythmic processes from the arrhythmic background at the signal level.
Here, we introduce *Rhythms & Background* (RnB), a wavelet-based method to extract a rhythmic time series in which the arrhythmic contribution is removed. Our method attenuates the $1/f^{\beta}$ contribution at the level of wavelet coefficients in the "time-scale" framework, allowing the synthesis of a new time series, free from the arrhythmic background. This series may then be used in ulterior signal processing pipelines, such as for the detection and coupling

analyses of purely rhythmic events. We validated *RnB* using realistic simulations and applied it to intracranial NREM sleep recordings to demonstrate that it improves the characterization phase-amplitude coupling between delta and sigma rhythms.

2.3 Materials and methods

2.3.1 From the spectral to the wavelet paradigm

The objective of this work is to extract as time series the rhythmic activity embedded in electrophysiological signals, in which the ubiquitous $1/f$ arrhythmic background is attenuated. We posit that the power spectrum of any signal can be decomposed into a scale-free background component and a distinct rhythmic contribution. On the Fourier spectral side, this can be formalized as:

$$\Gamma(f) = P(f)\, e^{R(f)} \tag{2.1}$$

where $P(f) = c/f^{\beta}$ accounts for arrhythmicity (with c as a positive constant and a 'scaling exponent' β) that will govern the decay of the power spectrum, while $R(f)$ represents oscillatory activity. By expanding the exponential, this model is equivalent to the following expression,

$$\Gamma(f) \approx \frac{c}{f^{\beta}} + c\, f^{-\beta} R(f) + \cdots \tag{2.2}$$

where the first term $\frac{c}{f^{\beta}}$ represents the scale-free background, and the second term $c\, f^{-\beta} R(f)$, accounts for the rhythmic contribution. It is noteworthy that this contribution is defined as a product between two factors: a narrowband rhythmic process $R(f)$; and the concurrent background $c\, f^{-\beta}$. The rhythmic term ($c\, f^{-\beta} R(f)$), can thus be understood as a *resonance* within a neuronal dynamic system, in which rhythms simultaneously emerge from and are stabilized by background activity (Hahn, Bujan, Frégnac, Aertsen, & Kumar, 2014 ; Tchumatchenko & Clopath, 2014). In the frequency domain (i.e. power spectrum), this interaction may give rise to a Gaussian peak, characteristic of oscillatory processes captured by spectral parameterization methods, provided that $R(f)$ decays rapidly at low frequencies.

Spectral whitening approaches such as IRASA (Wen & Liu, 2016) proposed to estimate a data-driven spectral filter $Q(f) \approx P(f)^{-1} \approx f^{\beta}$ acting on $\Gamma(f)$. In their method, the scaling exponent β is estimated through irregular resampling on an epoch-per-epoch basis and subsequently filtered with an epoch-wise filter $Q_i(f)$. Then, the rhythmic factor $e^{R^*(f)}$ is estimated by averaging the residual spectra across multiple epochs "i":

$$e^{R^*(f)} = \langle Q_i(f)\ \Gamma_i(f) \rangle \tag{2.3}$$

However, such methods operate only in the frequency domain, and the resulting "rhythmic spectra" cannot be used for time-resolved analyses. *RnB* translates the model above into a wavelet framework, using the "time-scale" decomposition of the signal. The upcoming section will give a detailed mathematical description of the algorithm; here, we provide a didactic and integrative overview.

Wavelets are transient "little waves" of a specific scale localized in time (Fig. 2.1A). Like a "zoom" function, wavelets at small temporal scales capture fast transient fluctuations, whereas wavelets at larger scales capture slower oscillations. The wavelet coefficients are thus defined by correlating a signal with wavelets at different scales and time position. This result in a "time-scale" decomposition of a signal, with wavelets coefficients expanded across scales and time (Fig. 2.1 B-2.1 C). Both the scale-free (arrhythmic) background and the scale-dependent (rhythmic) component contributes to each wavelet coefficient in the time-scale decomposition. The original contribution of *RnB* is to remove the scale-free contribution from each coefficient, preserving rhythmic activity in the coefficients.

This is achieved in two successive steps: first, the analysis of the original time series, and second, the synthesis of the rhythmic time series. During the analysis of the "original" time series, the scaling exponent (β) will be estimated from the wavelet power across all scales within each epoch (e.g., Fig. 2.1 C–D for NREM sleep). Because of their sensitivity to scaling properties, wavelets are uniquely suited to characterize the scale invariance inherent to electrophysiological recordings (Abry, Wendt, Jaffard, & Didier, 2019). This scale-free contribution will then be attenuated by removing the influence of β from all wavelet coefficients in the time-scale expansion, preserving only scale-dependent rhythmic activity in

the “filtered” representation (Fig. 2.1 E–F). This procedure yields a “rhythmic time series”, providing a substrate for further analyses of oscillatory activity (Fig. 2.1 G). Mathematically, the scale-free contribution is removed from the coefficients via a fractional differentiation operation grounded in the properties of the spline wavelet basis (Unser & Blu, 1999), as detailed in the next section.

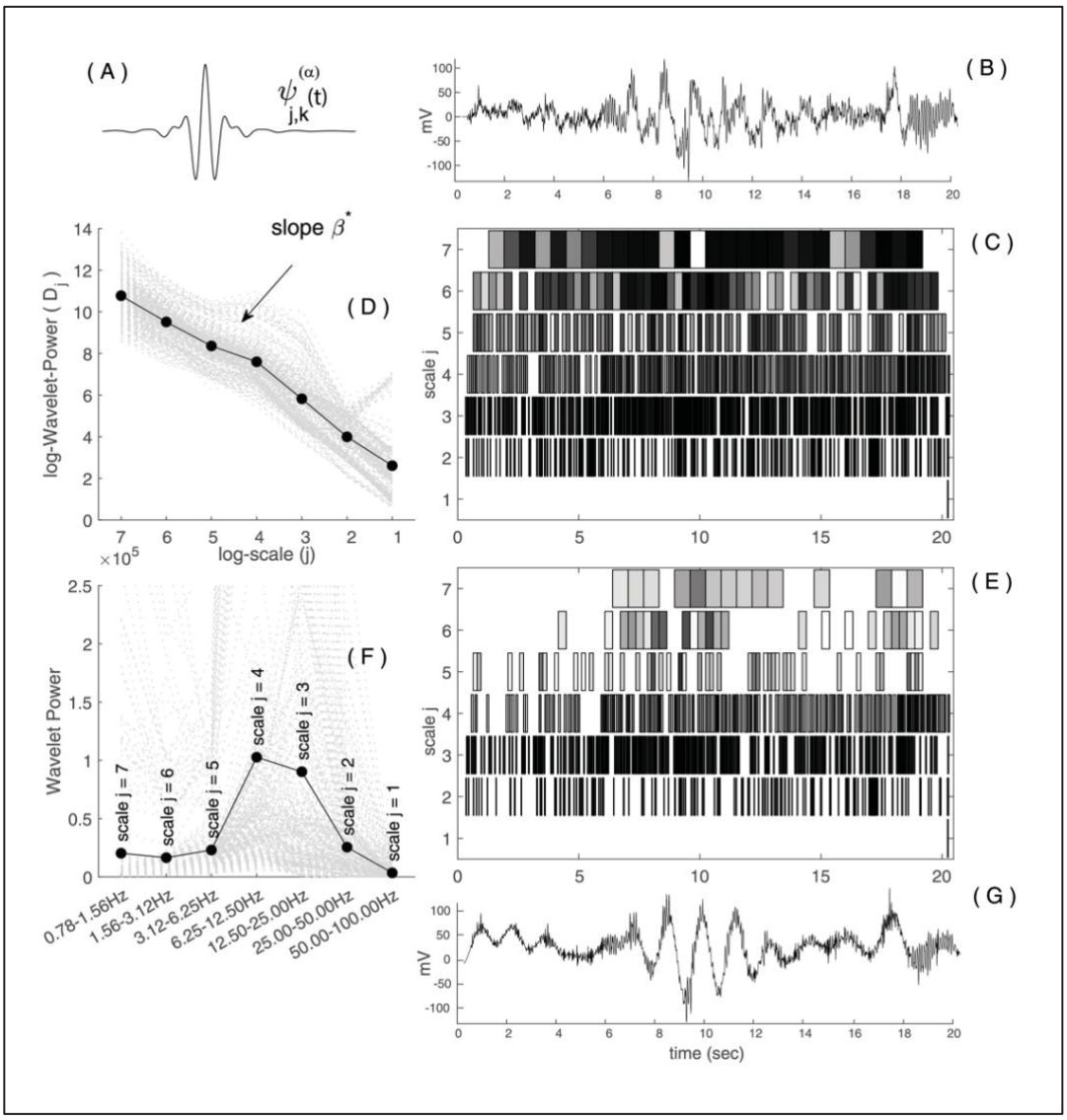

Figure 2.1 Time-scale wavelet framework

2.3.2 'Mother wavelet', wavelet family and time-scale expansion of a signal

A "mother wavelet" $\psi^{(\alpha)}(t)$ is a localized transient function (finite duration), with oscillations centered around a characteristic frequency f_0 (Fig. 2.1 A). Furthermore, this mother wavelet is characterized by a "regularity" parameter α which governs its behavior at low-frequency ($\sim f^{1+\alpha}$). Intuitively, α reflects how smooth the wavelet is: low α values allow the wavelet to capture abrupt transients, whereas higher values provide smoother functions that more effectively represent recurrent oscillatory activity. Given such a 'mother wavelet', a collection of rescaled (scales $2^j, j = 1,2, \ldots$) and time shifted (parameter k) wavelets is defined by

$$\psi_{j,k}^{(\alpha)}(t) = \frac{1}{\sqrt{2^j}} \psi^{(\alpha)}\left(\frac{t - k\,2^j}{2^j}\right) \tag{2.4}$$

Any signal can thus be expanded using wavelets using a "time-scale" decomposition (singular example on Fig. 2.1 B-2.1 C) in terms of a weighted sum of discrete time translated (k) of successive scaled (2^j) wavelets, up to a predefined scale 2^J :

$$s(t) = s_r(t) + \sum_{j=1}^{J} \sum_{k=1}^{n_j} w_{j,k}\ \ \psi_{j,k}^{(\alpha)}(t) \tag{2.5}$$

where $n_j = 2^{-j}N$ is the number of wavelet coefficients that describe the signal at scale 2^j. Each coefficient w_{jk} is obtained by correlating the signal with a scaled and shifted wavelet $\psi_{j,k}^{(\alpha)}$ and Fig. 2.1 C (time-scale decomposition) gives a visual representation of the coefficients. For completeness, we highlight two points related to this wavelet expansion.

- *Localization of coefficients.* A wavelet coefficient at scale $\approx 2^j$ captures signal content around frequency $f_j = 2^{-j} f_0$ localized around temporal window of size 2^j, and centered at $t = k\,2^j$. In other words, coefficients result from a localized band-pass filter in time and frequency. It is worth noting that, despite the temporal correlations present in the original signal, the wavelet coefficients of this discrete expansion are largely decorrelated, enabling localized processing.

- *Low-frequency residue.* The expansion also includes a residue ($s_r(t)$ in Eq. 2.5) corresponding to stable slow activity not described by the wavelets. This large-scale approximation of the original signal results from a low-pass filter that complements the bandpass filters of the wavelets-based correlations. In practice, because signals are finite in duration, this residue also compensates for edge effects limiting reliable estimation of the largest scales (i.e., very low frequencies activity).

Thus, wavelet coefficients provide a time–scale representation of the signal, whereas the residual captures an unavoidable low-frequency approximation in finite-length recordings.

2.3.3 The *RnB* Procedure

To extract a rhythmic time series, *RnB* will proceed in three steps using the analysis of an original time series: (i) estimate β per epoch from the log–log slope of wavelet-power across scales; (ii) attenuate the $1/f$ contribution on a sparse selection of the coefficients; (iii) synthesize the rhythmic time series from those coefficients in a suitable wavelet basis.

1. Estimation of the scaling exponent β in the wavelet domain

Rather than estimating β in the Fourier domain, we use the scaling of wavelet coefficient power given by (Abry et al., 2019). Let $D_j = \log\left(\frac{1}{n_j}\sum_k {w_{j,k}}^2\right)$ be the average log-power at scale *j*. A standard weighted least-squares regression of D computed over all logarithmic scales will reveal the expected linear trend of the scale-free process. Fig. 2.1 D illustrates this log-log linear regression on the wavelet coefficients from 300 epochs of NREM3 sleep recordings. Notice the linear slope indicating the presence of a scale-free process in the wavelet coefficients. This process contributes to the power of each coefficient in the time-scale representation.

$$\beta^* = \frac{\sum_{j_1}^{j_2} n_j \ \sum_{j_1}^{j_2} j\, n_j\, D_j - \sum_{j_1}^{j_2} j\, n_j \ \sum_{j_1}^{j_2} n_j \ D_j}{\sum_{j_1}^{j_2} n_j \ \sum_{j_1}^{j_2} n_j\, j^2 - \left(\sum_{j_1}^{j_2} j\, n_j\right)^2} \tag{2.6}$$

2. Attenuation of $1/f$ activity and denoising of wavelet coefficients

In analogy with the IRASA approach introduced in Eq. 2.3, *RnB* adjusts wavelet coefficients in the "time-scale" domain to account for ubiquitous, scale-free activity. To this end, we will use the *fractional spline wavelets* introduced by Blu & Unser (2000), whose regularity parameter α controls the smoothness of the basis and sets the expected scale-law of the coefficients (β^*). Unlike classical integer-order wavelets, this basis allows fractional orders, providing a natural way to decorrelate the β^* exponent from the oscillatory content and thereby attenuate the $1/f^{\beta^*}$ background.

For a signal with aperiodic exponent β^* and using a wavelet analysis with $\alpha = a_0 + \frac{\beta^*}{2}$, the decay of the wavelet coefficients follows $w_{j,k} \sim 2^{j(a_0+\frac{\beta^*}{2})}$, and combines the intrinsic regularity of the wavelet basis (a_0) and the scaling exponent (β^*). This scale-free process is visible in the coefficients from the time-scale expansion of the initial signal (Fig. 2.1C), in which a power law is clear (Fig. 2.1D).

To remove the arrhythmic contribution, *RnB* will rescale the coefficients as $w^*_{j,k} \sim 2^{-j\frac{\beta^*}{2}}\, w_{j,k}$.This correction flattens the scale-free trend, leaving residual coefficients that primarily reflect rhythmic contribution as illustrated in Fig. 2.1 E.

In addition to the previous $1/f^{\beta^*}$correction, the processing of the wavelet coefficients also involves a standard denoising, a "soft shrinkage" $\mathcal{S}(w_{j,k})$ that will contribute to the sparsity of the wavelet representation (Donoho & Johnstone, 1994).

$$\mathcal{S}(w) = w\ max\left(1 - {\lambda}/{|w|}, 0\right) \text{ with } \lambda = \sigma\sqrt{2\ln N} \tag{2.7}$$

and the noise σ is estimated from the finest scale wavelet coefficients, $\sigma = median(|w_1|)/0.6745$. The "rhythmic" wavelet coefficients are therefore given by the following expression:

$$w^*_{j,k} = 2^{-j\frac{\beta^*}{2}} \mathcal{S}(w_{jk}) \tag{2.8}$$

3. Synthesis of the rhythmic time series

Since the previous processing removed the β^* scaling from the wavelet coefficients, the rhythmic coefficients $w^*_{j,k}$ define a wavelet expansion using only α_0 :

$$s_R(t) \stackrel{\text{def}}{=} \sum_{j=1}^{J} \sum_{k=1}^{n_j} w^*_{j,k} \psi^{(\alpha_0)}_{j,k}(t) \tag{2.9}$$

The regularity parameter α_0 governs the wavelet smoothness of this synthesis, and indirectly its effective temporal extent: larger α yield smoother wavelets with longer, more oscillatory temporal envelopes and narrower spectral bandwidth, whereas smaller α values produce shorter and more "impulsive" wavelets, with higher temporal but lower spectral resolution, reflecting the fundamental time–frequency trade-off (Abry et al., 2019 ; Blu & Unser, 2000).

We set $\alpha_0 = 4$ as a compromise between temporal and spectral resolution, suitable for NREM sleep rhythms. This value provides a sufficient frequency resolution to represent narrowband transients such as spindles, while maintaining temporal sharpness for broader slow waves.

The resulting time-scale representation and rhythmic time series (Fig. 2.1 E, G) shows a marked attenuation of the arrhythmic component and highlight scale-specific rhythmic activity across multiple NREM3 epochs (Fig. 2.1 F). Note that the rhythmic time series $s_R(t)$ omit the residual term $s_r(t)$ from Eq. 2.5, which capture ultra-slow non-localized fluctuations, and whose removal improve robustness to very low-frequency artifacts and slow drifts.

2.3.4 Spectroscopy of NREM sleep recordings

Spectroscopy refers to the systematic analysis of the intrinsic oscillatory content of a signal or observation, providing a basis for unambiguous interpretation. In *RnB*, the rhythmic signal is obtained from the synthesis of the denoised wavelet coefficients, in which the scale-free component is attenuated. However, because wavelet power is organized by dyadic scales (i.e. discrete frequency intervals), it lacks a fine quasi-continuous frequency resolution when considered as a power spectrum (as illustrated on Fig. 2.1 F). However, the Fourier power spectra from the rhythmic signals will provide this finer description when averaged across epochs (akin to the IRASA method described in Eq. 2.3; (Wen & Liu, 2016)), yielding a reliable representation of dominant oscillatory activity.

In context of this paper, we will define the *NREM sleep spectroscopy* as the joint analysis of (i) the distribution of scale-free exponents (β^*) across epochs, capturing the variations of the arrhythmic background (Fig. 2.2 A) and (ii) the Fourier spectrum of the rhythmic component from $s_R(t)$, describing its oscillatory activity (Fig. 2.2 B). This provides an integrated framework for characterizing the organization of oscillations within their arrhythmic context across NREM sleep epochs.

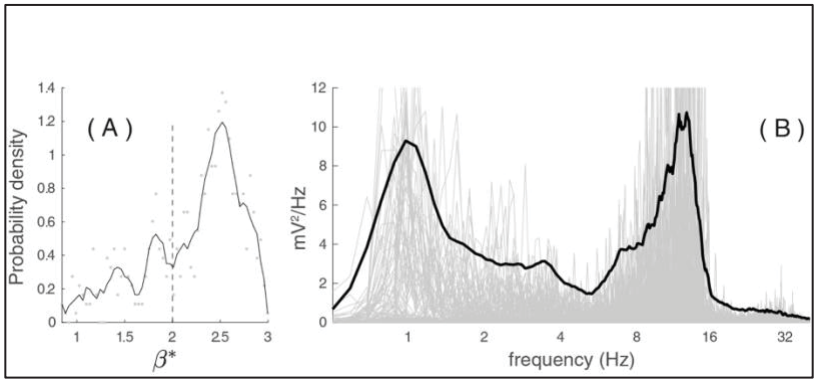

Figure 2.2 The 'NREM sleep spectroscopy'

2.3.5 The RnB algorithm – code accessibility

In the following sections, we apply the RnB algorithm to simulations and intracranial NREM sleep recordings, demonstrating its validity through simulations and application using NREM sleep analysis. A guide how to use this algorithm on user-provided data can be found in a publicly available GitHub. This algorithm is available as a MATLAB package licensed under an Apache 2.0 license. The module supports MATLAB 2021a or later, with dependencies upon the 'Signal Processing' toolbox. The package is openly developed and maintained. The project's repository includes the codebase, a demo which allows for illustration use of the algorithm on publicly available and user-provided data and the documentation materials. This pipeline allows user-provided time series to extract a rhythmic time series and perform basic spectroscopy. Rhythmic time series are extracted as a matrix that can be used by the user to perform time-resolved analyses in other pipelines.

Two parameters need to be set to use the algorithm on user-provided data (see the *wRnBMain* script).

- The j_1 and j_2 parameters specify the range in which the scaling exponent β^* is estimated (Eq.2.6). This should be done across scales ranging from j_1 (high frequencies) to j_2 (low frequencies). The range of scales from j_1 to j_2 should cover a range in which the scale-free process and rhythms of interest are both present (see Fig. 2.1 F for a correspondence between scales and frequencies). Importantly, there is a compromise between the scales to be used and the duration of the epochs in which the statistics are computed. The finest scales (high frequencies) should not include noisy activity, whereas the largest scales (low frequencies) are limited by epoch duration and edge effects. This can be manually tweaked in the RnB algorithm described in the following section.

- The parameter J refers to the largest scale (lower frequency) upon which the wavelet analysis/synthesis operations are performed to obtain the rhythmic signal.

These parameters can be changed according to the input data properties and the documentation on GitHub allow the user to understand the impact of such changes. As default parameters used in this work, the scale ran from 1 to 9 to determine the arrhythmic β^*s and the parameter J was set to 8.

2.3.6 Simulation analyses of RnB

Simulations were conducted to assess *RnB* performance in characterizing background and rhythms. A set of eight second epochs were constructed, combining various scale-free backgrounds with transient four second oscillations. Considering fractional Brownian motion (fBm) signals, the scale-free backgrounds were obtained by filtering white-noise time series to obtain a power law $1/f^{\beta}$ of the spectral power, while keeping the Fourier phase random. To introduce variability in the background, each trial used a β scaling exponent randomly sampled around a predefined mean value, with a standard deviation of 0.1.

Four-second alpha oscillations were added to these scale-free backgrounds using a classical phenomenological neural mass model (Jansen & Rit, 1995 ; Pinotsis, Moran, & Friston, 2012). This model simulates the dynamics of coupled inhibitory and excitatory neuronal populations interacting with a pyramidal cell. Examples of the temporal and spectral responses of this pure "rhythmic" model are presented in Fig. 2.3. These neural mass responses were superimposed onto pure scale-free backgrounds to construct realistic time series (see Fig. 2.4 A for an example).

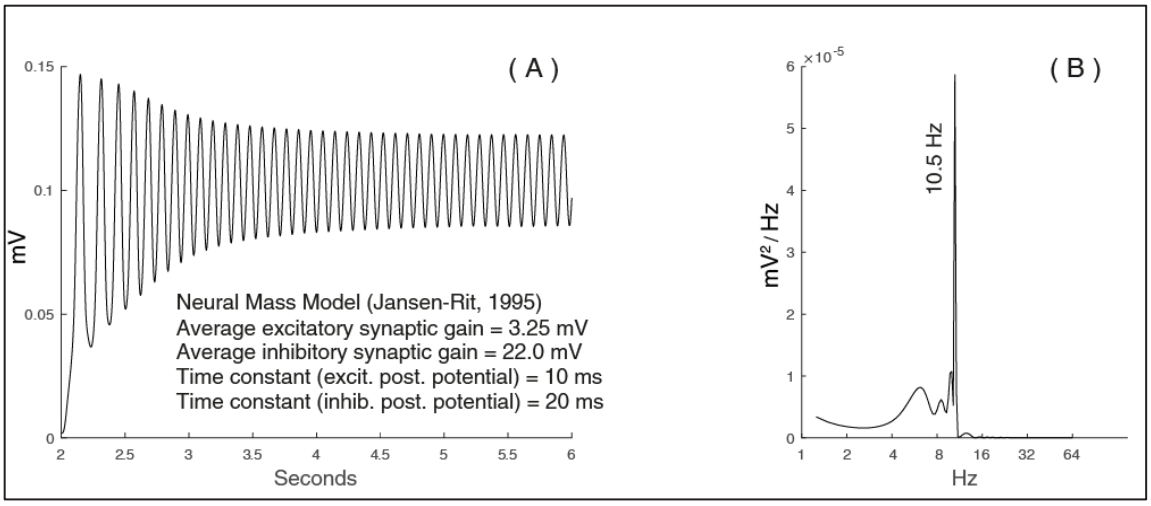

Figure 2.3 Methods: neural mass simulations

Two sets of simulations were conducted to assess *RnB*'s accuracy in estimating the maximal rhythmic amplitude of alpha and delta rhythms, as well as the scaling exponents.

1. The first set of simulations tested the robustness of *RnB* estimation for an alpha oscillation (10.5 Hz) simulated at 15 arbitrary amplitude levels within three arrhythmic background conditions (β = 1.7, 2.1 and 2.5).

2. A second set of simulations assessed the ability of *RnB* to perform accurate estimations in the context of two concurrent oscillations (delta at 3 Hz and alpha at 13 Hz). The delta oscillation varied across 15 incremental arbitrary amplitude levels, and the alpha amplitude remained constant.

For each condition (oscillation amplitude × background β), we first generated 300 pure scale-free epochs with β sampled around the target value (SD = 0.1). Oscillatory activity was then superimposed on 200 randomly chosen epochs per condition, leaving the 100 remaining ones as arrhythmic controls. To mimic a realistic scenario where rhythms may or may not be present, 60 epochs per condition were randomly selected among the total 300 for statistical analyses. *RnB* estimates of maximal rhythmic amplitude and scaling exponents were then extracted from these analyzed epochs.

2.3.7 Intracranial NREM sleep analyses using RnB

From NREM sleep recordings, we investigated whether rhythmic time series exhibit cardinal NREM sleep rhythms, notably their spectral signature and inter-frequency (delta-sigma) coupling. To do so, we first performed spectral analyses of the NREM sleep rhythmic time series produced by *RnB*. Second, we detected sleep slow waves in the rhythmic time series and characterized how these events locally group and synchronize other rhythms in the theta and sigma frequency bands. Finally, we assessed whether delta-sigma phase-amplitude coupling during NREM sleep differed between rhythmic and original time series.

2.3.7.1 Intracranial recordings

The intracranial recordings used in this work are extracted from a publicly available repository of iEEG recordings in patients with epilepsy. From this multicentric database providing physiological activity in non-lesional tissues of the sleeping brain, we used the recordings of 16 patients. Analyses were performed on NREM2 and NREM3 sleep recordings, including all electrodes (sampling rate: 200 Hz) localized in the precuneus and the anterior cingulate, two key hubs of cortical synchronization for slow waves and sleep spindles (Murphy et al., 2009 ; Zerouali et al., 2014). All recordings were segmented into 20-second epochs. The duration of recordings in each region and sleep stage is described in Table 2.1.

Table 2.1 Dataset for the intracranial sleep recordings. Total number of 20s epochs and total duration of each sleep stage are shown

Region	Sleep stage	# epochs	Total duration (min)
Precuneus	NREM2	967	322.33
	NREM3	951	317
Ant. Cingulate	NREM2	821	273.66
	NREM3	809	269.66

2.3.7.2 Spectroscopy of NREM sleep recordings

Each 20 second NREM sleep epoch was processed with the *RnB* algorithm to estimate the scaling exponent and extract a rhythmic time series. From *RnB* outputs, we estimated the distribution of scaling exponents and the average power spectral density separately in NREM2 and NREM3 sleep, what will be referred to as 'NREM sleep spectroscopy' (i.e., Fig 2.2). We compared these results to model fits from FOOOF, a standard spectral parameterization method (Donoghue et al., 2020).

For FOOOF analyses, we used the following parameters: an extraction of three peaks in the 0-45 Hz range, with fixed knee aperiodic modes (single slope). Aperiodic knees were initially parametrized in a subset of models but did not yield stable results and were therefore excluded from subsequent analyses.

2.3.7.3 Slow waves detection in the NREM sleep rhythmic signals

We adopted a proof-of-concept approach to detect sleep slow waves (SSWs) in the rhythmic time series from NREM3 sleep, to assess how they impacted the delta-sigma coupling during NREM sleep.

Rhythmic SSWs (rSSW) were identified in the rhythmic time series using a custom-made detector using region-adaptative frequency-filtering. This filtering served to use the locally expressed oscillatory content in each region, in line with the recent approaches (Donoghue et al., 2022). This detector operates in three steps:

1. **Canonical slow-wave candidates and polarity in intracranial-EEG**

We first used a standard intracranial slow wave detector on the rhythmic times series, as defined by von Ellenrieder et al. (2016). Briefly, candidates slow-wave half-waves were identified in the rhythmic time series after delta filtering (0.5–4 Hz) by detecting zero-crossings. Only half-waves with a duration falling within physiologically plausible limits

(125–1000 ms) were retained. Because intracranial bipolar polarity varies according to neuronal geometry, and therefore cannot be used to determine the phase of SSWs, we inferred rSSWs phase by comparing gamma-band (30–80 Hz) power between successive half-waves; the half-wave exhibiting lower gamma power was labeled as the rSSWs down-state.

2. Region-adaptive rhythmic filtering.

From the NREM sleep spectroscopy in each region (rhythmic time series), we defined a stage-specific delta band-pass filter centered on the main rhythmic delta peak which stood out locally during NREM3 (see Figure 2.6 for relevant results). For the anterior cingulate, this range was 0.5–2.5 Hz; for the precuneus, it was 1–3 Hz. We then re-applied the same detection criteria as in Step 1 (zero-crossing identification, duration limits, and gamma-based polarity determination) within this region-adaptive band to isolate events with maximal rhythmic content for each region and stage.

3. Conjunction of detected SW

The final rSSW inventory was defined as the conjunction of events detected in both passes. This procedure acted as a region-adaptative filter to lower the number of rSSWs retained from standard step-1, in accordance with the frequencies observed in the NREM sleep spectroscopy of each region.

2.3.7.4 Original-signal SSW inventory

We also produced a second SSW inventory from the original NREM sleep recordings, using the standard intracranial detection criteria described in step 1 above (von Ellenrieder et al., 2016). This set of SSWs detected in the original intracranial signal (without *RnB* processing) served to compare NREM sleep findings between the rhythmic time series provided by *RnB* and the original signal.

2.3.7.5 Windowing and classification of sleep slow waves

For all analyses (spectroscopy, time–frequency, and PAC), we extracted 4-s windows centered on the maximal hyperpolarization peak of each SSW or rSSW.

As in Bouchard et al. (2021), we characterized the transition frequency of each SSWs and rSSWs by measuring the time delay (τ) between the down phase (hyperpolarization) and up phase (depolarization) maxima. The inverse of this delay was used to define, for each SSW, a transition-frequency $f_{tr} = \frac{1}{2\tau}$. Then, we applied an unsupervised Gaussian mixture model (expectation–maximization algorithm) to the transition-frequency distribution in each region, classifying events into latent "switcher" classes: slow switchers (SlowS) with lower transition frequency, and fast switchers (FastS) with faster transition frequency. Events in the rhythmic signal are referred to as rhythmic slow switchers (rSlowS) and rhythmic fast switchers (rFastS).

2.3.7.6 Spectroscopy analysis of rSSWs

In the first set of analyses, the spectroscopy of rSSWs was compared to an equivalent number of baseline periods, using four-second NREM3 sleep time windows without rSSWs. Second, we directly compared the spectroscopy of rSlowS to rFastS, as SSWs with a slower transition frequency are known to better synchronize NREM sigma (≈13 Hz) rhythms (Chylinski et al., 2022).

2.3.7.7 Time-frequency analysis of rSSWs

To examine the timing of other NREM rhythmic activity around rSSWs, we used the rhythmic timeseries to perform time-frequency analyses around two distinct characteristic markers of rSSWs : 1) For standard rSSWs analyses, the peak of hyperpolarization was used as the central landmark consistent with previous studies (Cox, Driel, Boer, & Talamini, 2014) ; and 2) When specifically comparing rSlowS and rFastS, the window was centered on the zero-crossing point between hyperpolarization and depolarization, representing the midpoint of the transition

phase for both types. This alignment ensures equivalence between the two types of switchers, as depolarization occurs more rapidly in fast switchers.

To assess the impact on rSSWs on other rhythms, we computed two types of scalograms, following Tallon-Baudry & Bertrand (1999): 1) the induced power scalogram and 2) the phase-locked power scalogram. Both provide amplitude estimates in a time-frequency plane but differ in their computation. Induced power is obtained by averaging the amplitude of wavelet coefficients computed on a trial-by-trial basis. In contrast, phase-locked power is computed by first averaging the co-registered signal across rSSWs and then extracting the amplitude of the resulting wavelet coefficients (Tallon-Baudry & Bertrand, 1999). Phase-locked power thus isolates activity that is systematically aligned in phase across events, whereas induced power reflects the total event-related power regardless of phase consistency.

For all rSSWs analyses, we calculated the time-frequency wavelet transform within a one-second window around each central landmark (indicated as t=0 in Fig. 2.9). The scalograms were calculated using the continuous wavelet transform with the Morse analytic wavelet (default parameters: $\beta = 20$ and $\gamma = 3$). For visualization only, each scalogram is renormalized using an analytic variant of the Taeger-Kaiser power normalization and each display is individually rescaled between 0 and 1.

2.3.7.8 Phase amplitude Coupling analysis of rSSWs

To investigate how the rhythmic and original timeseries differ in their sensitivity to the phase-amplitude coupling (PAC) of delta and sigma rhythms during NREM sleep, we computed delta-sigma PAC from 4-s epochs centered on SSW epochs in the original timeseries and around rSSWs epochs in the rhythmic timeseries (rhythmic PAC; rPAC).

For SSWs, we used the phase $\varphi(t)$ of the delta band (0.5 - 4Hz) and the amplitude of the simultaneous sigma activity (10 - 16 Hz) from the Hilbert transform of the original signal. For rPAC, we considered the phase $\varphi(t)$ and the amplitude of the simultaneous sigma activity

from the Hilbert transform of the rhythmic time series preprocessed with RnB. For rPAC, we adapted the sigma frequency band as defined by the RnB spectroscopy in each region (Fig. 2.7; Anterior Cingulate: 8-14 Hz; Precuneus: 11.5-14.5 Hz).

For SSWs or rSSWs, the PAC and rPAC are defined by:

$$PAC = \left|\frac{1}{T}\sum_{t}(A(t) - \langle A\rangle)(\, e^{i\,\varphi(t)} - \langle\, e^{i\,\varphi}\rangle)\right| \tag{2.10}$$

$$= \left|\frac{1}{T}\sum_{t} A(t)\, e^{i\,\varphi(t)} - \frac{1}{T}\sum_{t} A(t)\;\; \frac{1}{T}\sum_{t} e^{i\,\varphi(t)}\right|$$

where T is the epoch duration across which the summation is running, and $\langle A\rangle$ and $\langle e^{i\varphi}\rangle$ are the mean amplitude and mean complex phase term across T. Subtracting these means removes spurious correlations caused by amplitude offsets or non-uniform phase distributions, providing a normalized measure that is robust to differences in overall signal power or phase bias (Cox, Rüber, Staresina, & Fell, 2020). PAC values were further averaged by event types (rSlowS and rFastS) in each region (anterior cingulate and precuneus).

2.3.7.9 Detection of theta bursts associated with rSSWs in the rhythmic timeseries

The impact of 'theta burst' (TBs) on delta-sigma PAC was investigated specifically in the precuneus (Jiang, Gonzalez-Martinez, & Halgren, 2019) because we identified a theta peak in the precuneus spectroscopy (Fig. 2.7). This was done because TBs were previously identified as precursors and potential modulators of sleep spindles (sigma) activity (Jiang et al., 2019). To do so, we adapted an existing NREM TBs detection algorithm for the rhythmic time series. We used the specific theta-band from the NREM sleep spectroscopy of the precuneus (theta mode 7.02 ± 2.4 Hz in NREM3). The detected events needed to reach a peak above ± 3 standard deviations of the average theta power, with start and stop times defined with ± 1 standard deviation. The final TBs inventory kept events with a duration between 0.4 and 1 second. We then extracted 4-sec windows centered around rSSWs co-occurring with TBs (<500ms; rSSWs+TBs events) and around rSSWs that did not (rSSWs-TBs events).

2.3.7.10 Statistics

We used statistical tests to determine the accuracy of *RnB* in our simulation and to evaluate the impact of the SSWs switcher types on rhythmic power and rPAC. Data distribution was inspected with Shapiro–Wilk tests. Parametric tests (two-tailed) were used when normality held; otherwise, non-parametric equivalents were chosen. All statistical analyses were performed using SPSS 26.

Linear regressions were used to assess the relationship between simulation parameters and *RnB* estimates (estimation of maximal rhythmic amplitude and arrhythmic scaling exponents). Simulation parameters (arrhythmic beta, rhythmic amplitude) and their interactions were entered as predictors of RnB outcomes in SPSS Statistics 26 software.

For intracranial data of NREM sleep, bilateral t-tests (with 1000 bootstraps to obtain bias-corrected confidence intervals), or non-parametric Mann-Whitney U, investigated the impact of switcher type (rSlowS vs rFastS) on the NREM sleep spectroscopy (arrhythmic beta and rhythmic power). For rhythmic power, we integrated power in adaptative frequency bands for identified peaks in the NREM sleep spectroscopy of the anterior cingulate and precuneus (delta: 0.5-4 Hz in both regions, sigma: 8-14 Hz in anterior cingulate, 11.5-14.5 Hz in precuneus, theta: 5-9 Hz in precuneus; Figure 6).

Mann-Whitney U-tests were used to test the difference in delta-sigma PAC between the original and rhythmic timeseries separately for both types of switchers in the precuneus and in the anterior cingulate. PAC and rPAC difference between switchers were also investigated separately in each region. Finally, the impact of TB on PAC differences was investigated in the preceding classification (rSSWs+TBs vs rSSWs-TBs) in the precuneus.

2.4 Results

We used realistic simulations to evaluate *RnB* performance in estimating rhythmic (oscillation amplitude) and scaling (β) parameters. As a first illustrative example of *RnB* application, we

considered a simulated alpha (10.5 Hz) oscillation embedded in an arrhythmic background (Fig. 2.4). The initial signal (Fig. 2.4 A) exhibited a clear arrhythmic drift, which was evident in its Fourier spectrum (Fig. 2.4 B). After *RnB* processing, the rhythmic signal shows a clear transient oscillation, and the arrhythmic drift is removed (Fig. 2.4 C). The spectral analysis of the rhythmic signal reveals a clear alpha peak in the rhythmic spectral density (Fig. 2.4 D).

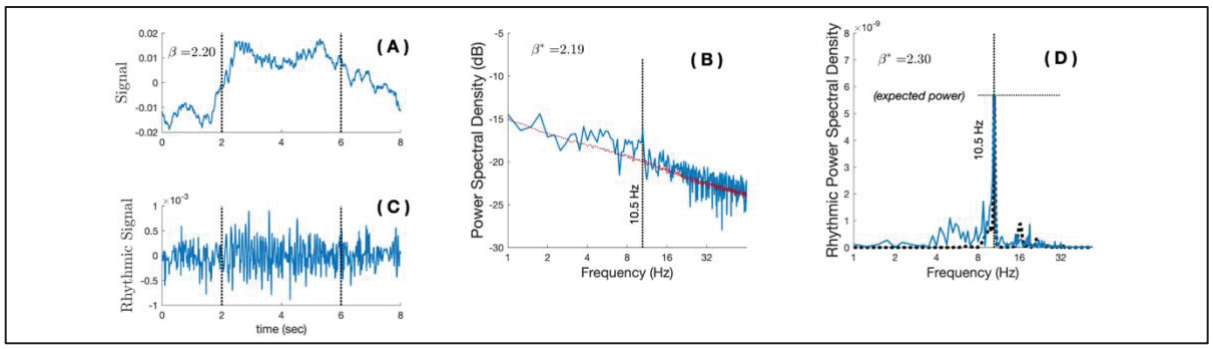

Figure 2.4 Methods: RnB estimations of neural masses simulations

Regression analyses then examined how varying the amplitude of simulated alpha oscillations (15 amplitude levels x 3 arrhythmic background conditions; Fig. 2.5 A-2.5 B) predicted *RnB* alpha amplitude estimates. *RnB* alpha amplitude scaled significantly and positively with the simulated alpha amplitude ($b = 0.99$, $p < 0.0001$), accounting for nearly all variance in *RnB* outputs ($R^2 = 0.98$; Fig. 2.5A). A small Amplitude × Background interaction was observed ($t = 8.58$, $p < 0.0001$, $\Delta R^2 < 0.01$), indicating a weaker relationship in the background condition with higher β values ($\Delta b = -0.05$, $p < 0.0001$). Importantly, the association between simulated and measured alpha amplitude remained strong and significant in all three background conditions (slopes ranging from $b = 0.94$ to 0.99, all $p < 0.0001$).

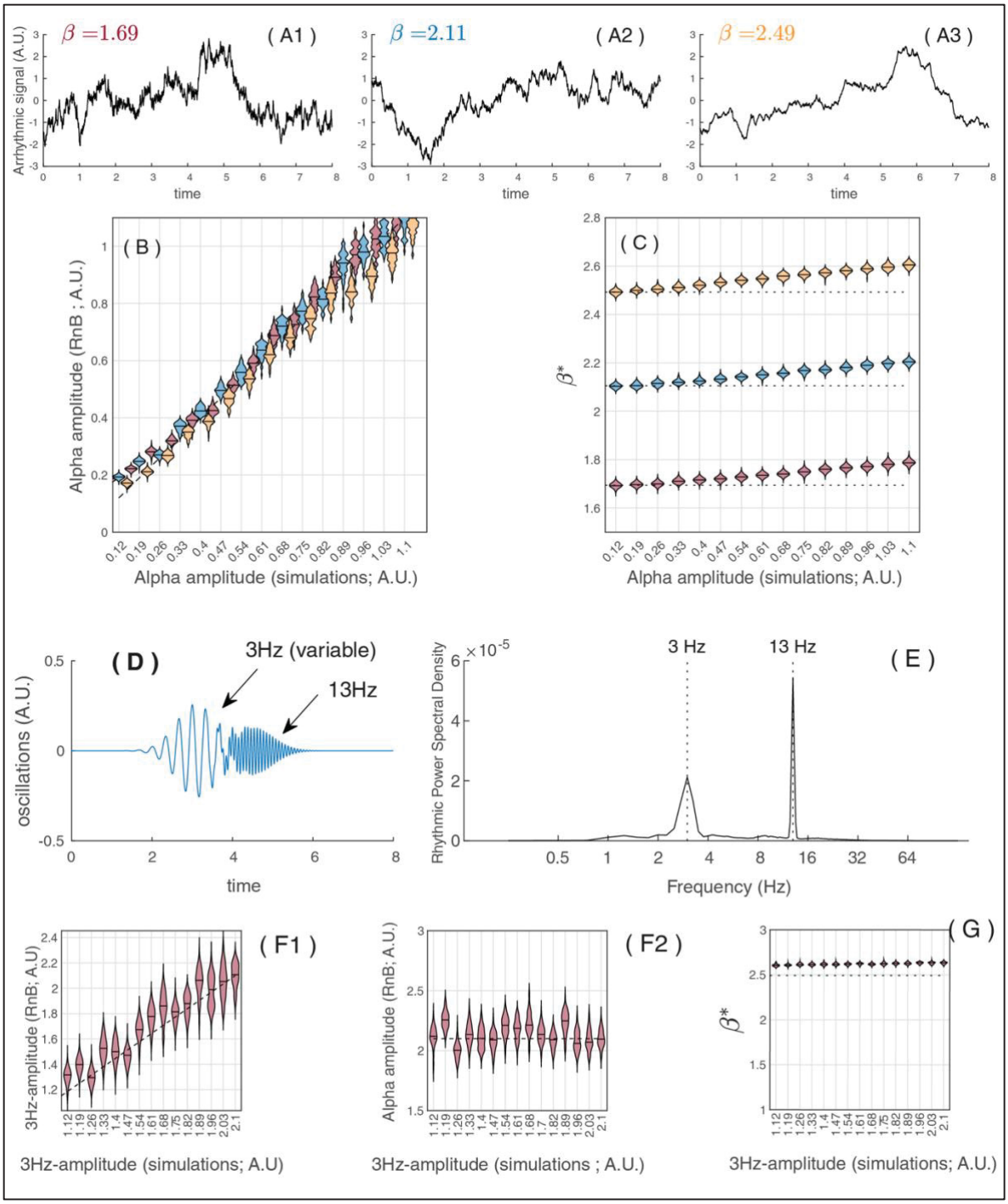

Figure 2.5 Simulation results: RnB estimations of rhythms and background

We next tested whether varying the amplitude of simulated alpha oscillations predicted *RnB* scale-free background (β) estimates across the same 15 amplitude levels x 3 background conditions (Fig. 2.5 C). In contrast to the strong effects on alpha amplitude estimates, *RnB* β estimates scaled only modestly with simulated alpha amplitude ($b = 0.10$, $t = 91.1$, $p < 0.001$), which accounted for less than 1% of the variance in β estimates ($R^2 < 0.01$; Fig. 2.5C). A small Amplitude × Background interaction was again observed ($t = 9.47$, $p < 0.001$, $\Delta R^2 < 0.01$), indicating a stronger positive association in the high-β background condition ($\Delta b = 0.01$, $p < 0.001$). Across all models, background condition remained by far the dominant predictor of *RnB* β estimates ($t = 663.3$, $p < 0.0001$, $R^2 = 0.99$).

Finally, we evaluated *RnB* estimates in simulations with two concurrent oscillations (delta at 3 Hz, and alpha at 13 Hz; Fig. 2.5 D–G). Simulated delta amplitude varied across 15 incremental levels, while alpha amplitude remained constant. *RnB* estimated delta amplitude scaled strongly and positively with simulated delta amplitudes ($b=0.87$, $p<0.0001$, $R^2=0.85$; Fig. 2.5 F1). In contrast, *RnB* estimated alpha amplitude was unaffected by simulated delta amplitude ($b=-0.01$, $p=0.27$; Fig. 2.5 F2). By comparison, β estimates increased significantly with higher simulated delta amplitude, explaining ~31% of the variance of β estimates ($b=0.03$, $p<0.001$, $R^2=0.31$; Fig. 2.5G).

Overall, *RnB* provided reliable estimates of both rhythmic amplitudes and scaling exponents across single and concurrent oscillations (alpha and delta). Two minor caveats should be noted: (i), *RnB* scaling exponents (β) estimates are slightly overestimated in the presence of high amplitude oscillation (especially delta); and (ii), rhythmic amplitude estimates (alpha) are slightly attenuated in high-β arrhythmic conditions. Together, these patterns indicate that while rhythmic and arrhythmic components are disentangled, minimal residual cross-influence persist.

2.4.1 The spectroscopy of sleep recordings

We now demonstrate the potential of *RnB* to characterize NREM sleep rhythms using intracranial recordings of NREM sleep. Our analyses focused on the anterior cingulate and the precuneus, two key regions involved in NREM delta (slow waves) and sigma (sleep spindles) rhythms (Murphy et al., 2009 ; Zerouali et al., 2014).

For illustrative purposes, we first show how the NREM sleep power spectrum can be parameterized using FOOOF (Donoghue et al., 2020). As expected, results from FOOOF highlight that intracranial recordings of NREM2 and NREM3 sleep spectrum are characterized by different scaling exponents, with steeper average arrhythmic slope in NREM3 compared to NREM2 in both anterior cingulate and precuneus (β shown on Fig. 2.6 B1 and B2). FOOOF also reveals sigma peaks in the average NREM spectrum in both stages and regions, with an additional theta peak in the precuneus during NREM2 and NREM3 sleep (Fig. 2.6 B1 and B2).

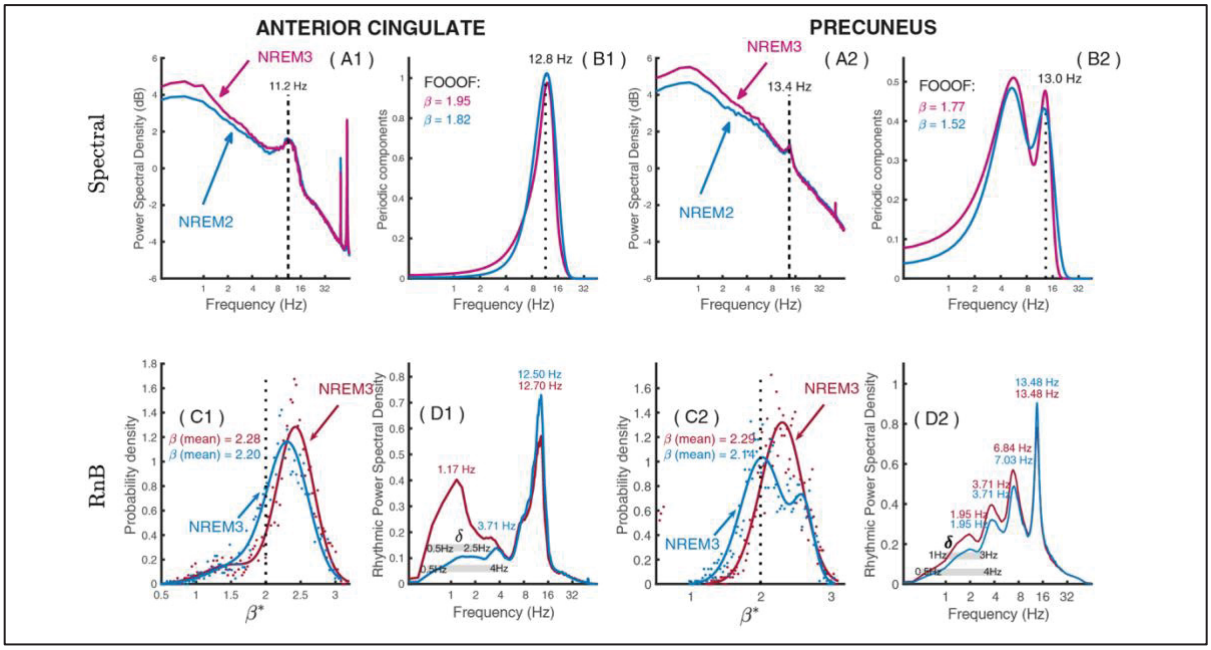

Figure 2.6 Results: RnB application to NREM sleep recordings

Next, we assessed whether the rhythmic time series extracted by *RnB* provided a reliable spectral representation of NREM sleep. Spectroscopy analyses were performed on rhythmic

time series from NREM2 and NREM3 sleep, considering power spectral density and the distribution of scaling exponents. Like FOOOF, the distributions of scaling exponents β assessed by *RnB* showed higher scaling exponents in NREM3 as compared to NREM2 sleep, for both anterior cingulate and precuneus (β distributions shown respectively on Fig. 2.6 C1 and C2). Furthermore, higher rhythmic delta power was observed in NREM3 compared to NREM2 sleep in the anterior cingulate and precuneus, although the specific frequency bands varied between the two regions (Fig. 2.6 D1 and D2). In the anterior cingulate, a single low-frequency delta peak (1.17 Hz) predominated in NREM3 as compared to NREM2 sleep, whereas two delta peaks (1.95 and 3.71 Hz) were found in the precuneus during NREM3 and NREM2 sleep. A rhythmic theta peak (≈ 7 Hz) was also found specifically in the precuneus during NREM2 and NREM3 sleep. Additionally, rhythmic sigma peaks were found in both regions, with slightly faster frequencies in the anterior cingulate (12.5 Hz) as compared to the precuneus (13.5 Hz), and lower maximal power in NREM3 compared to NREM2. The spectroscopy of NREM recordings is thus concordant with expected standard NREM delta and sigma rhythms, in addition to theta rhythms in the precuneus.

2.4.2 Rhythmic sleep slow waves module rhythmic and arrhythmic activity

Given that rhythmic time series showed higher delta activity during NREM3 compared to lighter (NREM2) sleep in both recorded regions, we detected sleep slow waves (SSWs) in the rhythmic time series from NREM3 sleep using spectroscopy-adapted frequency criteria (see methods), which we named “rhythmic sleep slow waves” (rSSWs). We wanted to assess how they modulate other rhythms during NREM3 sleep using time-frequency analyses (time resolved level) and spectroscopy (spectral level).

Detection rates of SSWs and rSSWs were lower in the rhythmic time series than in the original signal during NREM3 sleep (≈5 rSSW/min vs. ≈14 SSW/min), which is expected since arrhythmic fluctuations inflate SSW counts in raw data. rSSWs average waveform retained the expected biphasic shape of SSWs, with fast-frequency suppression during the downstate (Fig. 2.7 A1 and A2). Interestingly, time-frequency analyses of the rSSW in NREM3 indicate that

they were associated with sigma activity in their depolarization period, predominantly in the anterior cingulate (Fig. 2.7 B1 and B2).

The spectroscopy of rSSWs was compared to baseline NREM3 sleep epochs (without sleep slow waves). The probability density distributions showed lower scaling exponents for epochs with rSSWs than for baseline epochs, particularly in the anterior cingulate (Fig. 2.7 C1 and C2). Rhythmic power density showed higher delta and lower sigma rhythmic power for epochs with rSSWs compared to epochs without rSSWs in both regions, although the anterior cingulate showed stronger stage-related difference in rhythmic delta (Fig. 2.7 D1 and D2). Rhythmic sigma peak was wider in the anterior cingulate as compared to the precuneus. The theta peak previously observed in the precuneus also showed lower power during rSSWs as compared to the baseline, suggesting that theta activity in the precuneus may not be specifically linked with rSSWs.

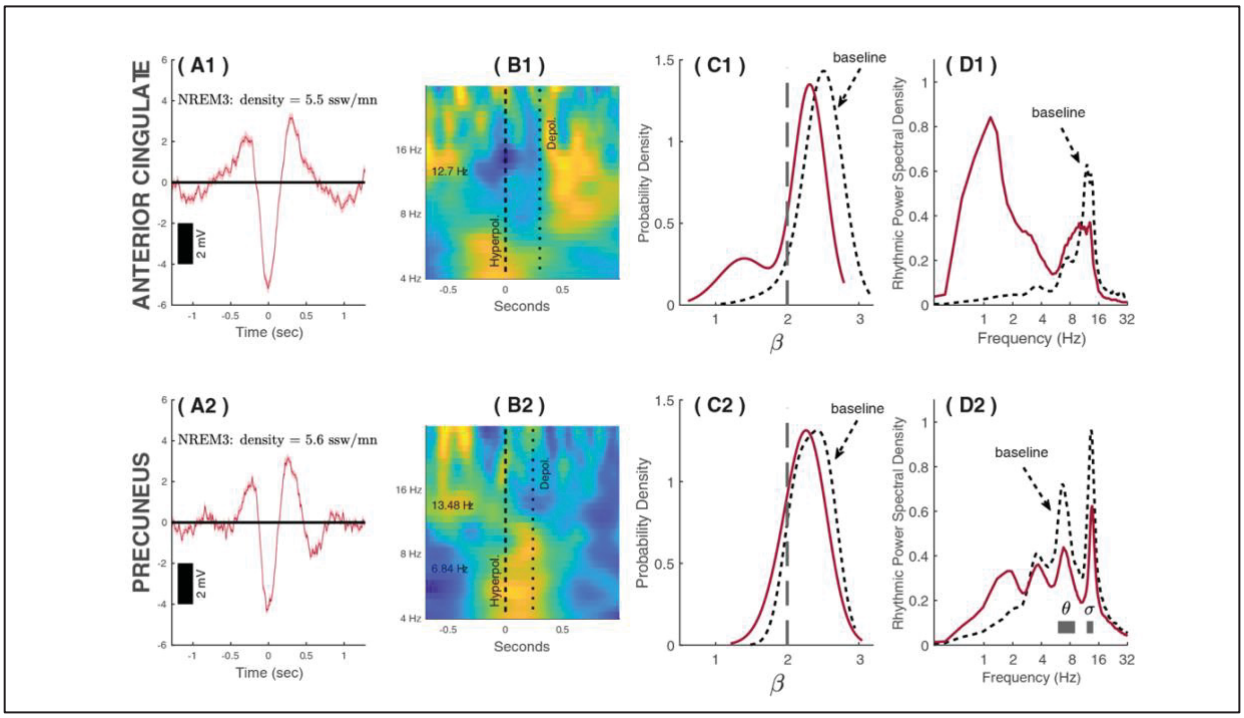

Figure 2.7 Detection of rhythmic sleep slow waves from the anterior cingulate and precuneus during NREM3 sleep

2.4.3 The spectroscopy of SSWs differs according to transition frequency

SSWs can be categorized as *slow* or *fast* switchers, depending on the duration of their transition frequency, the inverse of their *transition period* between their hyperpolarization and depolarization phase (Bouchard et al., 2021). Sigma rhythms are preferentially nested in the transition of SSWs with longer transition periods (slow switchers) as compared to fast switchers during NREM sleep (Chylinski et al., 2022). We thus evaluated in the rhythmic time series how slow switchers group sigma activity during NREM3 sleep.

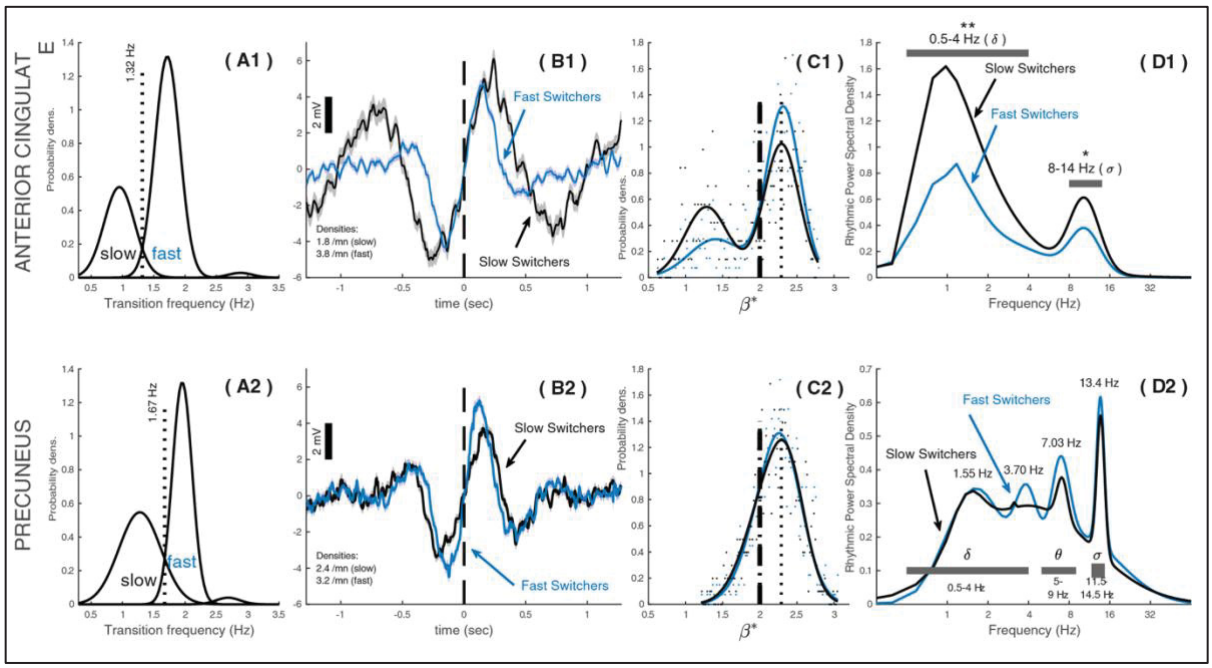

Figure 2.8 The spectroscopy of rhythmic sleep slow waves (rSSWs) in function of their transition frequency during NREM3

We categorized each rSSW detected in the rhythmic time series from NREM3 sleep as a rhythmic slow switcher (rSlowS) or a rhythmic fast switcher (rFastS; Methods). Depending on their transition frequency, we clustered rSSWs between rSlowS and rFastS and found a probability distribution skewed toward rFastS in both regions (Fig. 2.8 A1 and A2). The transition frequency separating rSlowS and rFastS was around 1.32 Hz in the anterior cingulate and 1.67 Hz in the precuneus, indicating a slower transition from hyperpolarization to depolarization in the anterior cingulate (Fig 2.8 B1 and B2 for examples).

The spectroscopy of rSlowS differed from rFastS particularly in the anterior cingulate. In this region, the scaling exponents of rSlowS showed a distribution with lower median values compared to rFastS (Fig. 2.8 C1; standardized Z: -4.5, $p<0.001$ on Mann-Whitney standardized U-test). In the precuneus, no difference between the distributions of scaling exponents was found between Slow and rFastS (Fig 2.7 C2, $p>0.05$). In the anterior cingulate (Fig. 2.8 D1), rSlowS showed significantly higher rhythmic delta power (t-test: $p<0.001$) and higher rhythmic sigma power (t-test $p<0.05$) as compared to rFastS. In the precuneus, rhythmic power spectral density did not significantly differ between rFastS and rSlowS in either considered frequencies (all t-tests $p>0.05$; Fig.2.8 D2).

2.4.4 rSlowS and rFastS regroup differently transient sigma and theta rhythms

To evaluate how other rhythms were regrouped in time by the transition of rSSWs, we examined induced and phase-locked power in time-frequency analyses from the rhythmic timeseries. Induced power reflects the overall amplitude from the average of the wavelet coefficients across all events. In contrast, phase-locked power is the wavelet amplitude computed on the average signal co-registered to a common landmark. Phase-locked power thus provides an indication of how consistently a given event or rhythm occurs in phase at a specific point across co-registered event (here, relative to the transition midpoint of rSSWs), whereas induced power captures increase or decreases in oscillatory energy regardless of the precise phase alignment of the signal. Previous work shows that sigma rhythms tend to occur specifically in phase during the transition from hyperpolarization to depolarization of SSWs, and especially in waves with a slower transition such as rSlowS (Chylinski et al., 2022). We thus hypothesized that rSlowS would exhibit stronger phase-locked sigma power during their transition when compared to rFastS.

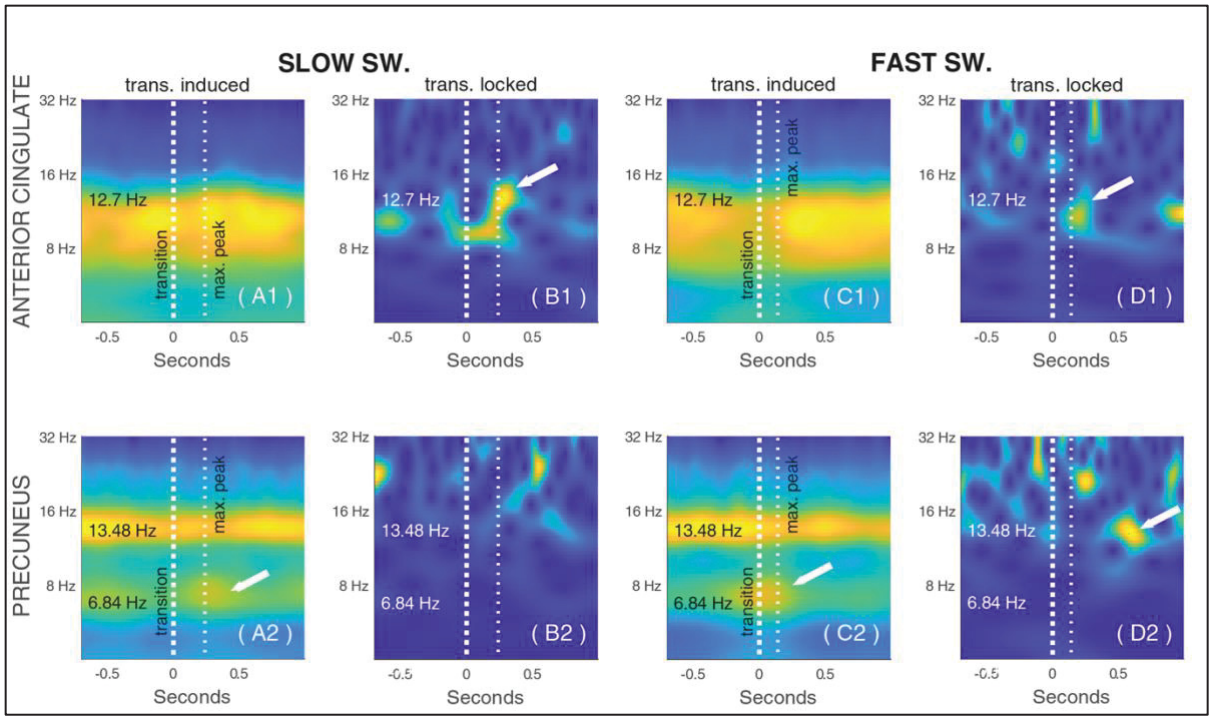

Figure 2.9 Time-frequency analyses of rhythmic slow waves (rSSWs) in function of their transition frequency during NREM3 sleep

Induced sigma power was observed around the transition of both rSlowS and rFastS, in the anterior cingulate (Fig. 2.9 A1-C1) and in the precuneus (Fig. 2.9 A2-C2). As expected, rSlowS in the anterior cingulate further showed noticeable phase-locked sigma power during their transition, reaching maximal power around the depolarizing peak (Fig. 2.9 B1). rFastS in the anterior cingulate also exhibited some phase-locked power around the depolarizing peak (Fig. 2.9 D1), although less pronounced than for rSlowS. In the precuneus, phase-locked sigma power was not strongly modulated around the maximal depolarization peak, for either rSlowS or rFastS. However, some phase-locked sigma emerged approximately 400ms later after the depolarization peak of rFastS in the precuneus (Fig. 2.9 D2).

In the precuneus specifically, induced theta power was observed with the transition of rSlowS and rFastS (Fig 2.9, A2 and C2). However, theta power was not sufficiently synchronized across events to yield a robust phase-locked power signature around the transition of either rSlowS (Fig. 2.9 B2) or rFastS (Fig 2.9 D2).

2.4.5 The rhythmic time series highlights coupled delta and sigma rhythms in NREM3 sleep

We compared delta-sigma coupling from the rhythmic time series versus the original time series. PAC was assessed from SSWs (original iEEG signal) and from rSSWs (rhythmic time series), referred to as rhythmic PAC (rPAC). We hypothesized that rSlowS and rFastS events would show higher PAC than in the original signal, due to minimized arrhythmic interferences in the rhythmic time series.

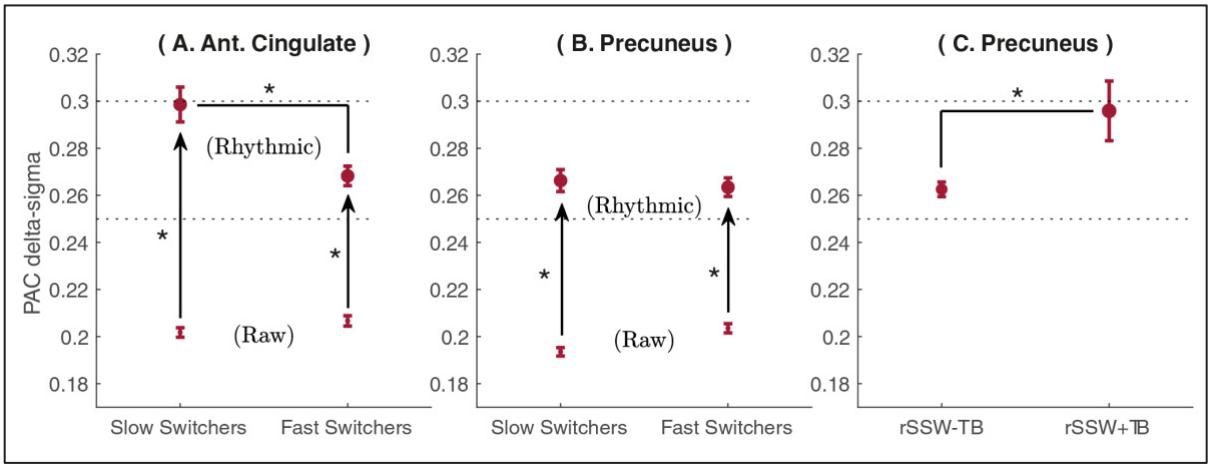

Figure 2.10 Delta-sigma PAC in the original and rhythmic time series

As shown in Fig. 2.10 (A and B), rPAC values were significantly higher than PAC values for both types of switchers in the two brain regions (Mann-Whitney U-tests: $p < 0.001$ for all events). Moreover, rSlowS showed higher rPAC as compared to rFastS in the anterior cingulate during NREM3 (Fig. 2.10A, U=2.82, p=0.005). This difference between switchers was not significant with standard PAC in the anterior cingulate (U= 1.85, p-value=0.06). In the precuneus, no significant differences in rPAC were found between switchers (Fig. 2.10 B, U=0.18, p>0.1).

Since induced theta power was observed around the transition of rSlowS and rFastS in the precuneus, (Fig. 2.9 A2 and C2), we also explored the impact of theta bursts (TBs) events on delta-sigma rPAC during rSSWs in the precuneus. This was prompted by previous literature

suggesting that NREM TBs precede slow-wave-spindle complexes and facilitate delta-sigma PAC (Gonzalez et al., 2018). We identified rSSWs co-occurring with TBs (<500ms; rSSWs+TBs events) and rSSWs that did not (rSSWs-TBs). We hypothesized higher delta-sigma rPAC for rSSWs+TBs events as compared to rSSWs-TB in the precuneus.

As shown in Fig. 2.10 C, delta-sigma rPAC was higher for rSSWs+TBs compared to rSSWs-TBs ($U=2.46$, $p=0.01$). Importantly, rSSWs+TBs events represented around 6% of all rSSWs in NREM3 (116/1815 rSSWs). Although rSSWs+TBs are rare, they constitute a significant modulator of rPAC in NREM3.

In summary, delta–sigma PAC was consistently higher in the rhythmic compared to the original time series. Importantly, *RnB* revealed that delta–sigma PAC is differentially modulated by specific sleep events: rSSWs increased rPAC in the anterior cingulate, whereas TBs enhanced delta–sigma PAC in the precuneus.

2.5 Discussion

The *RnB* algorithm introduces a novel approach to signal processing in electrophysiology, by disentangling rhythmic activity from the arrhythmic background at the time-series level. Spectral methods such as FOOOF and IRASA can separate rhythmic peaks from the scale-free background in the power spectrum (Pani et al., 2022), but they remain limited for time-resolved analyses and signal processing: instantaneous phase, amplitude and PAC estimates remains biased when the background deviates from a simple power law. To address this limitation, we leveraged the wavelet time–scale paradigm to attenuate scale-free activity at the level of wavelet coefficients, producing rhythmic time series with preserved oscillatory components. Simulations and intracranial NREM sleep recordings confirmed that *RnB* reliably recovers transient oscillations across multiple frequency bands. Importantly, rhythmic time series extracted by *RnB* revealed stronger delta–sigma phase-amplitude coupling during NREM3 sleep, underscoring its value for studying cross-frequency interactions.

2.5.1 Dynamic of the scale invariance and NREM Sleep EEG spectroscopy

Growing evidence indicates that the scale-free background is neither constant nor unitary: it changes across sleep stages, and often exhibits frequency-specific "knees", where the spectrum bends away from a single power-law (Brake et al., 2024 ; Gao, 2016 ; Gao et al., 2017). In NREM sleep, these knees overlap with the delta range, "hiding" slow oscillatory peaks (Bódizs et al., 2021 ; Gerster et al., 2022 ; Schneider et al., 2022). The wavelet-based *RnB* framework is particularly robust to this problem for several reasons.

First, wavelet-based estimates provide more reliable characterization of the scale-free regime and of low power than Fourier-based approaches (Abry et al., 2019). This advantage arises from key wavelet properties: (1) their vanishing moments, which cancel slow signal drifts or polynomial trends according to their regularity parameter (a); and (2) their "constant-Q" property, which adapts the time window to each scale and thus maintains a roughly constant number of oscillatory cycles per frequency band. In contrast, Fourier methods use a fixed window size, resulting in poorer resolution and biased low-frequency estimates. Second, *RnB* applies the $1/f^{\beta}$ correction in the time–scale domain, attenuating scale-free activity at each scale and time point. This repeated, scale-specific correction enhances robustness by preserving transient low-frequency oscillations in the reconstructed rhythmic signal. As a result, when the rhythmic signal is reanalyzed spectrally, oscillatory peaks remain clearly identifiable—even when overlapping with a scale-free knee—whereas global spectral parameterization may flatten or distort them (Gerster et al., 2022). Finally, by removing the low-frequency approximation term during synthesis of the rhythmic time series (the "residue" in Equation 2.5), *RnB* eliminates stable departures from the arrhythmic baseline without suppressing non-stationary events. Together, these features enable a genuine spectroscopy of sleep rhythms and allow recovery of transient delta oscillations critical for studying their interactions with spindles.

Simulations confirm that *RnB* preserves delta and sigma amplitudes across a range of 1/f exponents (Fig. 2.5). While *RnB* provides robust estimates of both oscillatory and arrhythmic

activity, our simulations revealed residual cross-component influences. These were modest (in general, $R^2 < 0.01$) but became more substantial in the delta range: strong delta oscillations increased β estimates, explaining up to ~30% variance in *RnB* β estimates. Given the importance of delta activity in sleep research, this coupling must be acknowledged as a potential confound. At the same time, the systematic nature of the effect makes it tractable, suggesting that future refinements (e.g., calibration, iterative separation) could mitigate this bias and enhance the reliability of *RnB* in high-delta contexts.

2.5.2 A case study: detection of rhythmic SW and switchers during NREM sleep

Our intracranial data further showed that the rhythmic time series provided by *RnB* recovered the frontal dominance of rhythmic delta in NREM3, consistent with established slow-wave topography (Steriade, 2006). Using spectroscopy-adapted criteria (Donoghue et al., 2022 ; Muehlroth & Werkle-Bergner, 2020), *RnB* enabled detection of sleep slow waves (SSWs) in the rhythmic time series (rSSWs). Importantly, rSSWs in anterior regions modulated sigma power more strongly than those in the precuneus, corroborating results from EEG studies indicating that frontal waves serve as more potent triggers for spindles (Cox et al., 2014), and supporting the validity of our results.

Notably, we further observed lower scaling exponents during rSSWs in the anterior cingulate compared to NREM sleep epochs without rSSWs, which is aligned with earlier spectral parametrization findings (Lendner et al., 2020). This result also converges with studies linking lower scaling exponents to higher neuronal excitability (Gao et al., 2017), which is also observed during the depolarization phase of sleep slow waves (Steriade, 2006). Interestingly, although simulations indicated inflation of β estimates under higher delta amplitudes, *RnB* remains sensitive to transient reductions in β during NREM3 sleep slow waves and rSlowS, reinforcing the validity of our estimates in relevant physiological ranges.

We also reproduced the fast–slow switchers classification of SSWs in the rhythmic signal (Bouchard et al., 2021). In the anterior cingulate, the transition of slow switchers (rSlowS) was

associated with higher phase-locked sigma power, and rSlowS showed higher delta-sigma rPAC when compared to rFastS. These results support the idea that SSWs with prolonged depolarization periods, such as rSlowS, promote stronger spindle generation (Botella-Soler, Valderrama, Crépon, Navarro, & Quyen, 2012 ; Chylinski et al., 2022 ; Cox, Mylonas, Manoach, & Stickgold, 2018 ; Cox et al., 2020). In the precuneus, rSSW–sigma rPAC depended more on co-occurring theta bursts (TBs), consistent with their proposed role as an "early" down-state that favors subsequent spindle emergence (Gonzalez et al., 2018 ; Jiang et al., 2019). In our data, both event types were relatively rare: most of rSSWs were classified as rFastS (Fig. 2.8), and TBs occurred in approximately 6% of all rSSWs. The scarcity of these specific events likely contributes to the high variability of delta-sigma PAC across studies (Cox, Rüber, Staresina, & Fell, 2019). Collectively, our findings extend MEG observations suggesting that locally synchronized transient sigma rhythms associated with rSlowS and TBs may act as specific drivers of broader spindle synchronization (Zerouali et al., 2014).

2.5.3 Enhancing Phase-Amplitude Coupling measures with RnB

Finally, delta–sigma PAC was higher for SSWs detected in *RnB's* rhythmic signal compared to those detected in the raw signal. This enhancement likely reflects that the rhythmic time series isolate genuine oscillatory activity, thereby increasing the specificity of rSSW detection and PAC estimation, albeit at the cost of sensitivity, resulting in a lower number of detected events in rhythmic compared to original time series. Our trade-off thus favors precision over exhaustivity. Our finding aligns with the notion that scale-free signal fluctuations can introduce spurious SSWs detections and lower PAC estimates, thereby increasing PAC variability (Aru et al., 2015 ; Donoghue et al., 2022). Such variability has repeatedly been noted as a source of small and heterogenous PAC effect sizes in sleep research (Jurkiewicz et al., 2021 ; Mander et al., 2017). By filtering out these arrhythmic confounds, *RnB* enhances the isolation of rhythmic events, improving the robustness of both slow-wave detection and PAC measures. This is particularly valuable for studying rhythm-dependent interactions across hippocampo–thalamo–cortical networks, where arrhythmic activity may differ between regions (Staresina, Niediek, Borger, Surges, & Mormann, 2023).

2.5.4 Future direction

RnB offers a practical shift in EEG signal processing, offering a wavelet-based framework to extract "true" oscillations from complex $1/f^{\beta}$ activity, even when background vary over time or involve multiple "scale-free" regimes. Here, we adapted detection criteria for known NREM sleep rhythms (rSSWs, TBs) to the rhythmic time series, serving as proof of concept rather than an exhaustive event characterization. The next step is to detect and classify rhythmic events directly in the *RnB* signal to develop new empirical detection criteria. For instance, matching pursuit approaches (P. Durka, Dovgialo, Duszyk-Bogorodzka, & Biegański, 2024 ; P. J. Durka & Blinowska, 1995 ; Krstulovic & Gribonval, 2006) or cycle-by-cycle analysis (Cole & Voytek, 2019) implemented within the rhythmic signal might identify subtle SSWs, theta bursts, or sigma bursts that standard detection technique may overlook.

2.6 Conclusion

By leveraging the wavelet-based multiresolution 'time-scale' paradigm, *RnB* disentangles NREM sleep rhythms from their arrhythmic background, enabling extraction of rhythms from scale-free dominated signals. Our findings show that this approach preserves physiologically meaningful oscillatory dynamics to study inter-frequency interactions of neural rhythms. *RnB* allows to shift the spotlight: in the raw signal, scale-free dynamics dominate the stage, whereas *RnB* brings the oscillatory actors to the forefront. In the long run, *RnB* may support the development of a refined detection and classification system of rhythmic sleep events across the lifespan and in clinical populations, where altered scale-free dynamics may obscure oscillatory markers.

CHAPITRE 3

WAVELET-BASED ASSESSEMENT OF THE RHYTHMIC SCALP EEG ACTIVITY DURING NREM SLEEP

Michael Foti[1], Zachay Vachon[2], David Smith[3,4], Rebecca Robillard[3,5], Jean-Marc Lina[1,6,7]

[1]Département de génie électrique, École de technologie supérieure, Montréal, QC, H3C1K3, Canada
[2]Département de physique, Mcgill University, Montréal, QC, Canada
[3]Institut de recherche en santé mental de l'Université d'Ottawa au Royal, Ottawa, ON, Canada
[4]Département de médecine cellulaire et moléculaire, Université d'Ottawa, ON, Canada
[5]École de psychologie, Université d'Ottawa, ON, Canada
[6]Centre d'Études Avancées en Médecine du sommeil, Hop. Sacré-Cœur de Montréal, Montréal, QC, H4J1C5, Canada
[7]Centre de Recherches Mathématique, Université de Montréal, Montréal, QC, H3C1J7, Canada

Article soumis pour publication dans la revue *IEEE Transaction on Biomedial Engineering* le 3 février 2026

3.1 Abstract

Recent evidence suggests that the rhythmic and aperiodic components of the EEG power spectrum may interact. We extend a novel method, initially developed using sleep intracranial recordings to disentangle rhythmic and aperiodic EEG time series, to scalp EEG, which is widely used in clinical settings, to investigate changes during NREM sleep and to assess age effects. The dataset consists of 62 healthy subjects: 30 younger subjects (21 ± 3 years) and 32 older subjects (60 ± 5 years). We developed a wavelet-based approach to disentangle aperiodic and oscillatory components from single epochs. The $1/f$ slope was calculated from the wavelet coefficients, and a time-scale whitening estimator filtered out the aperiodic component from the electrodes C3, F3, and O1. Rhythmic and aperiodic activity were quantified across NREM sleep depth and age groups, and sleep spindle features were extracted from the rhythmic time series using two detection algorithms. Rhythmic spectral features and aperiodic slope varied systematically with NREM sleep depth across both age groups, reliably measuring classical sleep features. The rhythmic time series also preserved sleep spindle activity. The new

approach we propose represents a substantial shift from current methods, which rely solely on the Fourier power spectrum. It can accurately assess the rhythmic activity of scalp EEG recordings. By separating rhythmic and aperiodic EEG activity at the time-series level, this approach offers a new tool for sleep analysis of scalp EEG. Our findings underscore the importance of disentangling rhythmic and aperiodic activity, as it may unveil valuable new biomarkers of pathological sleep states.

3.2 Introduction

The distinction between rhythmic and aperiodic brain activity has recently garnered attention in basic and clinical sleep research. While electroencephalography (EEG) recordings are a complex admixture of these components, the rhythmic oscillations in canonical frequency bands have historically been the principal focus of investigative efforts. Aperiodic activity, characterized by the 1/f decay of the power spectrum, was dismissed as a colored "$1/f$ noise" partly because of its ubiquity across many dynamical systems ranging from seismic activity to stock market fluctuations (He, 2014). In neuroscience, mounting evidence demonstrates that aperiodic or "scale-free" brain activity is physiologically and functionally significant (He, 2014). Physiologically, aperiodic activity manifests a temporal structure that includes nested frequencies and long-range temporal correlations (He, Zempel, Snyder, & Raichle, 2010) . The slope of the spectral $1/f$ decay is also considered as an index of cortical excitation-to-inhibition balance, with a flatter slope indicating relatively greater excitation (Gao et al., 2017). Functionally, aperiodic brain activity in fMRI (functional magnetic resonance imaging) is suppressed with increasing task difficulty and task novelty across experimental paradigms (Churchill et al., 2016). In EEG, the spectral decay also differentiates healthy participants from those with schizophrenia more effectively than oscillations (Peterson, Rosen, Belger, Voytek, & Campbell, 2023).

While it is possible to estimate aperiodic properties (decay and offset of the spectrum) and rhythmicity from the mixed signal, it is valuable to disentangle these components because their commonly extracted metrics can be conflated. For instance, narrowband power fluctuations

can originate from changes to the aperiodic background (Donoghue et al., 2020). We can mitigate these confounding factors with resampling and parameterization techniques, including Irregular Resampling Auto-Spectral Analysis (IRASA) (Wen & Liu, 2016), Fitting Oscillations & One Over F (FOOOF) (Donoghue et al., 2020), and Spectral Parameterization Resolved in Time (SPRiNT) (Wilson, da Silva Castanheira, & Baillet, 2022). To date, some studies have applied these techniques to sleep data. Prior work has shown that the $1/f$ slope steepened from non-rapid eye movement (NREM) 1 to NREM3 sleep and flattened during rapid eye movement (REM) sleep (Bódizs et al., 2021 ; Schneider et al., 2022). An EEG and intracranial electroencephalography (iEEG) study by Lendner et al. (2020) applied several parameterization methods as a control analysis, revealing an increasingly negative (i.e., steeper) $1/f$ slope from wakefulness through NREM3 and REM sleep. While these results provide valuable insights, all those studies are confined to the spectral domain, since the time-domain dynamics of rhythmic and aperiodic components should involve complex non-stationary interactions at the signal level. Sleep analysis is not based solely on spectral properties, it also includes the characterization of graphoelements (slow waves, sleep spindles). Therefore, disentangling the rhythmic and aperiodic activities at the signal level is essential for a comprehensive sleep analysis.

Interestingly, an approach called Periodic–Aperiodic Intrinsic Mode Decomposition (PAIMD) has been introduced to isolate aperiodic activity at the signal level (Farrokhi & Daliri, 2022). In PAIMD a fractional derivative reflecting the slope decay is applied to the entire EEG signal to attenuate aperiodic activity and facilitate the detection of well-defined frequency peaks in the spectrum. Each frequency peak corresponds to an oscillatory component present in the signal. PAIMD then iteratively estimates and subtracts these oscillatory components from the EEG signal. This procedure is repeated until all identified oscillatory components have been removed, leaving a residual that corresponds to an aperiodic signal. More recently, the Rhythms and Background (*RnB*) algorithm developed in Dubé et al. (2024) emphasized the transient rhythmic components. *RnB* is a signal processing approach that extracts rhythmic activity rather than estimate the aperiodic signal. *RnB* uses wavelet-based fractional filters,

which enable local fractional derivatives and thus limit phase distortion when estimating rhythmic signals, thereby preserving their structural characteristics.

RnB has been developed and validated in the context of intracranial EEG (iEEG) sleep recordings (Dubé et al., 2024). Nonetheless, iEEG recordings are invasive and are typically acquired in a specific clinical context, such as refractory epilepsy (Engel, 2014). In light of the growing evidence for the coexistence of rhythmic and aperiodic processes in scalp recordings, it has become timely and appropriate to develop signal processing approaches for scalp EEG aimed at isolating this rhythmic component. Notably, scalp EEG encodes physiologically meaningful information from sleep rhythms, such as sleep spindles. Sleep spindles are transient oscillatory events lasting approximately 0.5 to 3 seconds, with frequencies of 12 to 16 Hz, and occur predominantly during NREM2 sleep. They are hallmark features of sleep, commonly identified using automated detection algorithms, and studied in relation to memory processes and a range of clinical conditions (Fernandez & Luthi, 2019 ; Kumral, Matzerath, Leonhart, & Schönauer, 2023).

The present investigation extends the application of the *RnB* algorithm to scalp EEG sleep recordings. To evaluate the algorithm, we investigate how the aperiodic and rhythmic components of scalp EEG vary throughout sleep episodes, and whether these dynamics are sensitive to spatial topography and age-related differences. We also analyze sleep spindle features on the rhythmic signal using both a standard detection algorithm and the matching pursuit (MP) algorithm (Mallat & Zhang, 1993 ; Martin et al., 2013). Prior work has applied the MP algorithm to standard EEG data, though it is less commonly used due to its computational load (P. J. Durka & Blinowska, 1995 ; Schönwald et al., 2006). MP is a greedy algorithm that iteratively approximates a given signal as a linear combination of atoms selected from a parametrized dictionary of functions. In our case, this dictionary is especially designed to match the spindle characteristics. We hypothesize that, when applied to the rhythmic signal, this data-driven algorithm will identify spindles more accurately because the aperiodic activity is whitened from the signal, thus yielding a more precise spindle inventory. Overall, this study

aims to show that the *RnB* processing can extract valuable rhythmic signals from scalp recordings that encode accurate physiological information.

3.3 Methods and Materials

3.3.1 Dataset

For this study, PSG data were obtained from the SS3 subset database of the Montreal Archive of Sleep Studies (MASS) (O'Reilly, Gosselin, Carrier, & Nielsen, 2014). Ethical guidelines were followed to obtain access to the dataset. The dataset includes 62 healthy subjects, which we divided into two age groups: 30 younger subjects (21 ± 3 years) and 32 older subjects (60 ± 5 years). The recordings were acquired at a sampling rate (f_s) of 256 Hz, and sleep stages were scored based on the AASM criteria (American Academy of Sleep Medicine) (Iber, Ancoli-Israel, Chesson, & Quan, 2007).

3.3.2 Preprocessing

To assess spectral properties, data from electrodes F3, C3, and O1 during NREM2 and NREM3 were subdivided into overlapping 16-s epochs (4096 samples, 12.5% overlap).

For spindle analyses, only a subset of the dataset was used since the MP algorithm is computationally intensive. Analyses were restricted to electrode F3 during NREM2 sleep in 10 subjects. For each subject, spindles were detected only on the first ten 30-s epochs that were extracted. Overlapping epochs were not used for spindle detection to avoid double-counting events near epoch boundaries.

3.3.3 *RnB* processing step

3.3.3.1 Wavelet based estimator of the slope

Each epoch was expanded in its time-scale representation using discrete fractional spline wavelets (Unser & Blu, 1999) ,

$$\psi_{j,k}^{(\alpha_0)}(t) = 2^{-j/2}\psi^{(\alpha_0)}\left(\frac{t-k2^j}{2^j}\right) \tag{3.1}$$

where j and k denote dyadic scales and translation indices, respectively. The fractional wavelet filters are also parametrized according to a regularity parameter $\alpha_0 \in \mathbb{R}$, which allows us to ignore the polynomial trend present in the EEG signal up to order $\lfloor\alpha\rfloor$. For the wavelet-based estimator of the slope, we set the default value to $\alpha_0 = 2$. The signal is decomposed according to a set of dyadic scales $j \in [j_{min}, j_{max}]$ and positions k. This results in a set of wavelet coefficients that describe the time-scale content of a signal, obtained by applying the inner product between the signal and the wavelet, $\langle s, \psi_{j,k}^{(\alpha_0)}\rangle$.

To estimate the slope, which characterizes the aperiodic component, we first compute the logarithm of the mean squared wavelet coefficients at each scale,

$$D_j = log\left(\frac{1}{N_j}\sum_{k=1}^{N_j}|w_{j,k}|^2\right) \tag{3.2}$$

where $w_{j,k}$= $\langle s, \psi_{j,k}^{(\alpha_0)}\rangle$ with $j = j_1 \ldots j_2$ and N_j is the number of coefficients at each scale j. In contrast to the *RnB* slope estimator used in Dubé et al. (2024), which assumes an auto-similar signal (Abry et al., 2019), we relax this assumption to adapt to the complexity of the scalp recordings. Instead of applying a weighted linear regression as proposed in Abry et al. (2019), we use a simple linear regression, as in Bódizs et al. (2021),

$$\beta^* = \frac{n\sum_{j_1}^{j_2} jD_j - \left(\sum_{j_1}^{j_2} j\right)\left(\sum_{j_1}^{j_2} D_j\right)}{n\sum_{j_1}^{j_2} j^2 - \left(\sum_{j_1}^{j_2} j\right)^2} \tag{3.3}$$

where n is the number of scales $(j_2 - j_1 + 1)$. To select the scale range for the linear fit, we first plotted D_j as a function of j for all available scales (log-log scale) (see Fig. 3.1c). This

revealed an attenuation of D_j at higher scales (lower frequencies), which deviates from the expected linear power-law decay. Therefore, to estimate β^*, we selected $j_1 = 2(\sim 64$ Hz) and $j_2 = 8$ ($\sim$1 Hz) for the linear regression to account for this attenuation. The choice of scale j_1 and j_2 depends on the length and sampling frequency of the signal.

3.3.3.2 Wavelet analysis of the signal

We decomposed each epoch into its time-scale content, according to the parameter ($\alpha_0 + \beta^*/2$),

$$w_{j,k} = \langle s, \psi_{j,k}^{\left(\alpha_0 + \frac{\beta^*}{2}\right)} \rangle \tag{3.4}$$

Essentially, the filters are tuned using the slope computed from step 1). This results in wavelet coefficients containing information regarding the regularity and aperiodic component of the decomposed signal (See Fig 3.1d).

3.3.3.3 Wavelet coefficient processing

Blu and Unser have shown (Blu & Unser, 2003), that fractional wavelet coefficients have the following expression,

$$w_{j,k} = 2^{j\left(\alpha_0 + \frac{\beta^*}{2} + \frac{3}{2}\right)} \partial^{\alpha_0 + 1} \partial^{\frac{\beta^*}{2}} s\left(k2^j\right) \tag{3.5}$$

The right-hand side of this equation can be interpreted as the wavelet coefficient of the local fractional derivative $\partial^{\frac{\beta^*}{2}} s\left(k2^j\right)$, in the wavelet basis $\{\psi_{j,k}^{(\alpha_0)}\}$, provided that the factor $2^{j\frac{\beta^*}{2}}$ is factored out. It is worth noting that this filtering of aperiodic activity $2^{-j\frac{\beta^*}{2}}$ parallels a spectral Fourier whitening process of $f^{\frac{\beta^*}{2}}$ but in a time-resolved manner. The filtering process is performed on the wavelet coefficients after applying a soft shrinkage operator, which reduces the coefficients with the lowest energy (Donoho & Johnstone, 1994),

$$\mathcal{S}\left(w_{j,k}\right) = sign\ (w)\ \max(|w| - \lambda, 0) \tag{3.6}$$

where $\lambda = \sigma\sqrt{2 \ln N}$ and the σ is estimated from the finest scale wavelet coefficients, $\sigma = \frac{MAD(|w_1|)}{06745}$. (See Fig 3.1e).

3.3.3.4 Synthesis of the rhytmic signal

The rhythmic signal $s_r(t)$ is obtained through wavelet synthesis, utilizing filters parameterized exclusively by α, as the aperiodic component has been eliminated (See Fig 3.1f). The process to construct $s_r(t)$ is described according to the following equation,

$$s_r(t) = \kappa\left(\alpha_0, \alpha_0 + \frac{\beta^*}{2}\right) \sum_{j,k} 2^{-j\frac{\beta^*}{2}} \mathcal{S}\left\langle s, \psi_{j,k}^{\left(\alpha_0+\frac{\beta^*}{2}\right)}\right\rangle \psi_{j,k}^{(\alpha_0)}(t) \tag{3.7}$$

where $\mathcal{S}(w_{j,k})$ corresponds to the soft shrinkage applied to the wavelet coefficients, and the term $2^{-j\frac{\beta^*}{2}}$ represents the filtering operation as described in the previous step. The term $\kappa(\alpha_0, \alpha_0 + \frac{\beta^*}{2})$ defined as,

$$\mathcal{K}\left(\alpha_0, \alpha_0 + \frac{\beta^*}{2}\right) = (4\pi)^{\frac{\beta^*}{2}-\alpha_0} \frac{2^{\alpha_0+1}-1}{2^{\frac{\beta^*}{2}+1}-1} \frac{\zeta(\alpha_0+1)}{\zeta\left(\frac{\beta^*}{2}+1\right)} \tag{3.8}$$

is required to rescale the wavelet coefficients to account for the change of basis.

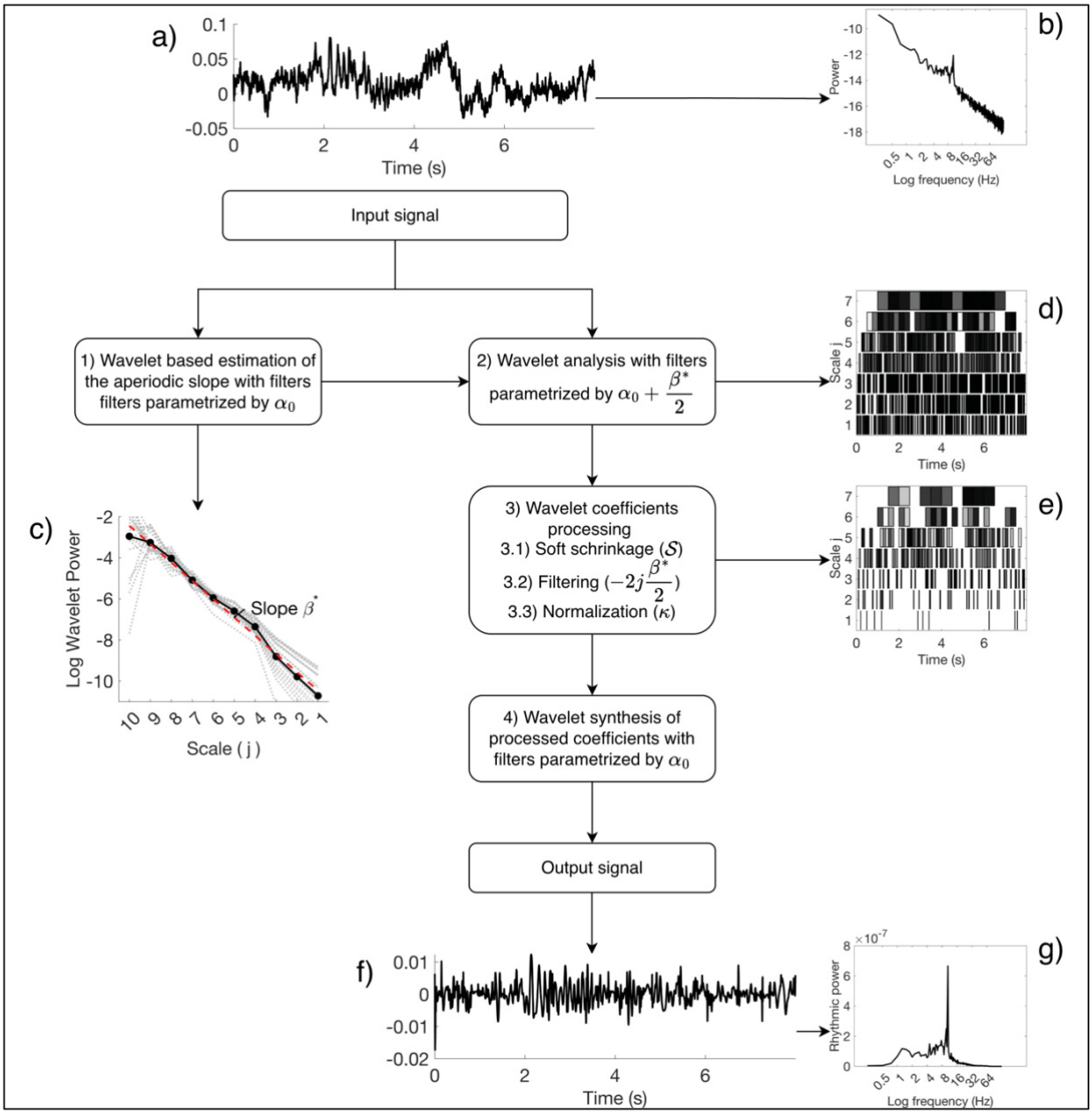

Figure 3.1 Processing steps of the *RnB* algorithm applied to a simulated signal. 1) The aperiodic exponent (β^*) is estimated by applying a linear fit to the log-mean squared of wavelets with filters parameterized by α_0. 2) The input signal is decomposed using fractional wavelet filters parametrized by $\alpha_0 + \beta^*/2$. 3) A soft shrinkage is applied to the wavelet coefficient, from which aperiodic activity is then filtered. The coefficients are then corrected to account for the change of wavelet basis. 4) The rhythmic signal is reconstructed via wavelet synthesis using filters parametrized solely by α_0. The final output is a signal with a suppressed aperiodic background, preserving its rhythmic features

3.3.4 Spectral analysis and aperiodic activity

For each sleep stage and each electrode, we computed 1) the relative average power spectrum of the standard and rhythmic signals and 2) the slope distribution across all epochs. The relative power consists of normalizing each band by the sum of the power across all bands. The resulting spectrum of the rhythmic signal for a given epoch exhibits the narrow-band spectrum of the original epoch, adjusted to account for the aperiodic slope. We calculated the power within the delta [1-4] Hz, theta [4-8] Hz, alpha [8-12] Hz, and sigma [12-16] Hz frequency bands. We also computed the rhythmic spectrum using the FOOOF algorithm (Donoghue et al., 2020) using default parameters to visually assess whether the two spectrums are concordant

3.3.5 Sleep spindles

We used the automatic spindle detector (Martin et al., 2013) on the standard and rhythmic signals from the same data subset and correspondingly applied the MP algorithm (Mallat & Zhang, 1993) only on the rhythmic signal. For both detectors, we calculated the average spindle density (number of spindles/minute). We also extract the number of corresponding spindles detected between both detectors. Figure 3.2 shows the detection of spindles in a standard signal and the corresponding rhythmic signal using both the standard and MP detectors. Although the MP algorithm was restricted to the rhythmic signal due to its computational demand, Fig. 3.2 illustrates that it could also be applied to the standard signal.

3.3.5.1 Automatic detector

The automatic detector first applies a bandpass filter (10 -16Hz) to the EEG data. The amplitude envelope of the filtered signal is obtained using the Hilbert transform and then smoothed. For each epoch, a detection threshold is set as the 90th percentile of the amplitude envelope to retain only high-amplitude events. Spindles are identified as continuous segments exceeding this threshold and are retained only if their durations range from 0.5 to 3 seconds.

3.3.5.2 Matching pursuit

Before applying the MP algorithm, a band-pass filter of 8- 24Hz was applied to the rhythmic signal to detect spindle events more accurately. The MP algorithm is based on a dictionary $\{D_i(t)\}$, which is a collection of functions (atoms), described according to their scale (s_i), onset (t_i) and frequency (f_i) and a phase index (k_i) (Mallat & Zhang, 1993).

$$D_i(t) \leftrightarrow \lambda_i = \{s_i, t_i, f_i, k_i\} \tag{3.9}$$

We constructed a dictionary to capture spindle-like oscillatory patterns by including atoms with characteristics typical of sleep spindles. The atoms are composed of Gabor functions with a frequency range from 8 to 24 Hz with increments of 0.2 Hz, a scale of 0.1-2.5 seconds with increments of 0.1 seconds and k = 0, 1. Each atom are centered at times $t_n = \frac{10n}{f_s}$ with n = 0,1,2 ... $\frac{N-1}{10}$. The Gabor functions used as atoms are defined as,

$$G_{\lambda_i}(t) = \sin\left(2\pi f_i(t - t_i) + \frac{k\pi}{2}\right) e^{-\frac{(t-t_i)^2}{2s^2}} \tag{3.10}$$

Where $k_i = 0$ or 1**.** The parameters f_i**,** t_i**,** and s_i represent frequency, time position and scale, respectively. Each atom can represent short oscillations at any point in time. Crucially, a combination of multiple atoms of different frequencies and scales can define a sleep spindle. MP iteratively selects an atom from a dictionary $\{D_i(t)\}$ that is most correlated with the current residual signal $r_n(t)$**.** For n = 0, the residual $r_0(t)$ corresponds to the EEG signal. At each iteration n, we find the best-matching atom from the dictionary $\{D_i(t)\}$**,**

$$i^* = argmax_i(|\langle r_n, D_i \rangle|) \tag{3.11}$$

and we remove the selected atom from the dictionary. Given the index i^***,** we update the residual for the next iteration,

$$r_{n+1}(t) = r_n(t) - \langle r_n, D_{i^*} \rangle D_{i^*}(t) \tag{3.12}$$

This process is repeated until 500 atoms have been selected. From the selection, only atoms with f_i within the 11 to 16 Hz frequency range and with s_i from 0.1 to 1 seconds are considered. The final step consists in selecting the atoms that will be used to construct the spindles. First, the envelopes of all atoms are summed to produce a time-varying signal that reflects the total envelope amplitude across atoms. A 5-second moving average $\mu(t)$ and the corresponding standard deviation $\sigma(t)$ of the envelopes are computed, and a threshold is defined as $\theta(t)$ =

$\mu(t) + 0.25\sigma(t)$. Atoms whose envelopes exceed $\theta(t)$ are retained, while the remaining atoms are discarded. The selected atoms are grouped into clusters based on temporal overlap, where any intersection is considered an overlap. Because a spindle is more complex than a single Gabor function, we kept 80% of the clusters that had at least two atoms. Also, clusters with a duration between 0.5 and 2.5 seconds are retained. Finally, we compute the energy of each cluster and keep clusters with energy above the sum of the mean and standard deviation across all clusters. This thresholding retains high-energy clusters as detected spindles.

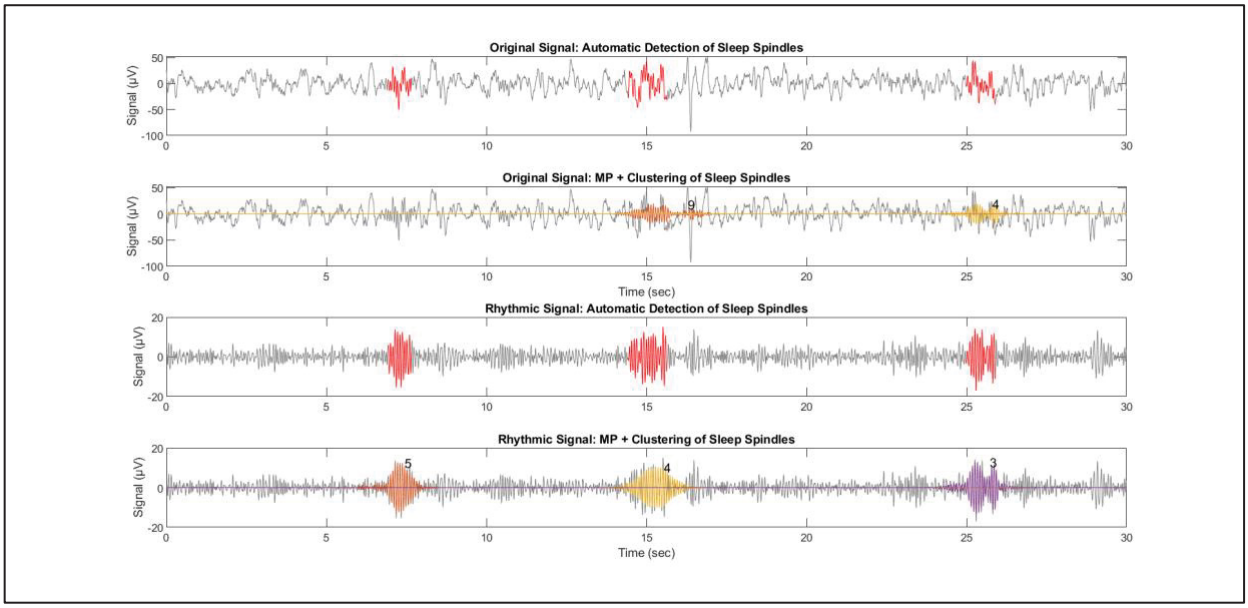

Figure 3.2 This figure illustrates the detection of one standard epoch and its corresponding rhythmic signal. The first two plots show the spindles detected by the standard detector on the raw and corresponding rhythmic signals respectively. The last two plot shows the MP detection applied to the standard and the rhythmic signal. The detected spindles are shown in colour. In the two bottom plots, each detected spindle is shown with the number of atoms in each cluster

3.3.6 Statistical analysis

All epochs were curtailed at 1.5 SD from the mean to attenuate the effects of outliers (across all variables, up to 20% of data were curtailed). Log transformations were applied on spectral power to improve normality as assessed with the Shapiro-Wilk test. Two-way mixed analyses of variance (ANOVAs) with one within-subject factor (sleep stages: N2 and N3) and between-

subject factor (age groups: Young and Older adults) were conducted on spectral power for each frequency band at each electrode (F3, C3, and O1) and on the aperiodic slope. Simple main effects analyses were used to decompose significant interactions. Based on a Bonferroni correction for series of 12 tests (4 frequency bands at 3 electrodes), the level of significance was set at $p < 0.004$.

3.4 Results

We investigated spectral power differences across frequency bands (delta, theta, alpha, sigma) between NREM2 and NREM3 in younger and older participants. Figures 3.3 and 3.4 illustrate the relative standard and rhythmic power for young and older adults, respectively, along with their slope distributions. Figure 3.5 illustrates the rhythmic spectrum using FOOOF. Results for the standard and rhythmic relative power, as well as the aperiodic slope, are presented in Table 3.1. Finally, we computed spindle density during NREM2, and the correspondence between spindles detected using the automatic detector and MP algorithm is reported in Table 3.2.

3.4.1 Standard relative power

Across all frequency bands and electrodes, there was a significant interaction between sleep stage and age for standard relative spectral power, except for theta at F3. For all electrodes, standard delta power increased from NREM2 to NREM3 in both age groups, but this effect was attenuated in older compared with younger adults. Standard theta power decreased from NREM2 to NREM3 at O1 and C3, but not at F3, in both age groups, but this effect was attenuated in older compared to younger adults. For F3, there was a main sleep effect, with a decrease in power from NREM2 to NREM3 ($F = 564.4$, $p < 0.001$, $np^2 = 0.91$). Standard alpha and sigma power decreased from NREM2 to NREM3 across all electrodes in both age groups, but this effect was attenuated in older compared with younger adults.

3.4.2 Rhythmic relative power

There was a significant interaction between sleep stage and age in rhythmic spectral power across all electrodes for delta, theta, and sigma, but not for alpha rhythmic relative power. Rhythmic delta power was increased from NREM2 to NREM3 across all electrodes and age groups, but this difference was significantly attenuated in older adults. In younger adults, rhythmic theta power was increased from NREM2 to NREM3 at all electrodes sites. Among older participants, there was no significant difference in rhythmic theta across sleep stages. A main sleep effect showed that rhythmic alpha power was higher in NREM2 than in NREM3 at electrode O1 ($F = 155.7$, $p < 0.01$, $np^2 = 0.73$), but there was no significant sleep stage difference at F3 or C3. There was no significant main effect of age on rhythmic alpha power at any electrode. Finally, rhythmic sigma power decreased from NREM2 to NREM3 in both age groups, but this was significantly attenuated in older adults.

3.4.3 Aperiodic exponent

There was a significant interaction between sleep stages and age across all electrodes. The aperiodic slope was steeper in NREM3 than in NREM2 in both age groups, with an attenuated difference between sleep stages in older adults. Additionally, older adults have a significantly shallower slope than younger adults, but this age difference emerges only in NREM3, not NREM2. Also, an anterior–posterior gradient was observed across both sleep stages and age groups, with F3 showing a steeper slope than O1.

3.4.4 Spindles

Using the automatic detector, we obtained a spindle density of 3.5/min in NREM2, both on the standard signal and the rhythmic signal. Using the MP algorithm on the rhythmic signal, we obtained a lower density of 3/min.

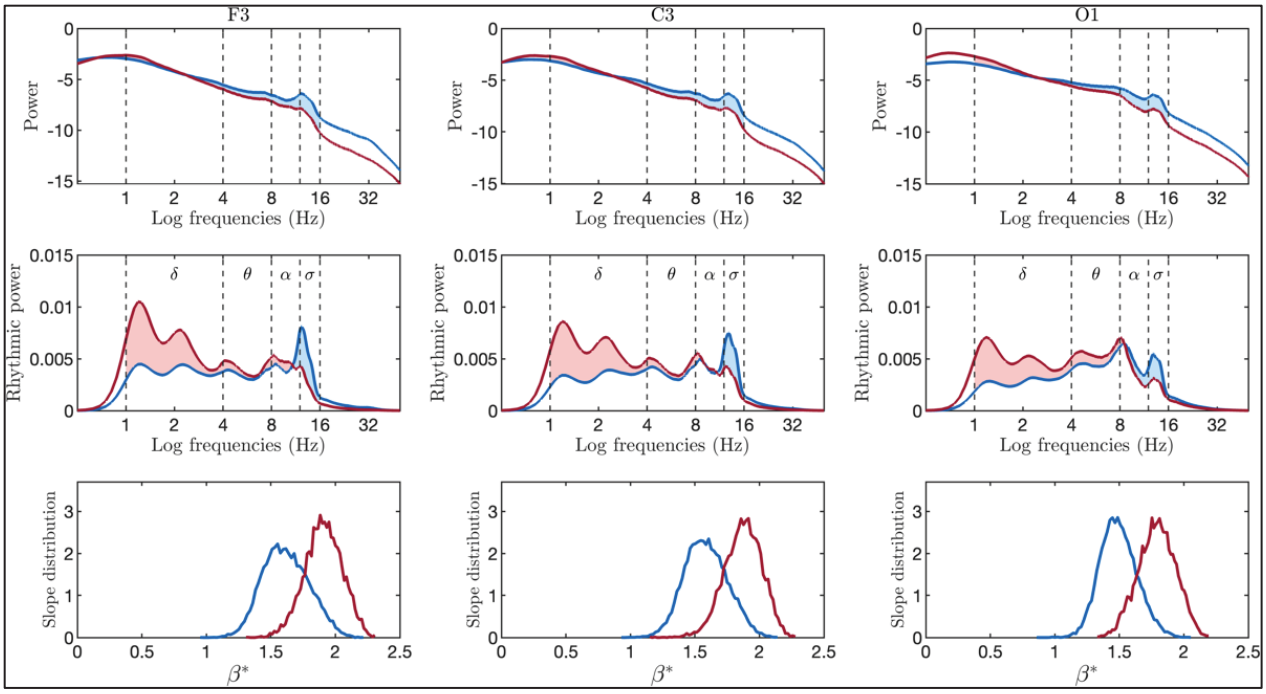

Figure 3.3 Relative power spectra (top row) and relative rhythmic spectra (bottom row) for F3, C3 and O1 electrodes in young adults during NREM2 (blue) and NREM3 (red) sleep. Light red indicates higher power in NREM3, and light blue indicates higher power in NREM2. Vertical dashed lines mark the canonical frequency band boundaries: delta (1-4 Hz), theta (4-8 Hz), alpha (8-10 Hz), sigma (12-16 Hz). The last row shows the slope distribution for NREM2 and NREM3 across electrodes

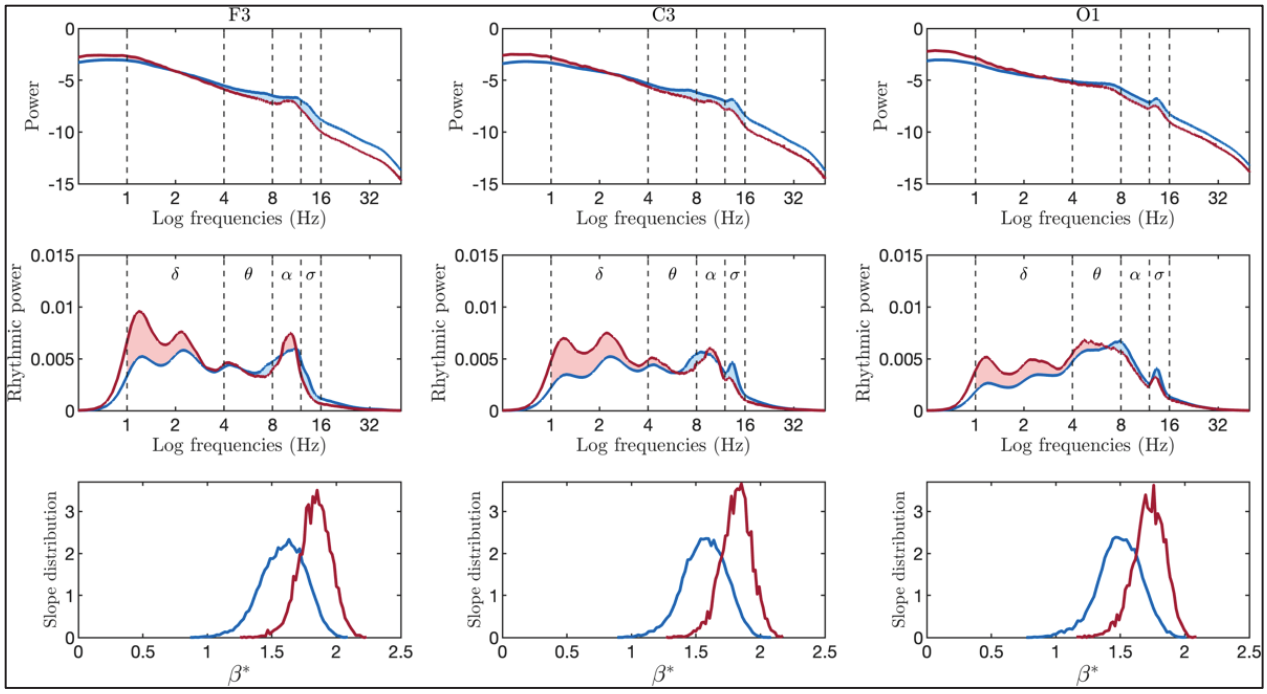

Figure 3.4 Relative standard power (top row) and relative rhythmic power (bottom row) for F3, C3 and O1 electrodes in old adults during NREM2 (blue) and NREM3 (red) sleep. Light red indicates higher power in NREM3, and light blue indicates higher power in NREM2. The last row shows the slope distribution for NREM2 and NREM3 across electrodes

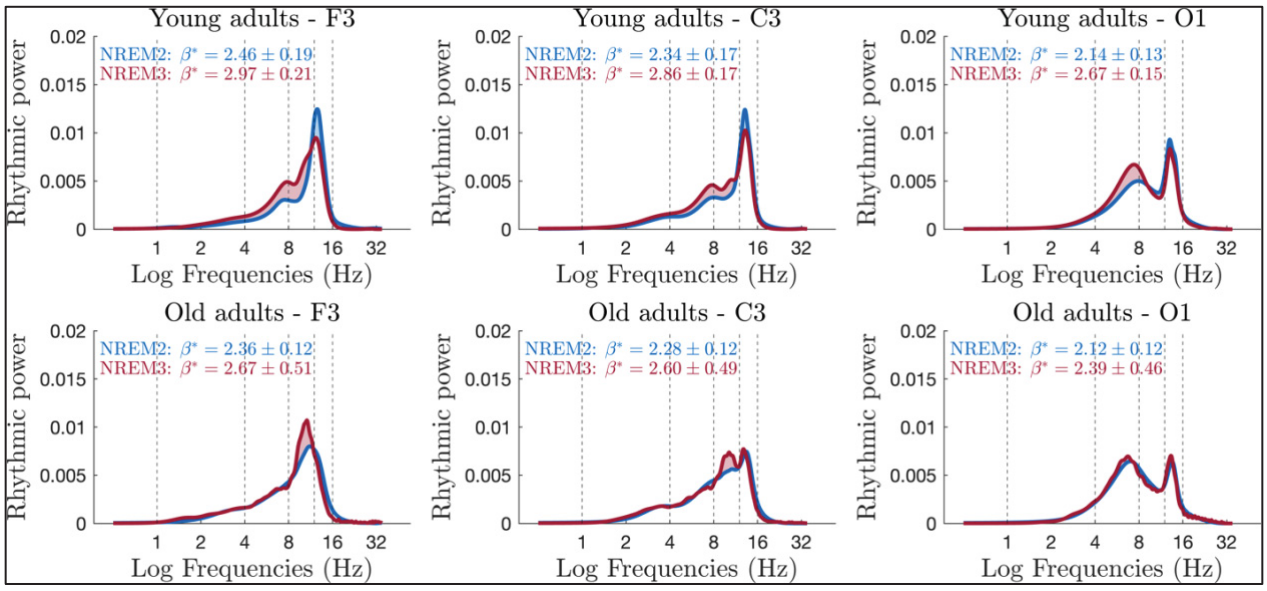

Figure 3.5 This figure shows the FOOOF rhythmic power for young participants (top row) and old participants (bottom row) at the F3, C3 and O1 electrodes during NREM2 (blue) and NREM3 (red) sleep

Table 3.1 Means, standard deviations (SD) and statistics for the sleep stage by age interactions across all electrodes and sleep stages for both young and older subjects, for the standard and rhythmic relative power and the aperiodic spectral slopes. bolded results denote a significant interaction

	Young NREM2 Mean ± SD	Young NREM3 Mean ± SD	Older NREM2 Mean ± SD	Older NREM3 Mean ± SD	Sleep X age			Young NREM2 vs NREM3	Older NREM2 vs NREM3
					F	P	np2	p	p
Standard Relative Power									
Delta									
F3	73.8 ± 5	87.3 ± 3.8	74.5 ± 5.5	84.9 ± 3.9	**9.3**	0.004	0.14	<0.001	<0.001
C3	68.2 ± 4.5	85.2 ± 3.5	69 ± 6.3	81.9 ± 4.1	**10.3**	0.002	0.15	<0.001	<0.001
O1	57.5± 5.3	78.3 ± 5	56.3 ± 5.7	70.4 ±6.2	**19.4**	<0.001	0.25	<0.001	<0.001
Tetha									
F3	13.9 ± 2.2	8.3 ± 2	14.9 ± 2.9	9.4 ± 2	2.9	0.091	0.05		
C3	16.9 ± 2.4	9.8 ± 2	18 ± 3.6	11.5 ± 2	**8.9**	0.004	0.13	<0.001	<0.001
O1	24.7± 3.7	15.7 ± 3.7	29.5 ± 4.9	21.9 ± 5.1	**12.6**	<0.001	0.18	<0.001	<0.001
Alpha									
F3	6.9 ± 2.3	3.2 ± 1.9	7.7 ± 3.1	4.7 ± 2.6	**15.5**	<0.001	0.21	<0.001	<0.001
C3	7.7 ± 2.4	3.2 ± 1.7	8.5 ± 3.1	4.8 ± 2.4	**18.5**	<0.001	0.24	<0.001	<0.001
O1	10.6 ± 2.7	4 ± 1.3	9.2 ± 2.5	5.1 ± 1.6	**39.7**	<0.001	0.40	<0.001	<0.001
Sigma									
F3	5.4 ± 2.5	1.2 ± 0.7	2.9 ± 1.4	1 ± 0.5	**43.5**	<0.001	0.42	<0.001	<0.001
C3	7.2 ± 2.8	1.7 ± 0.8	4.4 ± 2.1	1.7 ± 0.8	**48.3**	<0.001	0.45	<0.001	<0.001
O1	7.3 ± 2.7	2 ± 0.8	4.9 ± 2.4	2.6 ± 1.3	**84.8**	<0.001	0.59	<0.001	<0.001
Rhythmic Relative Power									
Rhythmic Delta									
F3	22.1 ± 5.3	32.6 ± 7	26 ± 6.8	32.2 ± 8.8	**21.7**	<0.001	0.27	<0.001	<0.001
C3	19.4 ± 4.5	30.9 ± 6.3	22.8 ± 6.6	29.9 ± 7.3	**19.6**	<0.001	0.25	<0.001	<0.001
O1	15.9 ± 3.3	25.9 ± 4.6	17.9 ± 4.9	23.4 ± 5.8	**28.9**	<0.001	0.33		
Rhythmic Tetha									
F3	23.1 ± 4.7	26 ± 4.7	26.6 ± 5.6	25.4 ± 5.3	**23.8**	<0.001	0.29	<0.001	0.054
C3	23.9 ± 5.1	27 ± 4.7	27.5 ± 5.8	26.7 ± 4.1	**22**	<0.001	0.27	<0.001	0.372
O1	30.4 ± 5.6	35.3 ± 4.6	38.2 ± 7.2	38.8 ±6.6	**26.3**	<0.001	0.31	<0.001	0.356

Table 3.1 Means, standard deviations (SD) and statistics for the sleep stage by age interactions across all electrodes and sleep stages for both young and older subjects, for the standard and rhythmic relative power and the aperiodic spectral slopes. bolded results denote a significant interaction

	Young NREM2 Mean ± SD	Young NREM3 Mean ± SD	Older NREM2 Mean ± SD	Older NREM3 Mean ± SD	Sleep X age			Young NREM2 vs NREM3	Older NREM2 vs NREM3
					F	P	np2	p	p
Rhythmic Relative Power									
Rhythmic Alpha									
F3	28.4 ± 6	27.9 ± 8.8	32.4 ± 7.8	33.1 ± 11.1	0.8	0.381	0.01		
C3	26 ± 5.1	24.6 ± 7.4	29.8 ±6.7	29.4 ± 8.5	1.5	0.218	0.03		
O1	28.8 ± 5.1	23.5 ±4.2	26.1 ± 5.3	22.8 ± 5	**5**	0.028	0.08	<0.001	<0.001
Rhythmic Sigma									
F3	26.4 ± 8.4	13.4 ± 6.4	15 ± 5.3	9.3 ± 3.6	**17.1**	<0.001	0.23	<0.001	<0.001
C3	30.5 ± 8.2	17.4 ± 6.4	19.8 ± 6.5	13.9 ± 4.7	**20.1**	<0.001	0.26	<0.001	<0.001
O1	24.8 ± 7.1	15.3 ± 4.9	17.6 ± 6.5	14.9 ± 5.7	**47.3**	<0.001	0.45	<0.001	<0.001
Aperiodic Slope									
F3	1.62±0.01	1.9 ± 0.01	1.59 ± 0.01	1.81 ±0.01	**32.1**	<0.001	0.35	<0.001	<0.001
C3	1.59±0.01	1.86±0.01	1.57 ± 0.01	1.79 ± 0.01	**22.7**	<0.001	0.28	<0.001	<0.001
O1	1.5 ± 0.01	1.78±0.01	1.5± 0.01	1.7 ± 0.02	**50.6**	<0.001	0.46	<0.001	<0.001

Table 3.2 Summary of spindles detected using different detection approaches on the standard and rhythmic signals. For each subject (row) and detection approach (column), four values are reported: total, match 1, match 2, and unmatched. For each cell, total denotes the number of spindles detected from the detector specified in the column header. Match 1 and Match 2 indicate the number of those spindles corresponding to detections obtained from the other two signals. Unmatched denotes the number of spindles with no corresponding detection in either of the other two signals

Subjects	Standard detector on raw signal	Standard detector on rhythmic signal	MP on rhythmic signal
	Total spindles, rhythmic match, MP match, unmatched	Total spindles, raw match, MP match, unmatched	Total spindles, raw match, rhythmic match, unmatched
1	16,16,12,0	16, 16, 12, 0	16, 16, 12,4
2	15, 15, 9, 0	15, 15, 9, 0	15, 15, 9, 6
3	27, 27, 15, 0	28, 27, 15,1	15,15, 15,0
4	19,18,10,1	18,18,10,0	13,10,10,3
5	18,18,11,0	18,18,11,0	14,11,11,3
6	19,19,12,0	19,19,12,0	14,12,12,2
7	14,14,9,0	15,14,9,1	15,8,9,7
8	20,20,14,0	21,20,14,1	16,14,14,2
9	11,11,8,0	11,11,8,0	18,8,8,10
10	18,18,13,0	18,18,11,0	17,12,11,5
Total	177,176,111,1	179,176,111,3	153,111,111,42

3.5 Discussion

The *RnB* algorithm represents a substantial shift from current quantified EEG methods by providing time series that reflect rhythmic activity. In addition to the usual spectral analysis that accurately characterised the resonances of the signal, this time series give access to signal decoding of the canonical graphoelements. Achieving this goal required a specific wavelet-based signal-processing framework to estimate and attenuate the aperiodic background of the EEG signal. When working within the spectrum, the signals associated with these components are not available, which limits our understanding of their interference (Donoghue et al., 2020 ; Wen & Liu, 2016). Therefore, time-resolved information must be incorporated to extend the current characterization method of rhythmic and aperiodic activity to the signal level.

Cerebral rhythms occur across a wide range of contexts (Buzsáki & Draguhn, 2004). Some are associated with pathologies, such as epileptic spiking activity, or with non-pathological conditions, including resting alpha rhythms. We focus on NREM sleep, where well-defined rhythms, such as spindles, occur, to illustrate the *Rnb* algorithm. Extracting a rhythmic signal is essential because it provides an inventory of rhythms that differs from that obtained from the standard signal, which contains aperiodic activity. This refined inventory should offer additional physiological insights in a clinical context. For example, it has been shown that obtaining such an inventory facilitates more effective investigations of rhythmic coupling (Dubé et al., 2024).

In our study, the rhythmic signal provides an inventory of rhythms that are mostly concordant with the literature, demonstrating the physiological relevance of the rhythmic signal extracted from the scalp EEG. We establish this by analyzing spectral features and assessing aperiodic activity across different levels of sleep depth in the context of aging. We also evaluated, with an illustrative example, the detection and the characterization of spindles from the rhythmic signal.

3.5.1 Aperiodic exponent estimator in the wavelet domain

Scalp EEG measures widespread cortical activity (Luo & Guan, 2018), whereas iEEG recordings are closer to the neural source, yielding a more localized measure of cerebral activity provided by the local field potentials (LFPs). As a result, scale-free dynamics are observed and quantified more clearly in iEEG data. Consequently, scalp recordings adhere less closely to a perfect power-law decay, reflecting a more complex mixture of aperiodic and rhythmic activity and are therefore less strictly scale-invariant. We therefore modified the slope estimator in Dubé et al. (2024) by relaxing the assumptions of a strict scale-free signal. The revised estimator (Eq. 3.3) better accommodated the characteristics of scalp EEG and provided reliable physiological features estimated from the signal's rhythmic and aperiodic components.

3.5.2 RnB algorithm applied to scalp EEG

3.5.2.1 Spectral analysis

Although some of these effects were modulated by age, standard relative power results reproduced typical sleep-stage effects, with increases in delta and decreases in theta, alpha, and sigma bands from NREM2 to NREM3. These findings are consistent with the dominance of low-frequency activity as sleep deepens. Since spectral power contains rhythmic and aperiodic components, this potentially obscures the specific contribution of rhythmic processes. Although standard relative power rescales the spectral power through normalization, it does not entirely remove the influence of aperiodic activity (Donoghue et al., 2022). Nevertheless, the relative spectral power of the rhythmic signal reveals patterns that differ from standard relative power analysis, yet still reproduce some well-established features of sleep physiology. This highlights the complex interplay between rhythmic and aperiodic activity.

Relative rhythmic power effects were modulated by age. In both age groups, the higher rhythmic delta activity in NREM3 compared to NREM2 aligns with the known dominance of slow-wave activity during deep sleep (Léger et al., 2018). Similarly, the higher rhythmic sigma activity in NREM2 compared to NREM3 is consistent with the higher density of sleep spindles

in NREM2, which decreases as sleep deepens (Andrillon et al., 2011 ; De Gennaro & Ferrara, 2003). In both rhythmic frequency brands (delta and sigma), aging was associated with reduced changes in rhythmic power between sleep stages, highlighting a loss of sleep-stage modulation with aging.

Rhythmic theta activity in young adults increased from NREM2 to NREM3 across all regions, deviating from classical sleep-stage effects (Borbély, Baumann, Brandeis, Strauch, & Lehmann, 1981 ; Dijk, Beersma, & van den Hoofdakker, 1989). While standard spectral measures (Zeitlhofer et al., 1993) typically report theta reductions across NREM, our results suggest that when rhythmic activity is isolated, rhythmic theta may undergo specific modulation during sleep. This discrepancy suggests that aperiodic activity may blur estimates of rhythmic activity. In Dubé et al. (2024), *RnB* was applied to iEEG data and revealed that when theta bursts co-occurred with rhythmic slow waves in the precuneus, the delta–sigma coupling strength was higher than when theta bursts were absent from rhythmic slow waves. Taken together, this further highlights that the *RnB* algorithm may uncover rhythmic activity obscured by aperiodic activity.

Based on our findings, mid-frequency bands (theta-alpha) are inherently influenced by aperiodic spectral properties, consistent with prior work showing that alpha-band power estimates are affected by the aperiodic background (Donoghue et al., 2020). Also, a recent study revealed that aperiodic spectral properties can strongly influence theta-band power estimates during working memory tasks (Frelih, Matkovič, Mlinarič, Bon, & Repovš, 2025). This suggests that alpha-theta band are sensitive to aperiodic activity across different neural states. Isolating rhythmic activity is essential, as standard spectral analysis may be driven by changes in aperiodic activity, which dominates the spectrum and can blur rhythmic power.

3.5.2.2 Aperiodic component distribution

RnB offers a more accurate characterization of scale-free activity and low-frequency power compared to spectral methods, because vanishing moments suppress polynomial trends during

signal decomposition (Abry et al., 2019). We obtained a steeper aperiodic slope in NREM3 compared with NREM2, which corroborates previous findings using spectral estimators of the slope (Bódizs et al., 2021 ; Lendner et al., 2020 ; Rosenblum, Jafarzadeh Esfahani, et al., 2025 ; Schneider et al., 2022). It is worth noting that we also observed a steeper slope in frontal regions relative to occipital sites. This topographic slope gradient aligns with the frontal dominance of low-frequency activity during NREM sleep (Horváth et al., 2022 ; Schneider et al., 2022). Aging was also linked to a flatter slope during NREM3, consistent with age-related changes in sleep aperiodic activity (Kozhemiako et al., 2022). In NREM2, aging was not associated with a flatter aperiodic slope. This may reflect the frequency range used to estimate the slope when applying the *RnB* algorithm (see Methods). Previous work has shown that aperiodic slope estimates depend on the frequency range, particularly when the spectrum exhibits an attenuation at low frequencies or multiple scaling regimes (Gerster et al., 2022), such that different frequency ranges may yield different estimates. In fact, when we estimated the slope using FOOOF over the frequency range (0.5–35 Hz), older adults showed a flatter aperiodic slope in NREM2, supporting our interpretation (see Fig 3.5).

3.5.2.3 Spindles

We show that spindles can be detected from rhythmic signals using the standard automatic detector and the MP algorithm, further showing that the rhythmic scalp signal contains physiological information. The MP is a data-driven approach that iteratively decomposes the signal using a dictionary of atoms designed to capture spindle rhythms. In this context, each detected spindle corresponds to a group of selected atoms, and the parameters of those atoms, such as their frequencies, provide insight into the frequencies that compose the spindle. An advantage of the MP is that rhythms are identified by matching them to the dictionary rather than by explicit amplitude-based detection thresholds, allowing the detector to adapt to the signal's features and individuals. A limitation is the computational cost, which could be mitigated by using GPU resources or by employing an alternative stopping criterion, such as an adaptive correlation threshold.

Using the standard detector on both the standard and rhythmic signals and applying MP to the rhythmic signal, we obtained a spindle density that falls within the range reported for healthy adults and reflects known inter-individual variability in sleep spindle measures (Coelho et al., 2025 ; De Gennaro & Ferrara, 2003 ; Höhn, Hahn, Lendner, & Hoedlmoser, 2024 ; Purcell et al., 2017). In general, there was a strong correspondence between the spindles detected in the standard and rhythmic signals (see Table 3.2), with each subject usually having at most one spindle that didn't correspond between them. Generally, there is no loss of spindle detection between the raw and rhythmic signal using the standard detector. However, the MP approach and the standard detector on the rhythmic signal showed differences in the correspondence of detected spindles. This is expected, as we are employing two different algorithms to detect spindles. Also, the atom selection procedure in the MP approach may impose stricter selection criteria, contributing to these differences in spindle inventory. Overall, our results confirm that the rhythmic signal contains meaningful physiological information through a valid spindle inventory in the sleep EEG recordings.

3.6 Conclusion and limitations

This study has some limitations. The analysis was limited to three electrodes, which may have limited the ability to fully capture the variations between sleep stages and age. Also, spindle detection was applied only to a subset of the data due to the computational load of the MP algorithm, which constrained the interpretability of the spindle results and restricted the algorithm's application to only the rhythmic signal.

In conclusion, this study assessed the spectral analysis of rhythmic signals and aperiodic activity and detected sleep spindles using the *RnB* algorithm. Applied to scalp EEG during NREM, *RnB* extracted an inventory of rhythms that reflects reliable sleep features. Additionally, the *RnB* framework advances current methodologies for characterizing rhythmic and aperiodic activity by extending spectral methods to the time domain. Future studies could apply *RnB* to determine whether rhythmic and aperiodic EEG components can reveal valuable new biomarkers of pathological sleep states. Also, since the *RnB* algorithm offers many

opportunities for analysis beyond spectral approaches, future work should investigate the source localization of sleep rhythms free of aperiodic activity and assess whether their source generators are more accurately estimated.

CHAPITRE 4

SPECTRAL ANALYSIS AND SCALE-FREE ACTIVITY OF TOPOGRAPHICAL MICROSTATES DURING NREM SLEEP

Michael Foti[1], David Smith[2,3], Rebecca Robillard[2,4], Jean-Marc Lina[1,5,6]

[1]Département de génie électrique, École de technologie supérieure, Montréal, QC, H3C1K3, Canada
[2]Institut de recherche en santé mental de l'Université d'Ottawa au Royal, Ottawa, ON, Canada
[3]Département de médecine cellulaire et moléculaire, Université d'Ottawa, ON, Canada
[4]École de psychologie, Université d'Ottawa, ON, Canada
[5]Centre d'Études Avancées en Médecine du sommeil, Hop. Sacré-Cœur de Montréal, Montréal, QC, H4J1C5, Canada
[6]Centre de Recherches Mathématique, Université de Montréal, Montréal, QC, H3C1J7, Canada

Article soumis pour publication dans la revue *Brain Topography* le 14 janvier 2026

4.1 Abstract

Microstates are quasi-stable electroencephalography (EEG) topographies describing large-scale brain activity. They are increasingly used to study brain dynamics and characterize neuronal disorders. Current analyses are primarily done in the time domain, where the neuronal dynamics are coded as a sequence of a finite number of microstates. The spectral properties of microstates could also offer valuable insights into neural activity. However, spectral analysis should address the sporadic sampling of the microstate sequences, which makes standard Fourier-based approaches inadequate. Microstates are obtained using the global field power (GFP), defined as the standard deviation across the scalp and reflecting the global field strength. In this study, we computed the spectrum of the GFP time series associated with each microstate sequence during NREM sleep in 61 healthy adults. We used the Lomb-Scargle algorithm to calculate the spectral power and handle the unevenly sampled microstate events. We observed and characterized a spectral decay that varies across sleep stages and age groups. We found that the GFP time series of microstate sequences exhibits scale-free dynamics, with the power spectrum following a 1/f like decay. The spectral slope of the decay was steeper

during NREM3 compared to NREM2 sleep and in younger compared to older individuals. These results suggest more organized global brain dynamics as sleep deepens, especially in younger individuals. Furthermore, our results suggest that the scale-free dynamics of the GFP, which are thought to reflect network engagement, may govern these large-scale processes.

4.2 Introduction

Electrical potential recordings measured on the scalp during sleep provide insight into the dynamics of spontaneous brain activity, enabling the characterization of various electrophysiological processes, such as restorative mechanisms and memory consolidation (Rasch & Born, 2013). NREM sleep encompasses many of these processes through synchronized brain rhythms, including sleep spindles during NREM2, generated by thalamocortical interactions and slow waves during NREM3, generated in the cortex and primarily originating in frontal regions (De Gennaro & Ferrara, 2003 ; Massimini et al., 2004). The global field power (GFP) is a time series of instantaneous electrophysiological power on the entire scalp, reflecting the dynamics of the overall electroencephalography (EEG) topography. It has been shown that the local maxima of the GFP, time points marked by high synchronicity in neural spontaneous activity, tend to align with topographies that can be clustered into a few distinct classes (Skrandies, 2007 ; Tomescu et al., 2014 ; Villar Ortega, Buetler, Aksöz, & Marchal-Crespo, 2024).The “centroids” associated with each cluster are commonly known as microstates (Lehmann et al., 1987). These distinct semi-stable configurations of potential fields on the scalp are thought to reflect simultaneous activation of specific nodes from brain networks, enabling to track temporal dynamics of brain states (Britz et al., 2010). There is a finite number of microstates (typically 4 to 7) representing canonical topographies that can be used to encode the entire EEG time series by assigning its most correlated microstate (Kleinert, Koenig, Nash, & Wascher, 2024). Historically, microstates have mainly been studied during resting state, with some studies extending to sleep (Bréchet et al., 2020 ; Brodbeck et al., 2012 ; Wiemers et al., 2024 ; Xu et al., 2020). Current work on microstates during sleep remains limited and has yet to address, as it has been done in the case of the rhythmic processes, how they vary as a function of both sleep stage and age.

Typically, microstate dynamics are characterized using metrics in the time domain, such as occurrence, duration, and transition probability. However, the spectral properties of microstate dynamics may provide crucial insights into the frequency content associated with distinct microstate classes. This would allow the quantification of rhythmic (transient burst of oscillatory events) and aperiodic (broadband process without characteristic time scale) properties of the microstate time series, offering a broader understanding of their dynamics.

Various methods have been proposed to describe the spectral content of EEG channels associated with microstates to infer global brain dynamics. However, these approaches fail to account for the GFP signal, which constitutes the fundamental signature used for the identification of the microstates. The spectral features of microstates have been extracted through a data-driven approach based on Empirical Mode Decomposition (EMD). EMD is an iterative decomposition of a signal into a set of Intrinsic Mode Functions (IMFs), which represent the main oscillations of the signal. A study using multivariate empirical mode decomposition was applied to multichannel EEG, followed by a Hilbert Transform on each IMF to obtain instantaneous frequency and amplitude estimates (Li et al., 2021). This approach provides instantaneous time-frequency spectra for each EEG channel (or topographic location), from which the spectral power is extracted at each time point associated with a given microstate. Another study used wavelet analysis to decompose the EEG signals from each electrode into its time-frequency content. The spectral power for each microstate was obtained at the specific microstate timing, and then averaged across all electrodes (Bréchet et al., 2020). EEG recordings during sleep have also been analyzed by comparing the time-lagged mutual information (AIF) of microstate sequences with the autocorrelation function (ACF) of the principal components of EEG signals (Wiemers et al., 2024). Their results suggest that spectral analysis of microstate sequences exhibit oscillatory patterns aligned with typical sleep EEG rhythms: alpha in wakefulness, theta in NREM1, sleep spindles in NREM2, and delta in NREM3. Overall, all these approaches depend on EEG channel-based proxies rather than measures that directly capture the dynamics of each individual microstate. Instead of analyzing the frequency content of microstates through each EEG channel individually, we propose a

more integrated approach considering both the spectral power of the GFP time series and the spectral analyses of the GFP time series associated with each specific microstate label sequence. For a particular microstate ($'l'$), we can extract the corresponding GFP time series denoted by GFP_l. A key challenge in applying spectral analysis to GFP_l is the irregular temporal occurrence of microstates, in contrast to continuous EEG and GFP that are sampled at uniform time steps. This makes usual spectral analysis techniques ill-suited. To this end, we propose using the Lomb-Scargle method, a spectral analysis technique commonly used in astronomy to evaluate irregularly sampled signals, such as the sparse occurrence of stellar activity (Scargle, 1982). This method is particularly well-suited to address the irregular occurrence of microstates.

In addition, irregularities of the electrophysiological signals associated with aperiodic activity during sleep have been recently studied in the wavelet domain (Lina, O'Callaghan, & Mongrain, 2019). Such analysis has been applied to microstates (Van De Ville et al., 2010) and to our knowledge, this was the first study to demonstrate that microstates, during resting state, reflect aperiodic activity. Aperiodic signals exhibit self-similar dynamics across a range of temporal scales. This implies that the statistical properties of the signal remain invariant when analyzed in a range of different timescales.

The present work aims to characterize the dynamics of microstate sequences during NREM2 and 3 sleep from two time series of interest: the microstate label sequences and the GFP sequences. First, building on the work of Van De Ville et al. (2010), we will assess whether the sequences associated with sleep microstates exhibit multifractal properties similar to those shown during wakefulness in resting state. Alongside this analysis, we will consider the spectral analysis of the GFP time series. Second, we describe the temporal statistics of NREM2 and NREM3 microstates as discrete events, that is, the mean occurrence and duration and their latency, which measures the interval between the end of a microstate and the onset of the next. Third, we will focus on the spectral properties of microstate sequences. Specifically, we performed a Lomb-Scargle analysis of GFP_l and we hypothesize that the GFP_l signals exhibit scale-free activity. Across all analyses, we will examine whether these characteristics of

microstate sequences change across NREM sleep stages and assess age effects as both shape sleep neurophysiology.

4.3 Materials and methods

4.3.1 Dataset

This study has used the SS3 database of the Montreal Archive of Sleep Studies (MASS), an open-access database of polysomnography (PSG) recordings obtained with ethics approval and informed consent (O'Reilly et al., 2014). The dataset includes 61 psychologically healthy subjects who were not taking any antidepressant medications. Participants were divided into two groups: young (n = 30, 21 ± 3 years) and older subjects (n = 31, 60 ± 5 years). Both age groups have similar sex distribution (47% females in the young adult group vs 61% in the older adults group, Chi-square = 1.3, p = 0.252).

Nineteen EEG electrodes were positioned according to the standard 10–20 system, and recordings were conducted at a sampling rate of 256 Hz. Sleep stages were scored based on the AASM criteria (American Academy of Sleep Medicine) (Iber et al., 2007). The data for each subject was segmented into 30-second epochs. We kept epochs free of muscle artifacts and micro-arousals. Depending on the availability of epochs from each sleep stage, we selected up to 15 minutes of clean epochs per subject.

4.3.2 Data processing

4.3.2.1 Microstate segmentation

Microstate analysis was performed using the microstate resting-state toolbox from EEGLAB (Nagabhushan Kalburgi et al., 2024). We first filtered the data between 1- 30 Hz. The identification of microstates proceeded in three steps. First, we computed the GFP time series defined as the standard deviation of the electrical potential across all electrodes for each sample. It is calculated as follows:

$$GFP(t) = \sqrt{\frac{1}{u}\sum_{i=1}^{u}\left(V_i(t) - \bar{v}(t)\right)^2} \tag{4.1}$$

$V_i(t)$ is the electrical potential at time t of the electrode i and $\bar{v}(t)$ is the mean across all electrodes, and u corresponds to the total number of electrodes. $GFP(t)$ is large for topographies with strong spatial gradients. The next step consists of detecting the local maxima of the GFP signal. The scalp potential topographies corresponding to these GFP peaks are then classified using a modified k-means clustering algorithm to identify a finite number of clusters (i.e microstates) topographies for each subject.There is currently no consensus to determine the number of microstates (Nagabhushan Kalburgi et al., 2024). We selected five microstates, as it yielded the most similar topographies across subjects. In line with established methods, canonical microstates for each sleep stage were obtained by averaging the co-registered microstates across all subjects (Koenig et al., 1999). For each subject, these canonical maps were back-fitted to EEG recordings by assigning the best-matching microstate at each global field peaks (Nagabhushan Kalburgi et al., 2024). Between these peaks, microstates were assigned using a nearest-neighbour approach. For each subject and sleep stage, this process generated a sequence of assigned microstates. We thus have two time series, in addition to the previous sequences of labels, the primary signal of interest is the GFP that indicates the strength of the corresponding microstates. Each subject had up to 15 minutes of data in NREM2 and NREM3 sleep, segmented into 30-second epochs. Each epoch includes a sequence of GFP values and corresponding microstate labels. For each microstate sequence of a label, we can extract the corresponding GFP_l sequence, where l corresponds to the microstate labels.

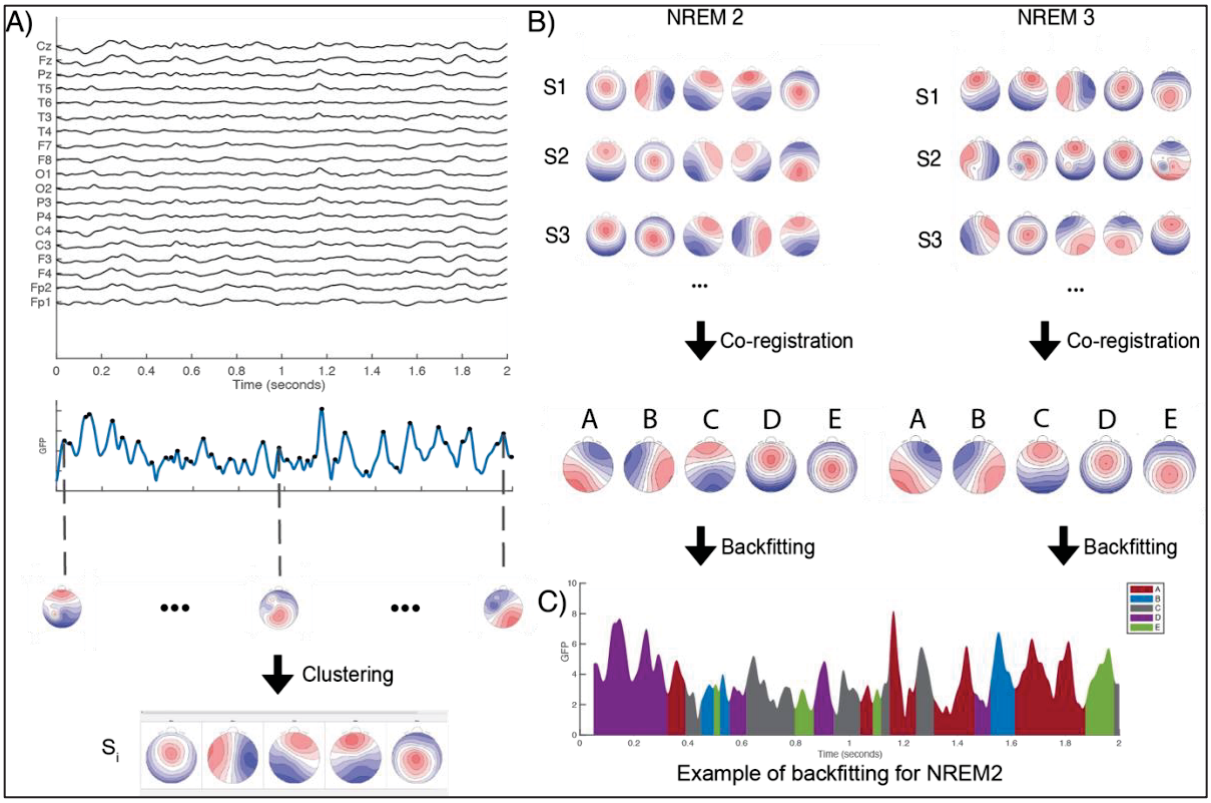

Figure 4.1 Microstate processing steps. A) Individual subject maps are obtained through clustering of the scalp topographies. B) These subject-level maps are then co-registered to generate a set of canonical microstate maps for NREM2 (left) and NREM3 (right). C) The canonical maps are subsequently backfitted to each subject's EEG time series for NREM2 and NREM3, respectively, yielding sequences of microstate labels for each epoch of the sleep stages. A 2-second interval is shown; analysis was performed on 30-second epochs

4.3.2.2 Multifractal analysis

We followed the multifractal analysis of microstate dynamics implemented by Van De Ville et al. (2010). The process first necessitated a 'balanced' partition of the microstates to ensure that no microstate is disproportionately represented. We thus grouped microstates into sets of two and three microstates (i.e. A and C, and B, D, and E). In total, there are 10 possible groupings. Each group is then assigned a value of +1 or -1, and the microstate sequence is encoded accordingly. Finally, the random walk was obtained as the cumulative sum of the coded time series.

The multifractal analysis was performed using the wavelet leader and bootstrap-based multifractal analysis (WLBMF) toolbox (Wendt & Abry, 2007). We used a discrete wavelet transform (DWT) to represent the signal into wavelet coefficients in the time-scale domain indexed by scale j, where scale j corresponds to different frequency bands. Similarly, to Van De Ville et al. (2010), we used Daubechies wavelet with five vanishing moments. Vanishing moments allow the wavelet transform to ignore polynomial trends present in the signal. Given that a signal may reflect multifractality across a specific set of scales only, we assess multifractality using the wavelet leader's framework across scales 6 to 12 (0.06–4 Hz).

Multifractal analysis characterizes the signal's irregularity through a parameter called the Hurst exponent (H). It takes a value between 0 and 1, where a value closer to 1 indicates a more irregular signal. For each subject and each NREM sleep stage, we extracted the average Hurst exponents of the random-walk that encoded the sequences of the microstates.

4.3.2.3 Spectral analysis of the GFP

In addition to the multifractal analysis, we compute the standard spectral power of the GFP time series using the fast Fourier Transform (FFT). Spectral power can be written as a combination of aperiodic and periodic contributions,

$$P(f) = \frac{C}{f^{\beta}} e^{R(f)} \tag{4.2}$$

Where $\frac{C}{f^{\beta}}$ represents the putative scale-free (aperiodic) activity of the spectrum and $R(f)$ represents oscillatory frequency components in the spectrum if any. $R(f)$ equal to zero corresponds to a pure scale-free activity. This scale-free activity is broadband, with power decreasing as frequency increases. Scale-free parameters for each subject and across each sleep stage were calculated with the Fitting Oscillations & OneOver-F (FOOOF) algorithm (Donoghue et al., 2020) . FOOOF is an iterative algorithm that models the power spectrum by fitting the aperiodic background $\left(\frac{C}{f^{\beta}}\right)$ and modelling the periodic components ($R(f)$) of the spectrum as Gaussian peaks. Spectral analysis based on the FFT of the GFP was applied on an

epoch-by-epoch basis for each subject and NREM sleep stage. The average spectrum was obtained for each subject, from which the aperiodic slope was estimated using FOOOF, between 1 and 8 Hz. We used the default parameters for FOOOF, except for the number of peaks, which was set to zero. Including periodic peaks introduced spurious frequency peaks attributable to overfitting. Therefore, we only consider the aperiodic fit. These settings were applied to all subsequent analyses using FOOOF algorithm.

4.3.2.4 Microstate standard characterization

We quantified the temporal properties of microstate sequences using three standard measures, for each subject and NREM sleep stage. First, mean occurrence [Hz], which indicates the average number of times per second that each microstate class appears. Second, mean duration, defined as the average duration of each microstate sequence measured in milliseconds. Third, mean latency, defined for each microstate as the mean duration between the end of a sequence and the start of the next. It describes the inactivity between two successive sequences in milliseconds.

4.3.2.5 Lomb-Scargle analysis of microstates

A GFP_l sequence can be associated with a microstate label. However, this sequence results in an irregularly sampling of the original GFP time series. To address the spectral characterization of this uneven sampling, we used the Lomb-Scargle framework (Scargle, 1982) that is well-suited for analyzing irregularly sampled time series.

For each subject and sleep stage, Lomb-Scargle spectral analysis was applied epoch-by-epoch to the GFP_l time series of each microstate sequence. The resulting spectrums were averaged across epochs to yield a spectrum for each subject's microstate. The aperiodic exponents from the Lomb-Scargle spectrums were obtained using FOOOF (see Fig. 4.2).

Lomb-Scargle algorithm :

When we extract a GFP sequence mapped to a given microstate, the resulting GFP_l timeseries is irregularly sampled. Such a signal cannot be addressed with the standard FFT. To address this challenge, Lomb-Scargle introduces a time shift (τ) to extend the spectral analysis to handle irregularly sampled signals,

$$P_{LS}(f) = \frac{{A_f}^2}{2}\left(\sum_n s(t_n)\, cos\big(2\pi f(t_n - \tau_f)\right)^2 + \frac{{B_f}^2}{2}\left(\sum_n s(t_n)\, sin\big(2\pi f(t_n - \tau_f)\right)^2 \tag{4.3}$$

In this expression, t_n corresponds to the irregularly spaced events. Additional parameters, amplitudes A_f and B_f, are introduced to control for the relative contributions of the two modes in the expansion. The case $t_f = 0$, $A_f = \sqrt{\frac{2}{\mathrm{N}}}$ and $B_f = \sqrt{\frac{2}{\mathrm{N}}}$ corresponds to the classical spectral analysis $P(f)$, based on an evenly sampled signal. To correctly analyze signals with uneven sampling, the following constraints are necessary and must be solved for A_f, B_f and t_f: 1) When data are regularly sampled, $P_{LS}(f)$ should match the classical definition, and 2) a global shift in time should not alter the spectral estimate of the periodogram $P_{LS}(f)$ (VanderPlas, 2018). Given those constraints, the unique solution was solved by Scargle (Scargle, 1982), enabling the spectral analysis of signals with unevenly sampled data.

$$A_f^2 = \frac{1}{\sum_n cos^2\big(2\pi f(t_n - \tau_f)\big)} \tag{4.4}$$

$$B_f^2 = \frac{1}{\sum_n sin^2\big(2\pi f(t_n - \tau_f)\big)} \tag{4.5}$$

$$\tau_f = \frac{1}{4\pi f} tan^{-1} \frac{\sum_t sin(4\pi f t_n))}{\sum_t cos(4\pi f t_n))} \tag{4.6}$$

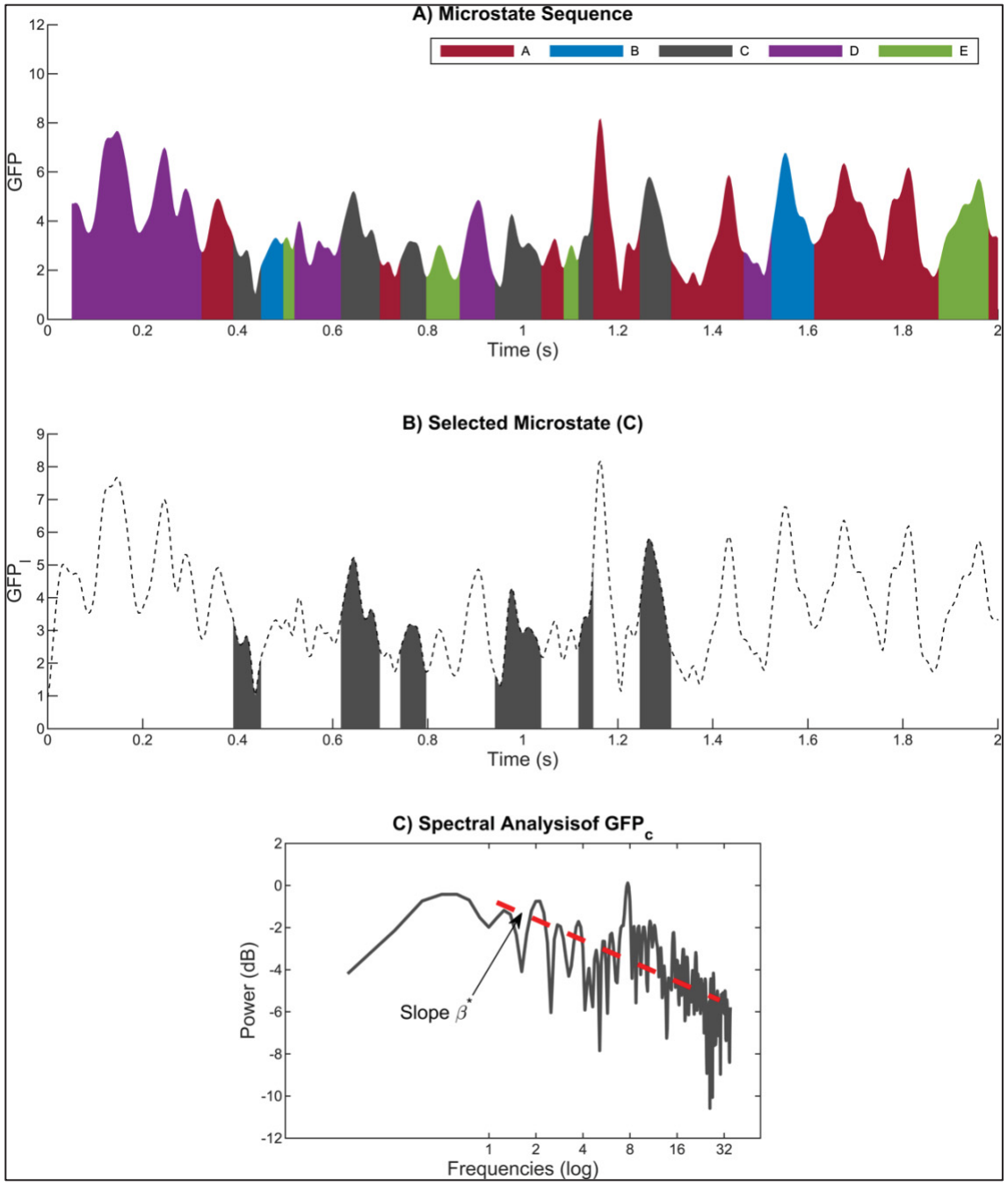

Figure 4.2 Spectral analysis applied to microstate sequence using the Lomb-Scargle algorithm

4.3.2.6 Shuffling the microstate sequences

To assess whether the most critical aspect of the spectral content of microstate sequences lies in the time series of the of GFP_l or in the sequence itself, we applied a spectral analysis under two distinct shuffling conditions to disrupt the temporal dynamics of the GFP or the microstate labels.

1. Label shuffling: Microstate labels were randomly shuffled while preserving the original GFP time series. This condition disrupts the sequential order of microstates while maintaining GFP fluctuations.

2. GFP intensity shuffling within microstates: GFP_l intensities were randomly shuffled within each microstate while keeping the microstate labels fixed. This condition disrupts the dynamics of GFP fluctuations while preserving the overall temporal structure of the microstate label sequence.

In both cases, the spectrum components were assessed using FOOOF to determine the changes in the spectrum caused by shuffling the data.

4.3.2.7 Statistical analysis

Two-way mixed ANOVAs with one within-subject factor (sleep stages: NREM2 vs NREM3) and one between-subject factor (age: young vs older adults) were conducted on the Hurst component and the FFT slope of the complete GFP. Three-way mixed ANOVAs with one within-subject factor (sleep stages: NREM2 vs NREM3), one between-subject factor (age: young vs older adults) and 5 microstates (A, B, C, D, E) were conducted on temporal and spectral parameters of microstates. For all analyses, when the assumption of sphericity was breached, the Greenhouse-Geisser correction was applied. Simple main effects were adjusted with a Bonferroni correction.

4.4 Results

4.4.1 Multifractal analysis of random-walk

No significant sleep stages by age interaction was found for the Hurst exponent ($F(1, 59) = 1.9$, $p = 0.175$, $\eta_p^2 = 0.031$). A main effect of sleep stages showed that the Hurst exponent significantly increased from NREM2 ($H = 0.62 \pm 0.02$) to NREM3 ($H = 0.63 \pm 0.02$) sleep ($F(1, 59) = 19$, $p < 0.001$, $\eta_p^2 = 0.24$). A non-significant trend for a main effect of age suggested lower Hurst exponents in older compared to younger adults ($F(1, 59) = 3.8$, $p = 0.056$, $\eta_p^2 = 0.06$).

4.4.2 Spectral analysis of GFP

From the average spectrum, the slope was analyzed in the 1–8 Hz range using the FOOOF algorithm (Donoghue et al., 2020). We selected this range because a distinct linear decrease in power was observable in the log-log spectrum. The spectral power of the GFP time series is illustrated in Fig. 4.4 (left). There was a significant sleep stage by age interaction for the FFT slope of the complete GFP ($F(1, 59) = 5.7$, $p = 0.020$, $\eta_p^2 = 0.09$). The FFT slope of the complete GFP significantly increased from NREM2 to NREM3 sleep in both age groups, but this increase was less pronounced in older adults ($F(1, 59) = 25.9$, $p < 0.001$, $\eta_p^2 = 0.31$) compared to young adults ($F(1, 50) = 69.9$, $p < 0.001$, $\eta_p^2 = 0.54$) .

4.4.3 Microstates characteristics

Figure 4.3 illustrates the mean occurrence, duration, and latency of each type of microstate across NREM2 and 3 stages for both young and older subjects.

4.4.3.1 Occurrence

There was a significant 3-way interaction between microstates, sleep stages, and age for microstates occurrence ($F(4,236) = 7.1$, $p < 0.001$, $\eta_p^2 = 0.11$). All microstates occurrence significantly increased from NREM2 to NREM3 sleep in both age groups (all $p < 0.001$, $\eta_p^2 > 0.38$), but this effect was modulated by age and microstates.

Significant sleep stage by age interactions were found for the occurrence of microstates A ($F(1, 59) = 7.0$, $p = 0.010$, $\eta_p^2 = 0.11$), C ($F(1, 59) = 7.3$, $p = 0.009$, $\eta_p^2 = 0.11$), D ($F(1, 59) = 13.7$, $p < 0.001$, $\eta_p^2 = 0.19$) and E ($F(1, 59) = 49.4$, $p < 0.001$, $\eta_p^2 = 0.46$), but not B (non-significant trend: $F(1, 59) = 4.0$, $p = 0.051$, $\eta_p^2 = 0.06$). Microstates A (similar trend for B) was significantly more frequent in older compared to younger individuals during both sleep stages, but the magnitude of this effect increased from NREM2 ($p = 0.046$, $\eta_p^2 = 0.07$) to NREM3 sleep ($p < 0.001$, $\eta_p^2 = 0.26$). Conversely, microstate C was slightly but not significantly more frequent in younger compared to older adults during NREM2 sleep ($p=0.128$, $\eta_p^2=0.04$) with more similar occurrence between the two age groups during NREM3 ($p=0.449$, $\eta_p^2=0.010$). Microstates D and E occurred less frequently in older compared to younger individuals during NREM2 sleep ($p < 0.002$, $\eta_p^2 > 0.16$), but did not differ significantly between age groups during NREM3 sleep ($p > 0.329$, $\eta_p^2 < 0.02$).

4.4.3.2 Duration

There was a significant 3-way interaction between microstates, sleep stages, and age for microstates duration ($F(3.2, 191.6) = 10$, $p < 0.001$, $\eta_p^2 = 0.15$). All microstates durations significantly lengthened from NREM2 to NREM3 sleep in both age groups (all $p < 0.001$, $\eta_p^2 > 0.51$), but this effect was modulated by age and microstates.

Significant sleep stage by age interactions were found for all microstates (A: $F(1, 59) = 17.7$, $p < 0.001$, $\eta_p^2 = 0.23$; B : ($F(1, 59) = 22.8$, $p < 0.001$, $\eta_p^2 = 0.28$; C: ($F(1, 59) = 29.7$, $p < 0.001$,

η_p^2 = 0.34; D: F(1, 59) = 22.6, p < 0.001, η_p^2 = 0.28; E: (F(1, 59) = 7.6, p = 0.008, η_p^2 = 0.11). Specifically, microstates A and B lasted longer in older compared to younger individuals during NREM2 sleep (p < 0.001, η_p^2 > 0.20), but did not significantly differ across age group during NREM3 sleep (p > 0.67, η_p^2 < 0.003). Microstate C was significantly longer in older compared to younger adults during NREM2 sleep (p = 0.037, η_p^2 = 0.07) but was significantly shorter in older compared to younger adults during NREM3 sleep (p = 0.005, η_p^2 = 0.13). The duration of Microstates D and E did not differ significantly between age groups during NREM2 sleep (p > 0.561, η_p^2 < 0.006) but were shorter in older compared to younger individuals during NREM3 sleep (p < 0.011, η_p^2 > 0.11).

4.4.3.3 Latency

There was a significant 3-way interaction between microstates, sleep stages, and age for microstates latency (F(3.2, 188.1) = 3.4, p = 0.018, η_p^2 = 0.05). All microstates latencies significantly increased from NREM2 to NREM3 sleep in both age groups (all p < 0.001, η_p^2 > 0.28), but this effect was modulated by age and microstates.

Significant sleep stage by age interactions were found for microstates A (F(1, 59) = 17.0, p < 0.001, η_p^2 = 0.22), B (F(1, 59) = 10.4, p = 0.002, η_p^2 = 0.15), D (F(1, 59) = 8.4, p = 0.005, η_p^2 = 0.13) and E (F(1, 59)=34.0, p < 0.001, η_p^2 = 0.37), but not C (p = 0.377, η_p^2 = 0.013). The latencies of microstates A and B were shorter in older compared to younger individuals during both sleep stages, but the magnitude of this effect increased from NREM2 (p<0.041, η_p^2>0.07) to NREM3 sleep (p < 0.001, η_p^2 > 0.21). The latencies of microstates D and E were longer in older compared to younger individuals during NREM2 sleep (p < 0.003, η_p^2 > 0.14), but did not differ significantly between age groups during NREM3 sleep (p > 0.224, η_p^2 < 0.03).

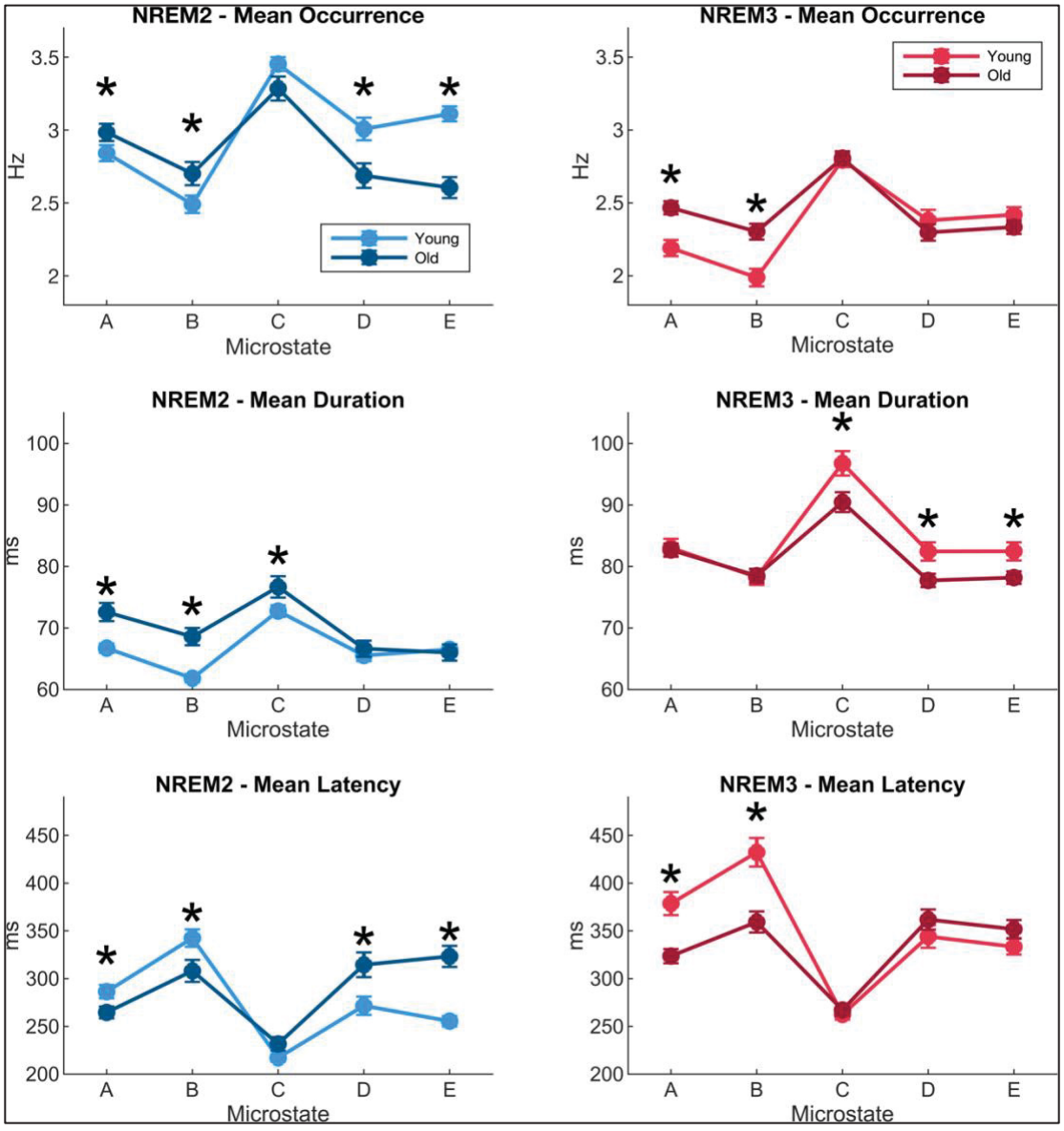

Figure 4.3 Microstate characteristics: mean occurrence (top row), mean duration (middle row), and mean latency (bottom row) of microstates A–E during NREM2 (left column) and NREM3 (right column) sleep, shown for young (lighter) and older (darker) individuals

4.4.4 Spectral analysis of GFP*l* microstate sequences

We assessed the mean spectrum across subjects using the Lomb-Scargle algorithm for NREM2 and NREM3, which is well suited to handle the irregular sampling of microstate sequences. This analysis revealed a low-frequency regime in the log-log space with high levels of power in the delta and theta ranges (1–8 Hz), and a drop in the spectrum power beyond ~8 Hz (see Fig. 4.3).

For the microstate sequences slopes, there was no significant 3-way interaction, nor interaction between microstates and sleep stages. A significant sleep stages by age interaction ($F(1, 58) = 4.4$, $p = 0.041$, $\eta_p^2 = 0.07$) showed that all microstates slopes significantly increased from NREM2 to NREM3 sleep in both age groups, but that this increase was less pronounced in older ($F(1, 58) = 66.6$, $p < 0.001$, $\eta_p^2 = 0.53$) compared to young adults ($F(1, 58) = 123.6$, $p < 0.001$, $\eta_p^2 = 0.68$).

A significant microstate by age interaction ($F(3.3, 189.2) = 4.7$, $p = 0.003$, $\eta_p^2 = 0.08$) showed that slopes were significantly lower in older compared to younger adults for all microstates, but that the magnitude of this age difference varied across microstates. Specifically, the largest age difference was observed in microstate D ($F(1, 58) = 30.1$, $p < 0.001$, $\eta_p^2 = 0.34$) and progressively declined from microstate D to C ($F(1, 58) = 16.1$, $p < 0.001$, $\eta_p^2 = 0.22$), to microstate E ($F(1, 58) = 11.0$, $p = 0.002$, $\eta_p^2 = 0.16$), to microstate A ($F(1, 58) = 8.4$, $p = 0.005$, $\eta_p^2 = 0.13$), and microstate B ($F(1, 58) = 5.1$, $p = 0.028$, $\eta_p^2 = 0.08$).

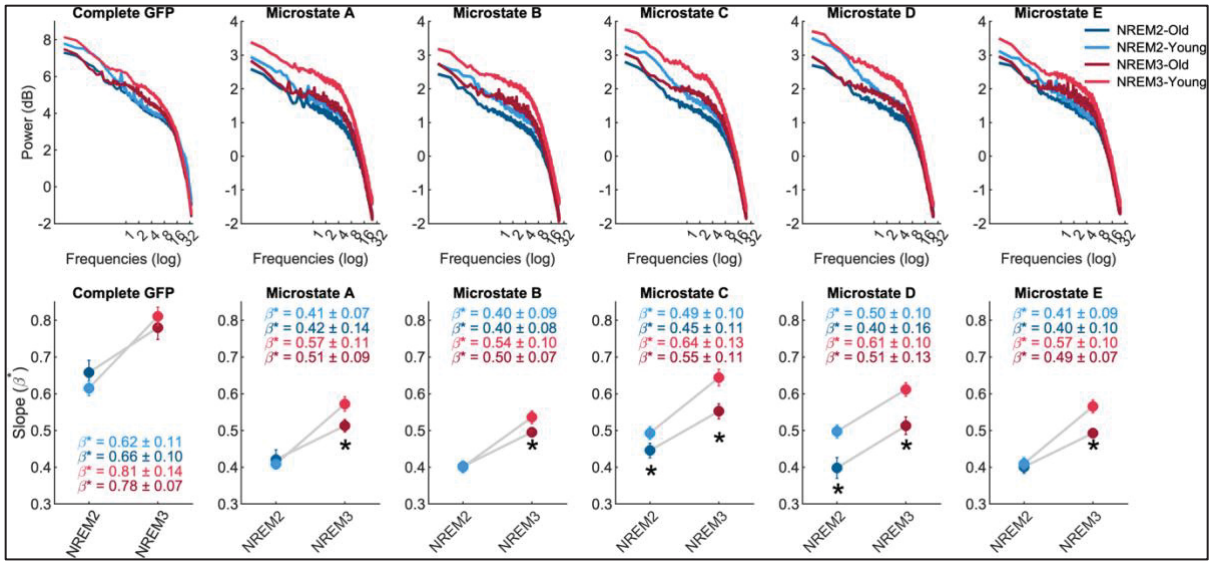

Figure 4.4 The top panels illustrate the spectral analysis for the complete GFP and microstate A-E during NREM2 (blue) and NREM3 (red) sleep stages for both age groups. The bottom panels show the slope (β^*= mean ± SEM) across sleep stages for both age groups, for the complete GFP and microstate A-E

4.4.5 Shuffling of the microstate sequence

Shuffling only the microstate labels while preserving the GFP time series maintained a scale-free property as spectral slopes persisted (see Fig. 4.4 A)). However, when GFP intensities were shuffled within each microstate label, the resulting spectrum became flat, indicative of white noise, and scale-free properties were disrupted (see Fig. 4.4 B)). In consequence, the scale-free property of the microstate dynamics as revealed by the Lomb-Scargle algorithm is an intrinsic property of the GFP time series.

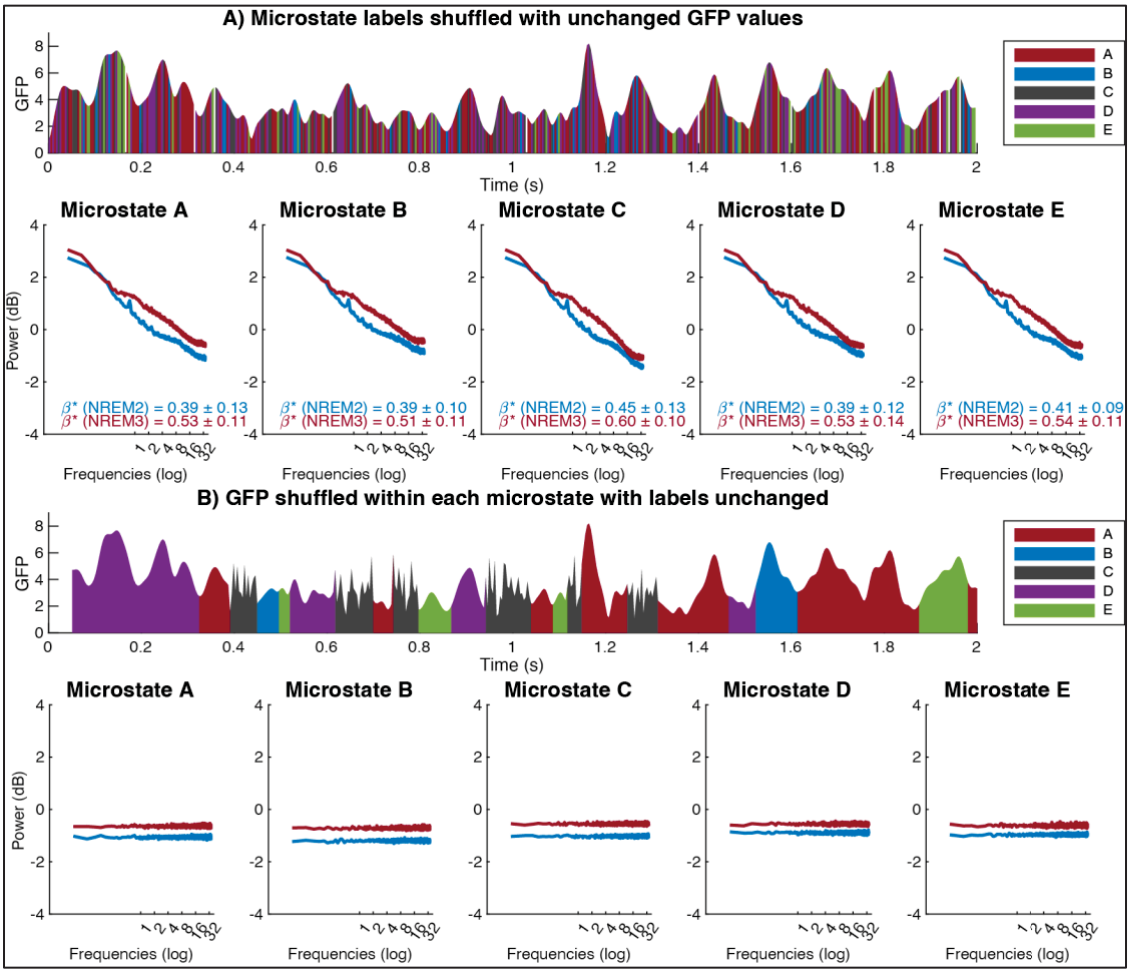

Figure 4.5 Spectral analysis applied to microstate sequences using the Lomb-Scargle algorithm for both shuffling conditions

4.5 Discussion

This study introduces the spectral analysis of microstate dynamics, drawing parallels to previous results obtained during wakefulness in resting state (Van De Ville et al., 2010), but with a new focus on NREM sleep stages and aging to anchor these new constructs in well known neurophysiological phenomena. Applying a 'coded' representation of the microstates dynamics described in Van De Vill et al. (2010) during wakefulness, we first showed that microstate sequences are multifractal during NREM sleep, with more temporal persistence of microstates during deeper sleep as suggested by a higher Hurst exponent during NREM3 compared to NREM2. The spectral analyses of the complete GFP time series during NREM

sleep confirmed that it was also scale-free. We then extended the spectral analysis to the microstates sequences using the Lomb-Scargle approach. To our knowledge, this is the first study to employ such an approach and investigate age-related changes in both spectral and temporal microstate metrics during sleep. Compared to their younger counterparts, older adults had microstates A and B which appear more frequently and more rapidly, especially during deeper sleep, and which lasted longer during lighter sleep. Their microstate C also lasted longer than younger adults during lighter sleep, but this effect was reversed during deeper sleep. Furthermore, the microstates D and E of older adults appeared less frequently and with slower latencies than those of younger adults in lighter sleep, and had briefer durations in deeper sleep.

We also showed that both the FFT slope of the full GFP and the slopes of individual microstates sequences steepened as sleep deepened, an effect that was attenuated by age. Importantly, the analyses for individual microstates sequences slopes revealed that although older individuals had lower slopes than young adults across all microstates, age-related changes in slope were most pronounced in microstates D and C. In the sections below, we interpret these findings in the context of established age-related changes to sleep and insights from EEG-fMRI studies.

4.5.1 Sleep-related age differences in microstate metrics

Prior work on microstates and healthy aging has focused on wakefulness, with resting-state studies showing that aging is associated with decreased occurrence of most microstates (Jabès et al., 2021 ; Tomescu et al., 2018 ; Zanesco, King, Skwara, & Saron, 2020). For instance, one study found a general decrease for all microstates, except for D which increased (Tomescu et al., 2018), whereas another found lower occurrences for microstates C, C', and D in older adults – with the reduction in D specific to the eyes-open condition (Jabès et al., 2021). Similarly, Zanesco et al. (2020) observed decreased occurrences across all microstates with age, reinforcing a broader pattern of less frequent microstate transitions in older individuals. Our results suggest that this previously observed age-related reduction in microstates during wake is also observed in light, but not deeper sleep, and that they are microstate dependent,

with microstates A and B actually showing the reverse pattern (increasing with age) during both light and deeper sleep.

Reports on age-related changes to microstate durations in the wake state have been somewhat mixed. Some studies found no significant age-related differences in microstate duration (Chen et al., 2019 ; Jabès et al., 2021 ; Stevens & Kircher, 1998), and another noted a trend towards shorter durations for microstates C, D, and E in older adults (Kashihara, Asai, & Imamizu, 2025). However, Zanesco et al. (2020) observed longer durations across all microstate topographies and Tomescu et al. (2018) reported longer durations for all microstates except C, which decreased in the oldest age category, particularly among females. Our results complement these previous findings suggesting that during sleep, this partially aligns with our observation of longer durations for microstates A, B and C in light sleep, but we extend these previous findings by unveiling that this effect is reversed in deeper sleep for microstates C, D and E.

In the context of sleep, prior work has shown that microstate durations increase from NREM2 to NREM3 (Brodbeck et al., 2012 ; Wiemers et al., 2024), a finding that was replicated here and accompanied by increased latencies for all microstates. Beyond global trends, microstate C has been reported to account for the highest global explained variance (GEV) (Wiemers et al., 2024) or to be most prominent in all stages except NREM2 (Brodbeck et al., 2012).

Overall, the current investigation bridges these areas of the microstate literature by unveiling that the nature of age differences in the temporal dynamics of microstates vary across levels of sleep depth and across microstates. Adding to the known age-related alterations in physiological functions affecting NREM sleep, our results suggests that during light sleep, older age is linked to more stable cortical networks underlying microstates A and B (as reflected by longer durations relative to younger adults), and a reduction of the amount of time spent in microstates D and E (as reflected by similar duration, yet lower occurrence and longer latencies relative to younger adults). These findings during NREM2 may relate to weakened integrity of thalamic projections to frontal and parietal cortical regions evident in older adults

during wake (Fama & Sullivan, 2015). One study found that the integrity of thalamic radiations to primarily the right hemisphere predicted age-related differences in spindle density at midline and right-lateralized EEG derivations during NREM sleep (Mander et al., 2017). These thalamocortical alterations suggest that aging may influence both lateral (left–right) and anteroposterior (front–back) axes of cortical organization, potentially affecting the occurrence or duration of microstates along both orientations.

Additionally, research suggests the thalamus facilitates slow wave transitions from Up to Down states and that silencing midline thalamic nuclei can extend Up state durations (Hay et al., 2021). It could be postulated that a diminished capacity of the thalamus to facilitate this switching during NREM2 may affect k-complexes, brief sequences of slow waves, and lead to prolonged microstates and thus greater temporal persistence of the cortical networks underlying microstates A, B and C in older compared to younger adults. This mechanism is supported by recent evidence showing that (a) thalamocortical connectivity is stronger during NREM2 than NREM3, where cortico-cortical connectivity predominates to generate sleep slow waves (Lambert et al., 2022), and (b) aging is associated with a decreased number of slow waves in NREM3 and an elevated number in NREM2 (McConnell et al., 2021).

Conversely, during deeper sleep, older age was linked to less prominent microstates C, D and E as reflected by shorter durations compared to younger adults, yet more prominent microstates A and B based on more frequent occurrence. Topographic changes to parameters of slow wave activity with age may be pertinent to our temporal microstate findings. For instance, changes to delta activity in central derivations during NREM sleep with age have been attributed to cortical thinning of the left medial orbitofrontal cortex, suggesting an influence of aging on slow wave propagation along an anteroposterior gradient (Latreille et al., 2019). Furthermore, computational modelling suggests that aging is associated with interhemispheric asymmetries in slow waves linked to corpus callosum integrity (Lupi et al., 2024), which is supported by empirical findings in patients who underwent total callosotomy(Avvenuti et al., 2020). Converging evidence thus suggests that aging alters slow wave generation and propagation along both lateral and anteroposterior axes, potentially manifesting as changes to the

occurrence of microstates A/B (lateral orientation) and the duration of C/D/E (anteroposterior orientation) during NREM3.

4.5.2 Lomb-Scargle spectral analysis of microstate sequences

We considered the GFP_l associated with microstate l to obtain a spectral description of each microstate's dynamic using the Lomb-Scargle algorithm. Similar to Fourier analysis, it assumes a decomposition into sinusoidal components. For each GFP_l, the label l denotes the most dominant configuration in the competition among all possible microstates for that sequence. Lomb-Scargle is particularly well-suited to characterize the lacunary GFP_l signals. This analysis of GFP_l within the 1-8 Hz frequency range revealed scale-free activity without distinct frequency peaks. In line with previous findings examining spectral slope changes across arousal states at individual electrodes (Lendner et al., 2020 ; Schneider et al., 2022), we confirmed a significantly higher spectral slope in NREM3 than in NREM2. This higher slope, promoting low frequencies, is consistent with our observation of lower occurrence and higher duration of the microstates during NREM3 compared to NREM2.

4.5.3 The lacunarity of the microstate's dynamics

The complete GFP spectrum shows a drop in power beyond around 8 Hz, indicating that it does not engage higher frequencies. When considering the GFP_l, we observe the same trend. However, when microstate labels were shuffled, with GFP time series remaining fixed, the spectral slope persisted without a drop in power. First, the fact that the scale-free activity persists suggests that the GFP time series is a critical determinant of the scale-free properties of the dynamics of the topographies. Second, when the label shuffling takes place, scale-free activity occurs on a larger spectral band. The label shuffling disrupted the temporal structure of individual microstate classes by breaking the sequences. This allows for shorter-duration states to emerge and increase transitions between the states. These shorter time scales are reflected in the spectrum as a continuation of scale-free activity into higher frequencies. Thus, the GFP_l spectrum encodes the latency of switches between different microstates providing possible insights into functional networks stability.

4.5.4 Persistence of microstates and criticality

A steeper spectral slope reflects more persistent activity, consistent with more stable neural dynamics, and higher mean duration. In healthy individuals at rest, microstates have been shown to exhibit scale-free dynamics, which may play an essential role in the brain's ability to transition between its functional networks (Van De Ville et al., 2010). Recent simulations showed that local connectivity affects aperiodic EEG activity, supporting that networks can influence scale-free brain activity (Brake et al., 2024). Microstates remain similar from wake to deep sleep, implying that functional networks remain active through sleep (Brodbeck et al., 2012). Within this framework, GFP_l may serve as an index of the engagement strength of a corresponding network. Our finding that GFP fluctuations follow scale-free dynamics suggests that when a given network is active, the strength of its engagement across the night is not governed by characteristic frequencies, but scale-free activity. These results align with simulations showing that local connectivity can shape scale-free activity (Brake et al., 2024) and further suggest that such scale-free properties may also be expressed globally by contributing to the amplitude dynamics of large-scale functional networks.

Although the presence of power laws does not prove that a system operates near a critical state, observing power-law behaviour across multiple parameters and scales of brain activity strengthens the case that the brain may be operating near criticality (Beggs & Timme, 2012). Our findings suggest that this may be the case during sleep. Notably, systems operating near this point are thought to be optimized in several functional characteristics, including dynamic range and information transfer (O'Byrne & Jerbi, 2022). It is possible that the scale-invariant relationship we observe between larger and smaller GFP fluctuations reflects this optimized state at the network level.

4.5.5 Spectral topographies of microstates C and D in aging

The spectral decays of microstate sequences in our study were shallower in older adults, and the magnitude of this difference was greatest for microstates D and C. The scale-free dynamics

of these microstates were thus the most sensitive to age-related changes in our sample. Interestingly, resting state studies report that the strength and coverage of cortical alpha activity shapes fMRI network connectivity (Scheeringa, Petersson, Kleinschmidt, Jensen, & Bastiaansen, 2012) and EEG microstate topography (Croce, Quercia, Costa, & Zappasodi, 2020 ; Milz, Pascual-Marqui, Achermann, Kochi, & Faber, 2017 ; Pascual-Marqui et al., 2014), and that microstates C and D exhibit the most spatially widespread alpha power (Milz et al., 2017). This finding is relevant to our results because EEG alpha power during wake is known to decline with age (Babiloni et al., 2006 ; Scally, Burke, Bunce, & Delvenne, 2018 ; Vysata, Kukal, Prochazka, Pazdera, & Valis, 2012) even when adjusting for the confounding influence of aperiodic activity (Tröndle et al., 2023). A source-localization study of spectral rhythms also demonstrated age-related reductions in alpha power that were pronounced in occipital, temporal, parietal, and limbic regions (Babiloni et al., 2006). Given that microstates C and D are associated with distributed alpha sources and have shown age-related differences in our study, these spectral findings may reflect underlying changes in the same large-scale functional networks captured by microstate dynamics. Furthermore, given the importance of alpha activity for determining network behavior in EEG and fMRI during wake, future research should explore the shaping influence of oscillatory and aperiodic activity on microstates during sleep, particularly given that age-related changes to alpha power in sleep are less consistent in the literature (Landolt & Borbély, 2001 ; Latreille et al., 2019).

Other source-space and EEG-fMRI studies point to diverse generators for our microstates D and C – or their closest approximations – spanning several major resting-state networks during wake (Britz et al., 2010 ; Custo et al., 2017 ; Pascual-Marqui et al., 2014) and sleep (Bréchet et al., 2020 ; Xu et al., 2020) , but differences in methods, modalities, and vigilance states constrain inferences regarding the sources underlying these microstates. For instance, in EEG-fMRI, Britz et al. (2010) link RSN3 and RSN4 (corresponding to our microstates C and D) with salience and attention networks, respectively, while Xu et al. (2020) connect their microstate C to deactivation of the control executive network, and microstate D to BOLD deactivation and activation of the visual and salience networks. In EEG, Custo et al. (2017) associate microstate C with the precuneus and posterior cingulate cortex, key hubs within the

default-mode network. Thus, while Custo et al. (2017) diverge from these EEG-fMRI studies on microstate C, there is otherwise broad agreement between their work and Britz et al. (2010), including the generators of microstate D/RSN4. This is tentatively supported by research connecting microstate D to executive functions during wake (Tarailis, Koenig, Michel, & Griškova-Bulanova, 2024), which are known to decline with age (Heckner et al., 2021).

Making inferences from an EEG source-localization study by Bréchet et al. (2020) is challenging because their work features topographies less closely aligned with canonical templates from Koenig et al. (2002). However, there is notably some agreement between two other EEG source-localization studies identifying hubs of the default-mode network (DMN) as common generators of most microstate topographies (Custo et al., 2017 ; Pascual-Marqui et al., 2014). Pasqual-Marqui et al. (2014) specifically show that microstate C has generators in the posterior cingulate cortex – part of the DMN – and anterior cingulate cortex, although the anterior cingulate could belong to several RSNs depending on the subregion involved. In contrast, microstate D is generated primarily from the posterior cingulate cortex. Interestingly, Pasqual-Marqui et al. (2014) highlight the importance of alpha – and to a lesser extent, beta – activity for cortical connectivity and specify the posterior cingulate as a common source of alpha and beta oscillatory information for other microstate generators. Further source-localization studies are sorely needed to resolve discrepancies in the literature, but there are hints from the extant research that aperiodic activity within regions of DMN and CEN (central executive network) may be susceptible to aging based on our microstate findings.

4.5.6 Potential for clinical biomarkers

Future studies should test whether these spectral features can reliably differentiate between healthy and pathological brain states, particularly given mounting evidence based on EEG recorded during wakefulness that microstates may serve as indicators of psychiatric illness or neurological impairment. For example, irregular microstate transitions have been reported in mood and anxiety disorders, including less frequent switching between microstates B and D, and more frequent transitions between A–D and B–C (Al Zoubi et al., 2019). In schizophrenia,

studies have described atypical dynamics such as reduced duration of microstates B and D and increased prevalence of microstates A and C (Lehmann et al., 2005). Altered microstate patterns have also been found in individuals who are genetically predisposed to schizophrenia, highlighting the sensitivity of microstate measures to underlying vulnerabilities or early pathophysiological processes (Tomescu et al., 2014).

Similarly, abnormal microstate dynamics have been observed in insomnia disorder. One study reported increased prevalence of microstate D and shorter durations of microstate C (Wei, Ramautar, Colombo, te Lindert, & Van Someren, 2018), while another found an elevated prevalence of microstates D and E at the expense of B and C (Weng, Jülich, & Lei, 2025). However, these findings – like those in other clinical populations – are based exclusively on resting-state EEG recordings. Future research will benefit from extending microstate analyses into sleep, given clinically relevant endogenous processes and its inherent nature as a closed-loop system that is less sensitive to external perturbations.

4.6 Conclusion and limitations

This study has some limitations. Since the scalp coverage was of 19 electrodes, a denser montage would provide more reliable measurements and reduce susceptibility to artifacts. Additionally, it would improve spatial resolution and lead to a more accurate GFP estimate, better reflecting the overall strength of large-scale neural dynamics. A denser montage would also allow us to incorporate source reconstruction of microstates, providing better insights into the neural generators underlying the spectral changes across age and sleep stages. Finally, the correspondence of our microstate maps was determined through visual comparison with existing studies. Although this approach is common, more objective microstate matching methods have recently been introduced to improve comparison across studies (Koenig et al., 2024).

In this study, we applied Lomb–Scargle spectral analysis to the GFP time series of microstate sequences during NREM sleep. We found that the GFP shows scale-free dynamics, with

spectral slopes varying by sleep stage and age-being steeper in NREM3 compared to NREM2, and in younger adults compared to older ones. These findings suggest that deep sleep involves more organised large-scale brain dynamics, and that aging may reduce this organization. Additionally, time-based microstate metrics revealed sleep stage and age dependent shifts in microstate dynamics. Although future research should verify reproducibility across different cohorts, our results highlight the scale-free nature of microstates and introduce the spectral slope of microstates as a measure of sleep neurophysiology.

CONCLUSION ET PERSPECTIVES

Cette thèse présente différents outils numériques développés pour caractériser les activités rythmiques et apériodique des enregistrements EEG intracrâniens et de scalp en sommeil NREM. Comme l'illustre la figure 4.6, les signaux EEG peuvent être analysés selon trois axes fondamentaux séparés ou en combinaison: la dynamique temporelle, l'activité spectrale et l'organisation spatiale. Plusieurs outils numériques permettent d'extraire des informations cliniques pertinentes dans ces trois domaines, selon la question clinique posée. Par exemple, pour les troubles du sommeil (insomnie), les rythmes canoniques du sommeil, obtenus par des algorithmes de détection, constituent des biomarqueurs, notamment par leurs densités (Dang-Vu et al., 2015). D'autre part, l'activité apériodique, caractérisée par une décroissance linéaire des spectres, représente également une information clinique importante pour l'analyse des troubles du sommeil (Andrillon et al., 2020). Enfin, les micro-états peuvent être associés à de l'information spatiale de l'EEG sur le scalp, permettant de caractériser des pathologies telles que la schizophrénie et la dépression (Khanna et al., 2015) .

Dans cette thèse, nous avons développé l'algorithme *RnB* pour dissocier l'activité rythmique et apériodique des signaux EEG, permettant d'obtenir une description exhaustive de l'information du signal aux niveaux temporel (rythmique) et spectral (apériodique). Sur le volet spatial de l'EEG, nous avons introduit l'algorithme de Lomb-Scargle pour caractériser l'activité apériodique des séquences de topographies de micro-états. Lomb-Scargle permet ainsi d'accéder à l'information fréquentielle et de caractériser l'activité apériodique à grande échelle des séquences irrégulières de micro-états. Globalement, l'ensemble de ces travaux permet une caractérisation plus complète et plus robuste de l'activité cérébrale, offrant des outils à valeur clinique. Le point commun entre ces deux contributions est une caractérisation plus spécifique de l'activité apériodique du signal électrophysiologique à l'échelle locale et globale. Concrètement, cette thèse a donné lieu à trois contributions.

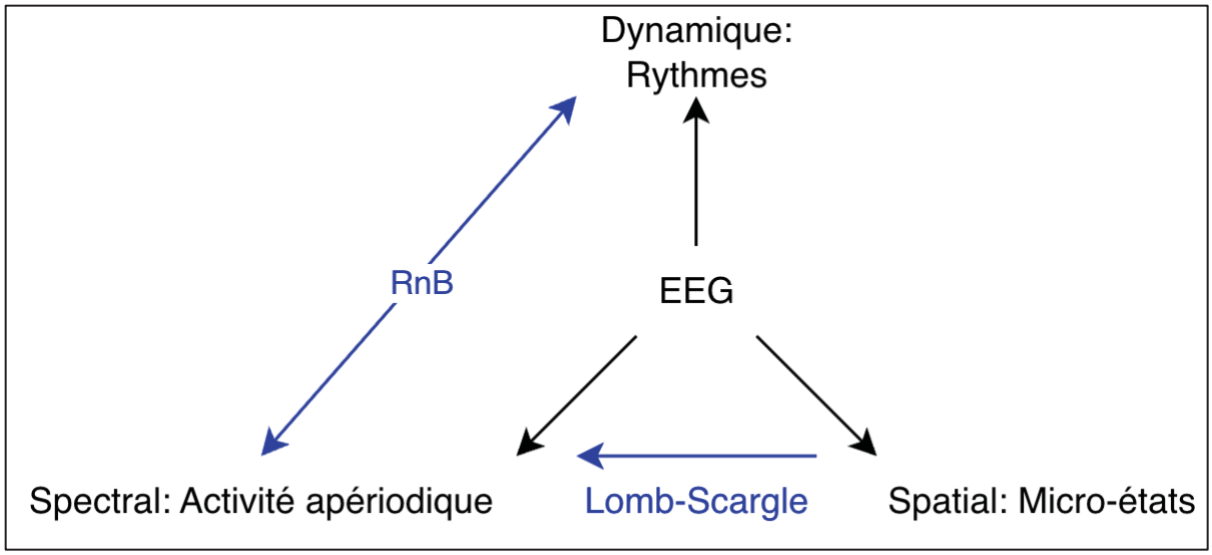

Figure 4.6 Outils numériques (en bleu) développés pour quantifier les signaux EEG : *RnB* permet de caractériser les activités rythmique et l'activité apériodique du signal EEG et Lomb–Scargle permet de mesurer l'activité apériodique des topographies des micro-états

Contribution 1 : Nous avons introduit la méthode de traitement du signal *RnB* basée sur la transformation par ondelettes fractionnaire, qui permet d'extraire un signal rythmique. En introduisant un estimateur en ondelettes qui tient compte de l'activité apériodique, cette méthodologie va au-delà des approches actuelles dans la littérature, qui se limitent au domaine spectral. Notons que, l'algorithme *RnB* généralise l'algorithme classique de « *shrinkage* » (Donoho & Johnstone, 1994), qui consiste à retenir les coefficients en ondelettes du signal EEG les plus forts. En effet, *RnB* tient compte de l'activité apériodique ($\beta \neq 0$) en introduisant un changement de base entre l'analyse et la synthèse en ondelettes afin de reconstruire correctement le signal rythmique. La famille d'ondelette fractionnaire dépend également d'un paramètre α arbitraire. On peut toutefois choisir une valeur de α qui demeure du même ordre de grandeur que β, afin que ce dernier ne soit pas négligé dans l'analyse par ondelette du signal.

Dans le contexte de l'EEG intracrânien, le signal rythmique extrait par l'algorithme *RnB* a été validé par l'analyse spectrale, la détection d'ondes lentes et l'évaluation du couplage phase-amplitude du delta et du sigma. Nous avons montré que les signaux rythmiques obtenus sont cohérents avec la neurophysiologie du sommeil, en montrant que la puissance spectrale du delta rythmique est plus élevée en NREM3 que NREM2 et que la puissance sigma rythmique

est plus élevée en NREM2 que NREM3. De plus, nous avons montré que le couplage $\delta - \sigma$ est plus élevé que celui observé dans les signaux EEG standards et que ce couplage augmente aussi lorsque les ondes thêta coïncident avec des ondes lentes rythmiques, par rapport aux périodes sans coïncidence. Ainsi, l'analyse du couplage est une application concrète où l'algorithme *RnB* pourrait être exploité dans un contexte clinique. En réduisant la présence d'activité apériodique, l'algorithme *RnB* met en évidence les rythmes en optimisant la quantification du couplage. On pourrait donc caractériser avec plus de précision les mécanismes neurophysiologiques et donc identifier des biomarqueurs cliniques plus robustes. En réduisant l'influence de la composante apériodique du signal, qui est hétérogène et interfère avec les rythmes, on devrait obtenir une meilleure discrimination entre cohortes cliniques, ainsi qu'une meilleure reproductibilité des résultats.

Il est important de noter que l'algorithme *RnB* filtre l'activité apériodique de façon ponctuelle sur des coefficients décorrélés. Ainsi, le calcul du couplage rythmique est effectué sur un signal produit par des coefficients qui ont été traités sur deux échelles différentes. Il est donc peu probable que les résultats du couplage soient associés à une activité rythmique produite par cette manipulation des coefficients par ondelettes. Toutefois, une façon de valider les résultats serait de « casser » la structure de phase du signal rythmique afin d'établir une valeur de couplage de référence. Si les résultats excèdent cette valeur de référence, le couplage peut être interprété comme étant associé à la physiologie, plutôt qu'un biais introduit par l'algorithme.

Une étude de Pulver et al. (2024) a utilisé des enregistrements EEG portatifs pour analyser les oscillations canoniques du sommeil impliquées dans la consolidation de la mémoire, soit les ondes lentes à transition rapide et lente (Bouchard et al., 2021). Cette classification des ondes lentes correspond à celle des « fast » et « slow switchers », étudiés dans *RnB* (chapitre 2). D'autre part, ces auteurs considèrent aussi les oscillations thêta et les fuseaux couplés à ces ondes lentes. L'objectif de ce travail était d'évaluer si la précision temporelle de ces couplages pouvait constituer un biomarqueur précoce de la maladie d'Alzheimer. À l'aide d'analyses temps–fréquence, les auteurs ont montré que l'organisation temporelle du couplage était

corrélée aux biomarqueurs habituels de la maladie d'Alzheimer, mettant en évidence une désorganisation de ce couplage chez des individus amyloïdes positifs. Ce travail suggère que cette altération constitue un biomarqueur de l'Alzheimer précoce. À noter que cette étude proposait des analyses similaires (ondes lentes) à celles réalisées avec l'algorithme *RnB* et s'inscrit donc dans une perspective qui rejoint directement celle proposée par *RnB*. L'application de *RnB* dans le contexte de cette étude permettrait d'obtenir un inventaire des rythmes, qui révélerait plus finement la désorganisation temporelle des couplages neuronaux et, potentiellement, permettrait d'obtenir des biomarqueurs plus robustes. On faciliterait ainsi leur intégration dans des protocoles cliniques de suivi longitudinal de l'Alzheimer précoce.

Contribution 2 : L'algorithme *RnB* a également été évalué sur l'EEG de scalp utilisé en contexte clinique. Le signal EEG de scalp présente un mélange plus complexe d'activités rythmique et apériodique, puisqu'une électrode mesure l'activité cérébrale des régions avoisinantes. Ceci a nécessité une modification de l'estimateur apériodique appliqué aux enregistrements intracrâniens.

Nous avons fait l'analyse spectrale des signaux rythmiques en évaluant les variations de puissance entre les stades du sommeil, ainsi que les effets du vieillissement. Nous avons ainsi révélé une dynamique qui diffère des approches standards de l'EEG quantitatif. De manière similaire aux résultats de *RnB* appliqués aux enregistrements intracrâniens, l'inventaire des rythmes sur le scalp concorde également avec la physiologie normale du sommeil, avec un delta rythmique plus élevé en NREM3 et un sigma rythmique plus élevé en NREM2. Cependant, les puissances rythmiques alpha et thêta présentaient des résultats plus difficiles à interpréter, car elles déviaient d'une diminution progressive attendue en sommeil de l'alpha et du thêta de NREM2 vers NREM3. Cela suggère que les bandes alpha et thêta sont plus sensibles à l'influence de la composante apériodique et que la dynamique entre les rythmes et l'activité apériodique présente une interférence plus difficile à interpréter. Nous avons aussi montré que le vieillissement est associé à des variations de puissances rythmiques plus faibles entre les stades du sommeil, contrairement aux jeunes, ce qui implique que le sommeil avec le vieillissement est moins flexible dans les transitions rythmiques.

Nous avons également détecté les fuseaux de sommeil, car ce sont des rythmes canoniques du sommeil NREM2 impliqués dans des processus importants tels que la consolidation de la mémoire. Nous avons détecté ces rythmes à l'aide de l'algorithme MP et avons montré que l'inventaire des rythmes avait une valeur physiologique. L'algorithme MP s'appuie sur un dictionnaire de fonctions pour caractériser les oscillations du signal. Chaque fuseau est défini par un cluster regroupant les fonctions (« atomes ») du dictionnaire présentant la corrélation la plus élevée avec le signal. L'algorithme ne repose pas sur des critères d'amplitude. L'amplitude du signal rythmique est inférieure à celle du signal EEG standard, car la composante apériodique est filtrée. Étant donné que l'algorithme MP ne s'appuie pas sur des critères d'amplitude, il est particulièrement adapté au signal rythmique, contrairement, par exemple, aux détecteurs classiques des ondes lentes qui reposent explicitement sur l'amplitude du signal EEG standard. De plus, en appliquant cet algorithme au signal standard et au signal rythmique, il serait possible de comparer le contenu des clusters obtenus. On pourrait faire l'hypothèse que le signal rythmique mettrait en évidence des clusters plus parcimonieux que ceux obtenus avec le signal standard. En tout, ce travail a montré que les signaux rythmiques du scalp présentent une nature physiologique et doivent permettre d'identifier des biomarqueurs fiables, applicables à des contextes cliniques, comme le montre l'étude de Pulver et al. (2024).

Finalement, étant donné que nous disposons d'un signal rythmique, une perspective de ce travail consisterait à localiser les sources rythmiques sur le maillage du cortex (fuseaux, ondes lentes). Cette étape consisterait à estimer l'activité cérébrale à partir d'un nombre limité d'électrodes, en résolvant un problème inverse *mal posé,* puisqu'on estime l'activité cérébrale dans un espace source (~10 000 sources) plus grand que l'espace des données (~100 électrodes). Puisque l'inventaire des rythmes déployés sur le scalp est mieux identifié lorsque l'activité apériodique est filtrée, cela pourrait réduire l'étalement spatial des générateurs corticaux et se traduire par des sources plus focales et mieux définies. Cela permettrait de caractériser plus précisément les mécanismes neuronaux de l'activité cérébrale rythmique dans le cadre de certaines pathologies. De plus, un signal rythmique sans interférence apériodique optimiserait également les analyses portant sur la synchronisation et la connectivité

fonctionnelle, afin d'identifier de façon plus robuste des réseaux altérés dans le contexte de pathologies en utilisant, par exemple, des métriques de cohérence spectrale.

Contribution 3 : Nous avons proposé l'analyse spectrale du GFP, associée à des séquences de micro-états, puis caractérisé l'activité apériodique des topographies de micro-états. L'analyse spectrale a été effectuée à l'aide de la méthode de Lomb-Scargle, permettant d'obtenir le contenu spectral de séquences échantillonnées irrégulièrement. Le GFP caractérise l'organisation temporelle de la synchronisation et de la désynchronisation de l'activité cérébrale à partir des topographies du scalp. Il fournit une mesure scalaire, soit l'écart-type des topographies du scalp, à partir de laquelle se manifeste, à grande échelle, la dynamique spatio-temporelle de l'activité cérébrale.

Nous avons montré que le GFP présente une structure invariante d'échelle. Ce comportement en $1/f^{\beta}$ du GFP peut être associé à des systèmes présentant une dynamique proche de la criticalité, un état à la frontière de l'ordre et du désordre, caractérisé par une invariance d'échelle permettant de traiter optimalement l'information (Beggs & Timme, 2012). Toutefois, l'invariance d'échelle n'implique pas nécessairement l'existence d'un état critique. L'invariance d'échelle observée du GFP corrobore également les simulations de Brake et al. (2024) qui montrent que l'invariance d'échelle peut résulter de la connectivité locale et potentiellement se manifester à grande échelle dans les dynamiques de l'activité cérébrale. Dans ce cadre, si l'on considère que le système dynamique et spatial de l'activité cérébrale est gouverné par des propriétés d'invariance d'échelle, alors le calcul de la pente spectrale β constitue un biomarqueur important, tant à l'échelle locale qu'à l'échelle globale. De plus, l'analyse spectrale du GFP des micro-états chez une cohorte de jeunes et de personnes âgées a montré que le sommeil des jeunes adultes est plus régulier que celui des personnes âgées, notamment pendant le sommeil profond. En effet, la pente spectrale des jeunes était plus élevée, ce qui est associé à des corrélations à longue portée plus fortes. Cela suggère que des changements neurophysiologiques de l'activité apériodique à grande échelle durant le sommeil auraient lieu au sein de différentes populations cliniques.

La continuité du travail pourrait porter sur la localisation des générateurs de chaque micro-état. Comme nous avons montré que les séquences du GFP des micro-états sont apériodiques, la localisation des générateurs du potentiel EEG de chaque micro-état serait spécifique à l'activité apériodique. Cela offrirait une description exhaustive de l'activité apériodique à grande échelle, avec l'obtention des générateurs de micro-états régis par une invariance d'échelle, ainsi que de la pente spectrale qui les caractérise. Étant donné l'hypothèse selon laquelle les générateurs des micro-états sont associés à des réseaux de connectivité (Britz et al., 2010), en plus de caractériser les altérations des réseaux en cas de pathologie, ce travail pourrait quantifier les variations de pente spectrales qui leur sont associées et caractériser l'organisation à longue portée associée aux réseaux d'une pathologie.

En conclusion, les outils développés dans cette thèse contribuent à une meilleure caractérisation des dynamiques rythmiques et apériodiques du cerveau pendant le sommeil. Ces outils numériques, dont certains font l'objet d'une propriété intellectuelle protégée par une déclaration d'invention, peuvent être appliqués dans des contextes cliniques, en offrant un inventaire plus précis des rythmes et une mesure de l'activité apériodique locale et à grande échelle.

ANNEXE I

ONDELETTE DE MORSE

L'ondelette de Morse (Lilly & Olhede, 2012) est définie dans le domaine de Fourier selon l'équation,

$$\widehat{\psi}(\omega) = CU(\omega)\omega^n e^{-\omega^m} \tag{A I.1}$$

La fonction $U(\omega)$ est la fonction de Heaviside. Le paramètre n contrôle la décroissance, tandis que le paramètre m contrôle plutôt la symétrie. La variable C est une constante de normalisation est définie par,

$$C = 2\left(\frac{em}{n}\right)^{\frac{n}{m}} \tag{A I.2}$$

Elle permet d'obtenir une amplitude de 2 à la fréquence de crête. La fréquence de crête est définie par,

$$\omega_{m,n} = \left(\frac{n}{m}\right)^{\frac{1}{m}} \tag{A I.3}$$

Ainsi,

$$\widehat{\psi}\left(\omega_{m,n}\right) = 2 \tag{A I.4}$$

Ceci permet de contrôler l'ondelette et d'établir une pour une certaine fréquence de crête. En modifiant les paramètres, m et n, la forme de l'ondelette de Morse est modifiée. L'ondellette devient plus étroite lorsque n et m augmentent. Lorsque n est petit et m est grand, l'ondellette est asymétrique et les propriétés de localisation sont moins efficaces.

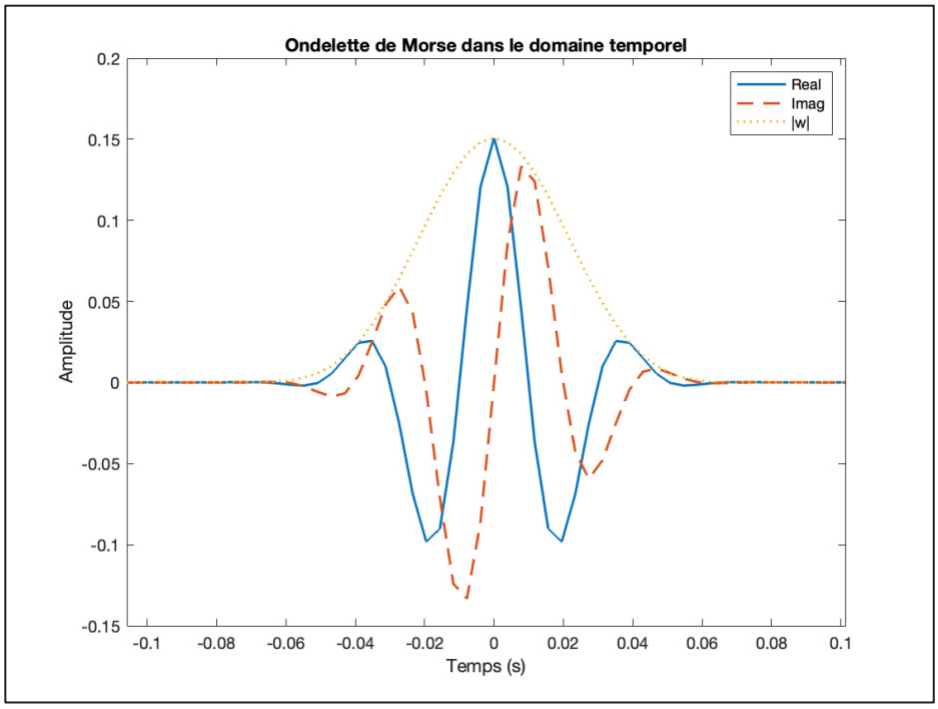

Figure-A I-1 Représentation de l'ondellette de Morse (n = 3, m = 10)

BIBLIOGRAPHIE

Abry, P., Wendt, H., Jaffard, S., & Didier, G. (2019). Multivariate scale-free temporal dynamics: From spectral (Fourier) to fractal (wavelet) analysis. *Comptes Rendus. Physique*, *20*(5), 489-501. https://doi.org/10.1016/j.crhy.2019.08.005

Al Zoubi, O., Mayeli, A., Tsuchiyagaito, A., Misaki, M., Zotev, V., Refai, H., … Victor, T. A. (2019). EEG Microstates Temporal Dynamics Differentiate Individuals with Mood and Anxiety Disorders From Healthy Subjects. *Frontiers in Human Neuroscience*, *13*. https://doi.org/10.3389/fnhum.2019.00056

Andrillon, T., Nir, Y., Staba, R. J., Ferrarelli, F., Cirelli, C., Tononi, G., & Fried, I. (2011). Sleep Spindles in Humans: Insights from Intracranial EEG and Unit Recordings. *Journal of Neuroscience*, *31*(49), 17821-17834. https://doi.org/10.1523/JNEUROSCI.2604-11.2011

Andrillon, T., Solelhac, G., Bouchequet, P., Romano, F., Le Brun, M.-P., Brigham, M., … Léger, D. (2020). Revisiting the value of polysomnographic data in insomnia: more than meets the eye. *Sleep Medicine*, *66*, 184-200. https://doi.org/10.1016/j.sleep.2019.12.002

Antony, J. W., Piloto, L., Wang, M., Pacheco, P., Norman, K. A., & Paller, K. A. (2018). Sleep Spindle Refractoriness Segregates Periods of Memory Reactivation. *Current Biology*, *28*(11), 1736-1743.e4. https://doi.org/10.1016/j.cub.2018.04.020

Aru, J., Aru, J., Priesemann, V., Wibral, M., Lana, L., Pipa, G., … Vicente, R. (2015). Untangling cross-frequency coupling in neuroscience. *Current Opinion in Neurobiology*, *31*, 51-61. https://doi.org/10.1016/j.conb.2014.08.002

Avvenuti, G., Handjaras, G., Betta, M., Cataldi, J., Imperatori, L. S., Lattanzi, S., … Bernardi, G. (2020). Integrity of Corpus Callosum Is Essential for the Cross-Hemispheric Propagation of Sleep Slow Waves: A High-Density EEG Study in Split-Brain Patients. *Journal of Neuroscience*, *40*(29), 5589-5603. https://doi.org/10.1523/JNEUROSCI.2571-19.2020

Babiloni, C., Binetti, G., Cassarino, A., Dal Forno, G., Del Percio, C., Ferreri, F., … Rossini, P. M. (2006). Sources of cortical rhythms in adults during physiological aging: a multicentric EEG study. *Human Brain Mapping*, *27*(2), 162-172. https://doi.org/10.1002/hbm.20175

Baillet, S., Mosher, J. C., & Leahy, R. M. (2001). Electromagnetic brain mapping. *IEEE Signal Processing Magazine*, *18*(6), 14-30. https://doi.org/10.1109/79.962275

Beggs, J. M., & Timme, N. (2012). Being Critical of Criticality in the Brain. *Frontiers in Physiology*, *3*. https://doi.org/10.3389/fphys.2012.00163

Beniczky, S., & Schomer, D. L. (2020). Electroencephalography: basic biophysical and technological aspects important for clinical applications. *Epileptic Disorders*, *22*(6), 697-715. https://doi.org/10.1684/epd.2020.1217

Blaskovich, B., Bullón-Tarrasó, E., Pöhlchen, D., Manafis, A., Neumayer, H., Besedovsky, L., … Spoormaker, V. I. (2024). The utility of wearable headband electroencephalography and pulse photoplethysmography to assess cortical and physiological arousal in individuals with stress-related mental disorders. *Journal of Sleep Research*, *33*(4), e14123. https://doi.org/10.1111/jsr.14123

Blu, T., & Unser, M. (2000). The fractional spline wavelet transform: definition end implementation. Dans *2000 IEEE International Conference on Acoustics, Speech, and Signal Processing. Proceedings (Cat. No.00CH37100)* (Vol. 1, pp. 512-515 vol.1). https://doi.org/10.1109/ICASSP.2000.862030

Blu, T., & Unser, M. (2003). A complete family of scaling functions: the (/spl alpha/, /spl tau/)-fractional splines. Dans *2003 IEEE International Conference on Acoustics, Speech, and Signal Processing, 2003. Proceedings. (ICASSP '03).* (Vol. 6, p. VI-421). https://doi.org/10.1109/ICASSP.2003.1201708

Bódizs, R., Szalárdy, O., Horváth, C., Ujma, P. P., Gombos, F., Simor, P., … Dresler, M. (2021). A set of composite, non-redundant EEG measures of NREM sleep based on the power law scaling of the Fourier spectrum. *Scientific Reports*, *11*(1), 2041. https://doi.org/10.1038/s41598-021-81230-7

Borbély, A. A., & Achermann, P. (1999). Sleep Homeostasis and Models of Sleep Regulation. *Journal of Biological Rhythms*, *14*(6), 559-570. https://doi.org/10.1177/074873099129000894

Borbély, A. A., Baumann, F., Brandeis, D., Strauch, I., & Lehmann, D. (1981). Sleep deprivation: Effect on sleep stages and EEG power density in man. *Electroencephalography and Clinical Neurophysiology*, *51*(5), 483-493. https://doi.org/10.1016/0013-4694(81)90225-X

Botella-Soler, V., Valderrama, M., Crépon, B., Navarro, V., & Quyen, M. L. V. (2012). Large-Scale Cortical Dynamics of Sleep Slow Waves. *PLOS ONE*, *7*(2), e30757. https://doi.org/10.1371/journal.pone.0030757

Bouchard, M., Lina, J.-M., Gaudreault, P.-O., Lafrenière, A., Dubé, J., Gosselin, N., & Carrier, J. (2021). Sleeping at the switch. *eLife*, *10*, e64337. https://doi.org/10.7554/eLife.64337

Brake, N., Duc, F., Rokos, A., Arseneau, F., Shahiri, S., Khadra, A., & Plourde, G. (2024). A neurophysiological basis for aperiodic EEG and the background spectral trend. *Nature Communications*, *15*(1), 1514. https://doi.org/10.1038/s41467-024-45922-8

Bréchet, L., Brunet, D., Perogamvros, L., Tononi, G., & Michel, C. M. (2020). EEG microstates of dreams. *Scientific Reports*, *10*(1), 17069. https://doi.org/10.1038/s41598-020-74075-z

Britz, J., Van De Ville, D., & Michel, C. M. (2010). BOLD correlates of EEG topography reveal rapid resting-state network dynamics. *NeuroImage*, *52*(4), 1162-1170. https://doi.org/10.1016/j.neuroimage.2010.02.052

Brodbeck, V., Kuhn, A., von Wegner, F., Morzelewski, A., Tagliazucchi, E., Borisov, S., … Laufs, H. (2012). EEG microstates of wakefulness and NREM sleep. *NeuroImage*, *62*(3), 2129-2139. https://doi.org/10.1016/j.neuroimage.2012.05.060

Buzsáki, G. (2004). Large-scale recording of neuronal ensembles. *Nature Neuroscience*, *7*(5), 446-451. https://doi.org/10.1038/nn1233

Buzsáki, G., & Draguhn, A. (2004). Neuronal Oscillations in Cortical Networks. *Science*, *304*(5679), 1926-1929. https://doi.org/10.1126/science.1099745

Carrier, J., Viens, I., Poirier, G., Robillard, R., Lafortune, M., Vandewalle, G., … Filipini, D. (2011). Sleep slow wave changes during the middle years of life. *European Journal of Neuroscience*, *33*(4), 758-766. https://doi.org/10.1111/j.1460-9568.2010.07543.x

Chen, Y., Liu, Y., Zhou, P., Zhang, X., Wu, Q., Zhao, X., & Ming, D. (2019). The Transitions Between Dynamic Micro-States Reveal Age-Related Functional Network Reorganization. *Frontiers in Physiology*, *9*. https://doi.org/10.3389/fphys.2018.01852

Churchill, N. W., Spring, R., Grady, C., Cimprich, B., Askren, M. K., Reuter-Lorenz, P. A., … Berman, M. G. (2016). The suppression of scale-free fMRI brain dynamics across three different sources of effort: aging, task novelty and task difficulty. *Scientific Reports*, *6*(1), 30895. https://doi.org/10.1038/srep30895

Chylinski, D., Van Egroo, M., Narbutas, J., Muto, V., Bahri, M. A., Berthomier, C., … Vandewalle, G. (2022). Timely coupling of sleep spindles and slow waves linked to early amyloid-β burden and predicts memory decline. *eLife*, *11*, e78191. https://doi.org/10.7554/eLife.78191

Coelho, J., Degros, H., Micoulaud-Franchi, J.-A., Sagaspe, P., d'Incau, E., Galvez, P., … Taillard, J. (2025). Threshold Values of Sleep Spindles Features in Healthy Adults Using Scalp-EEG and Associations With Sleep Parameters. *Annals of Clinical and Translational Neurology*, *12*(6), 1276-1291. https://doi.org/10.1002/acn3.70055

Cole, S., & Voytek, B. (2019). Cycle-by-cycle analysis of neural oscillations. *Journal of Neurophysiology*, *122*(2), 849-861. https://doi.org/10.1152/jn.00273.2019

Cox, R., Driel, J. van, Boer, M. de, & Talamini, L. M. (2014). Slow Oscillations during Sleep Coordinate Interregional Communication in Cortical Networks. *Journal of*

Neuroscience, *34*(50), 16890-16901. https://doi.org/10.1523/JNEUROSCI.1953-14.2014

Cox, R., Mylonas, D. S., Manoach, D. S., & Stickgold, R. (2018). Large-scale structure and individual fingerprints of locally coupled sleep oscillations. *Sleep*, *41*(12), zsy175. https://doi.org/10.1093/sleep/zsy175

Cox, R., Rüber, T., Staresina, B. P., & Fell, J. (2019). Heterogeneous profiles of coupled sleep oscillations in human hippocampus. *NeuroImage*, *202*, 116178. https://doi.org/10.1016/j.neuroimage.2019.116178

Cox, R., Rüber, T., Staresina, B. P., & Fell, J. (2020). Phase-based coordination of hippocampal and neocortical oscillations during human sleep. *Communications Biology*, *3*(1), 176. https://doi.org/10.1038/s42003-020-0913-5

Croce, P., Quercia, A., Costa, S., & Zappasodi, F. (2020). EEG microstates associated with intra- and inter-subject alpha variability. *Scientific Reports*, *10*(1), 2469. https://doi.org/10.1038/s41598-020-58787-w

Custo, A., Van De Ville, D., Wells, W. M., Tomescu, M. I., Brunet, D., & Michel, C. M. (2017). Electroencephalographic Resting-State Networks: Source Localization of Microstates. *Brain Connectivity*, *7*(10), 671-682. https://doi.org/10.1089/brain.2016.0476

Czeisler, C. A., & Gooley, J. J. (2007). Sleep and Circadian Rhythms in Humans. *Cold Spring Harbor Symposia on Quantitative Biology*, *72*, 579-597. https://doi.org/10.1101/sqb.2007.72.064

Dang-Vu, T. T., Salimi, A., Boucetta, S., Wenzel, K., O'Byrne, J., Brandewinder, M., … Gouin, J.-P. (2015). Sleep Spindles Predict Stress-Related Increases in Sleep Disturbances. *Frontiers in Human Neuroscience*, *9*. https://doi.org/10.3389/fnhum.2015.00068

Daubechies, I. (1988). Orthonormal bases of compactly supported wavelets. *Communications on Pure and Applied Mathematics*, *41*(7), 909-996. https://doi.org/10.1002/cpa.3160410705

De Gennaro, L., & Ferrara, M. (2003). Sleep spindles: an overview. *Sleep Medicine Reviews*, *7*(5), 423-440. https://doi.org/10.1053/smrv.2002.0252

Dijk, D. J., Beersma, D. G. M., & van den Hoofdakker, R. H. (1989). All night spectral analysis of EEG sleep in young adult and middle-aged male subjects. *Neurobiology of Aging*, *10*(6), 677-682. https://doi.org/10.1016/0197-4580(89)90004-3

Donoghue, T. (2025). A Systematic Review of Aperiodic Neural Activity in Clinical Investigations. *European Journal of Neuroscience*, *62*(7), e70255. https://doi.org/10.1111/ejn.70255

Donoghue, T., Haller, M., Peterson, E. J., Varma, P., Sebastian, P., Gao, R., … Voytek, B. (2020). Parameterizing neural power spectra into periodic and aperiodic components. *Nature Neuroscience*, *23*(12), 1655-1665. https://doi.org/10.1038/s41593-020-00744-x

Donoghue, T., Schaworonkow, N., & Voytek, B. (2022). Methodological considerations for studying neural oscillations. *European Journal of Neuroscience*, *55*(11-12), 3502-3527. https://doi.org/10.1111/ejn.15361

Donoho, D. L., & Johnstone, I. M. (1994). Ideal spatial adaptation by wavelet shrinkage. *Biometrika*, *81*(3), 425-455. https://doi.org/10.1093/biomet/81.3.425

Dubé, J., Foti, M., Jaffard, S., Latreille, V., Frauscher, B., Carrier, J., & Lina, J. M. (2024, 17 novembre). Rhythms and Background (RnB): The Spectroscopy of Sleep Recordings. bioRxiv. https://doi.org/10.1101/2024.10.28.620621

Durka, P., Dovgialo, M., Duszyk-Bogorodzka, A., & Biegański, P. (2024). Two-Stage Atomic Decomposition of Multichannel EEG and the Previously Undetectable Sleep Spindles. *Sensors*, *24*(3), 842. https://doi.org/10.3390/s24030842

Durka, P. J., & Blinowska, K. J. (1995). Analysis of EEG transients by means of matching pursuit. *Annals of Biomedical Engineering*, *23*(5), 608-611. https://doi.org/10.1007/BF02584459

Engel, J. J. (2014). Approaches to refractory epilepsy. *Annals of Indian Academy of Neurology*, *17*(Suppl 1), S12. https://doi.org/10.4103/0972-2327.128644

Fama, R., & Sullivan, E. V. (2015). Thalamic structures and associated cognitive functions: Relations with age and aging. *Neuroscience & Biobehavioral Reviews*, *54*, 29-37. https://doi.org/10.1016/j.neubiorev.2015.03.008

Farrokhi, A., & Daliri, M. R. (2022). PAIMD: A Novel Data-Driven Decomposition Method for Separating Neural Signal Into Periodic and Aperiodic Components. *IEEE Access*, *10*, 130572-130585. https://doi.org/10.1109/ACCESS.2022.3226259

Favaro, J., Colombo, M. A., Mikulan, E., Sartori, S., Nosadini, M., Pelizza, M. F., … Toldo, I. (2023). The maturation of aperiodic EEG activity across development reveals a progressive differentiation of wakefulness from sleep. *NeuroImage*, *277*, 120264. https://doi.org/10.1016/j.neuroimage.2023.120264

Fernandez, L. M. J., & Luthi, A. (2019). Sleep Spindles: Mechanisms and Functions. *Physiological Reviews*. https://doi.org/10.1152/physrev.00042.2018

Ferrarelli, F., Peterson, M. J., Sarasso, S., Riedner, B. A., Murphy, M. J., Benca, R. M., … Tononi, G. (2010). Thalamic Dysfunction in Schizophrenia Suggested by Whole-Night Deficits in Slow and Fast Spindles. *American Journal of Psychiatry*. https://doi.org/10.1176/appi.ajp.2010.09121731

Finley, A. J., Angus, D. J., Knight, E. L., Reekum, C. M. van, Lachman, M. E., Davidson, R. J., & Schaefer, S. M. (2024). Resting EEG Periodic and Aperiodic Components Predict Cognitive Decline Over 10 Years. *Journal of Neuroscience*, *44*(13). https://doi.org/10.1523/JNEUROSCI.1332-23.2024

Frelih, T., Matkovič, A., Mlinarič, T., Bon, J., & Repovš, G. (2025). Modulation of aperiodic EEG activity provides sensitive index of cognitive state changes during working memory task. *eLife*, *13*. https://doi.org/10.7554/eLife.101071.3

Gais, S., Mölle, M., Helms, K., & Born, J. (2002). Learning-Dependent Increases in Sleep Spindle Density. *Journal of Neuroscience*, *22*(15), 6830-6834. https://doi.org/10.1523/JNEUROSCI.22-15-06830.2002

Gao, R. (2016). Interpreting the electrophysiological power spectrum. *Journal of Neurophysiology*, *115*(2), 628-630. https://doi.org/10.1152/jn.00722.2015

Gao, R., Peterson, E. J., & Voytek, B. (2017). Inferring synaptic excitation/inhibition balance from field potentials. *NeuroImage*, *158*, 70-78. https://doi.org/10.1016/j.neuroimage.2017.06.078

Garcia-Rill, E., D'Onofrio, S., Luster, B., Mahaffey, S., Urbano, F., & Phillips, C. (2016). The 10 Hz frequency: A fulcrum for transitional brain states. *Translational Brain Rhythmicity*, *1*(1). https://doi.org/10.15761/TBR.1000103

Gerster, M., Waterstraat, G., Litvak, V., Lehnertz, K., Schnitzler, A., Florin, E., … Nikulin, V. (2022). Separating Neural Oscillations from Aperiodic 1/f Activity: Challenges and Recommendations. *Neuroinformatics*, *20*(4), 991-1012. https://doi.org/10.1007/s12021-022-09581-8

Gonzalez, C. E., Mak-McCully, R. A., Rosen, B. Q., Cash, S. S., Chauvel, P. Y., Bastuji, H., … Halgren, E. (2018). Theta Bursts Precede, and Spindles Follow, Cortical and Thalamic Downstates in Human NREM Sleep. *Journal of Neuroscience*, *38*(46), 9989-10001. https://doi.org/10.1523/JNEUROSCI.0476-18.2018

Hafkemeijer, A., van der Grond, J., & Rombouts, S. A. R. B. (2012). Imaging the default mode network in aging and dementia. *Biochimica et Biophysica Acta (BBA) - Molecular Basis of Disease*, *1822*(3), 431-441. https://doi.org/10.1016/j.bbadis.2011.07.008

Hahn, G., Bujan, A. F., Frégnac, Y., Aertsen, A., & Kumar, A. (2014). Communication through Resonance in Spiking Neuronal Networks. *PLOS Computational Biology*, *10*(8), e1003811. https://doi.org/10.1371/journal.pcbi.1003811

Hassainia, F., Petit, D., Nielsen, T., & Gauthier, S. (2008). Quantitative EEG and Statistical Mapping of Wakefulness and REM Sleep in the Evaluation of Mild to Moderate Alzheimer's Disease. *European Neurology*, *37*(4), 219-224. https://doi.org/10.1159/000117446

Hay, Y. A., Deperrois, N., Fuchsberger, T., Quarrell, T. M., Koerling, A.-L., & Paulsen, O. (2021). Thalamus mediates neocortical Down state transition via GABAB-receptor-targeting interneurons. *Neuron*, *109*(17), 2682-2690.e5. https://doi.org/10.1016/j.neuron.2021.06.030

He, B. J. (2014). Scale-free brain activity: past, present, and future. *Trends in Cognitive Sciences*, *18*(9), 480-487. https://doi.org/10.1016/j.tics.2014.04.003

He, B. J., Zempel, J. M., Snyder, A. Z., & Raichle, M. E. (2010). The Temporal Structures and Functional Significance of Scale-free Brain Activity. *Neuron*, *66*(3), 353-369. https://doi.org/10.1016/j.neuron.2010.04.020

Heckner, M. K., Cieslik, E. C., Eickhoff, S. B., Camilleri, J. A., Hoffstaedter, F., & Langner, R. (2021). The Aging Brain and Executive Functions Revisited: Implications from Meta-analytic and Functional-Connectivity Evidence. *Journal of Cognitive Neuroscience*, *33*(9), 1716-1752. https://doi.org/10.1162/jocn_a_01616

Helfrich, R. F., Lendner, J. D., & Knight, R. T. (2021). Aperiodic sleep networks promote memory consolidation. *Trends in Cognitive Sciences*, *25*(8), 648-659. https://doi.org/10.1016/j.tics.2021.04.009

Helfrich, R. F., Lendner, J. D., Mander, B. A., Guillen, H., Paff, M., Mnatsakanyan, L., … Knight, R. T. (2019). Bidirectional prefrontal-hippocampal dynamics organize information transfer during sleep in humans. *Nature Communications*, *10*(1), 3572. https://doi.org/10.1038/s41467-019-11444-x

Helfrich, R. F., Mander, B. A., Jagust, W. J., Knight, R. T., & Walker, M. P. (2018). Old Brains Come Uncoupled in Sleep: Slow Wave-Spindle Synchrony, Brain Atrophy, and Forgetting. *Neuron*, *97*(1), 221-230.e4. https://doi.org/10.1016/j.neuron.2017.11.020

Hernandez, J., Lina, J.-M., Dubé, J., Lafrenière, A., Gagnon, J.-F., Montplaisir, J.-Y., … Carrier, J. (2024). Electroencephalogram rhythmic and arrhythmic spectral components and functional connectivity at resting state may predict the development of synucleinopathies in idiopathic rapid eye movement sleep behavior disorder. *Sleep*, *47*(12), zsae074. https://doi.org/10.1093/sleep/zsae074

Höhn, C., Hahn, M. A., Lendner, J. D., & Hoedlmoser, K. (2024). Spectral Slope and Lempel–Ziv Complexity as Robust Markers of Brain States during Sleep and Wakefulness. *eNeuro*, *11*(3). https://doi.org/10.1523/ENEURO.0259-23.2024

Horváth, C., Szalárdy, O., Ujma, P. P., Simor, P., Gombos, F., Kovács, I., … Bódizs, R. (2022). Overnight dynamics in scale-free and oscillatory spectral parameters of NREM sleep EEG. *Scientific Reports*, *12*(1), 18409. https://doi.org/10.1038/s41598-022-23033-y

Iber, C., Ancoli-Israel, S., Chesson, A., & Quan, S. F. (2007). The AASM Manual for the Scoring of Sleep and Associated Events: Rules, Terminology, and Technical Specification. Repéré à https://cir.nii.ac.jp/crid/1370004237604151044

Jabès, A., Klencklen, G., Ruggeri, P., Michel, C. M., Banta Lavenex, P., & Lavenex, P. (2021). Resting-State EEG Microstates Parallel Age-Related Differences in Allocentric Spatial Working Memory Performance. *Brain Topography*, *34*(4), 442-460. https://doi.org/10.1007/s10548-021-00835-3

Jaffard, S., Lashermes, B., & Abry, P. (2007). Wavelet Leaders in Multifractal Analysis. Dans T. Qian, M. I. Vai, & Y. Xu (Éds), *Wavelet Analysis and Applications* (pp. 201-246). Basel : Birkhäuser. https://doi.org/10.1007/978-3-7643-7778-6_17

Jansen, B. H., & Rit, V. G. (1995). Electroencephalogram and visual evoked potential generation in a mathematical model of coupled cortical columns. *Biological Cybernetics*, *73*(4), 357-366. https://doi.org/10.1007/BF00199471

Javed, E., Croce, P., Zappasodi, F., & Gratta, C. D. (2019). Hilbert spectral analysis of EEG data reveals spectral dynamics associated with microstates. *Journal of Neuroscience Methods*, *325*, 108317. https://doi.org/10.1016/j.jneumeth.2019.108317

Jensen, O., Kaiser, J., & Lachaux, J.-P. (2007). Human gamma-frequency oscillations associated with attention and memory. *Trends in Neurosciences*, *30*(7), 317-324. https://doi.org/10.1016/j.tins.2007.05.001

Jiang, X., Gonzalez-Martinez, J., & Halgren, E. (2019). Posterior Hippocampal Spindle Ripples Co-occur with Neocortical Theta Bursts and Downstates-Upstates, and Phase-Lock with Parietal Spindles during NREM Sleep in Humans. *Journal of Neuroscience*, *39*(45), 8949-8968. https://doi.org/10.1523/JNEUROSCI.2858-18.2019

Jurkiewicz, G. J., Hunt, M. J., & Żygierewicz, J. (2021). Addressing Pitfalls in Phase-Amplitude Coupling Analysis with an Extended Modulation Index Toolbox. *Neuroinformatics*, *19*(2), 319-345. https://doi.org/10.1007/s12021-020-09487-3

Kashihara, S., Asai, T., & Imamizu, H. (2025). Topographical polarity reveals continuous EEG microstate transitions and electric field direction in healthy aging. *Cerebral Cortex*, *35*(8), bhaf214. https://doi.org/10.1093/cercor/bhaf214

Khanna, A., Pascual-Leone, A., Michel, C. M., & Farzan, F. (2015). Microstates in resting-state EEG: Current status and future directions. *Neuroscience & Biobehavioral Reviews*, *49*, 105-113. https://doi.org/10.1016/j.neubiorev.2014.12.010

Kleinert, T., Koenig, T., Nash, K., & Wascher, E. (2024). On the Reliability of the EEG Microstate Approach. *Brain Topography*, *37*(2), 271-286. https://doi.org/10.1007/s10548-023-00982-9

Klinzing, J. G., Mölle, M., Weber, F., Supp, G., Hipp, J. F., Engel, A. K., & Born, J. (2016). Spindle activity phase-locked to sleep slow oscillations. *NeuroImage*, *134*, 607-616. https://doi.org/10.1016/j.neuroimage.2016.04.031

Koenig, T., Lehmann, D., Merlo, M. C. G., Kochi, K., Hell, D., & Koukkou, M. (1999). A deviant EEG brain microstate in acute, neuroleptic-naive schizophrenics at rest. *European Archives of Psychiatry and Clinical Neuroscience*, *249*(4), 205-211. https://doi.org/10.1007/s004060050088

Koenig, Thomas, Diezig, S., Kalburgi, S. N., Antonova, E., Artoni, F., Brechet, L., … Michel, C. M. (2024). EEG-Meta-Microstates: Towards a More Objective Use of Resting-State EEG Microstate Findings Across Studies. *Brain Topography*, *37*(2), 218-231. https://doi.org/10.1007/s10548-023-00993-6

Koenig, Thomas, Prichep, L., Lehmann, D., Sosa, P. V., Braeker, E., Kleinlogel, H., … John, E. R. (2002). Millisecond by Millisecond, Year by Year: Normative EEG Microstates and Developmental Stages. *NeuroImage*, *16*(1), 41-48. https://doi.org/10.1006/nimg.2002.1070

Kozhemiako, N., Mylonas, D., Pan, J. Q., Prerau, M. J., Redline, S., & Purcell, S. M. (2022). Sources of Variation in the Spectral Slope of the Sleep EEG. *eNeuro*, *9*(5). https://doi.org/10.1523/ENEURO.0094-22.2022

Krstulovic, S., & Gribonval, R. (2006). Mptk: Matching Pursuit Made Tractable. Dans *2006 IEEE International Conference on Acoustics Speech and Signal Processing Proceedings* (Vol. 3, p. III-III). https://doi.org/10.1109/ICASSP.2006.1660699

Kuhn, A., Brodbeck, V., Tagliazucchi, E., Morzelewski, A., von Wegner, F., & Laufs, H. (2015). Narcoleptic Patients Show Fragmented EEG-Microstructure During Early NREM Sleep. *Brain Topography*, *28*(4), 619-635. https://doi.org/10.1007/s10548-014-0387-1

Kumral, D., Matzerath, A., Leonhart, R., & Schönauer, M. (2023). Spindle-dependent memory consolidation in healthy adults: A meta-analysis. *Neuropsychologia*, *189*, 108661. https://doi.org/10.1016/j.neuropsychologia.2023.108661

Lambert, I., Roehri, N., Fayerstein, J., Giusiano, B., Colombet, B., Bénar, C.-G., & Bartolomei, F. (2022). Cortico-cortical and thalamo-cortical connectivity during non-REM and REM sleep: Insights from intracranial recordings in humans. *Clinical Neurophysiology*, *143*, 84-94. https://doi.org/10.1016/j.clinph.2022.08.026

Landolt, H.-P., & Borbély, A. A. (2001). Age-dependent changes in sleep EEG topography. *Clinical Neurophysiology*, *112*(2), 369-377. https://doi.org/10.1016/S1388-2457(00)00542-3

Latreille, V., Gaubert, M., Dubé, J., Lina, J.-M., Gagnon, J.-F., & Carrier, J. (2019). Age-related cortical signatures of human sleep electroencephalography. *Neurobiology of Aging*, *76*, 106-114. https://doi.org/10.1016/j.neurobiolaging.2018.12.012

Léger, D., Debellemaniere, E., Rabat, A., Bayon, V., Benchenane, K., & Chennaoui, M. (2018). Slow-wave sleep: From the cell to the clinic. *Sleep Medicine Reviews*, *41*, 113-132. https://doi.org/10.1016/j.smrv.2018.01.008

Lehmann, D., Ozaki, H., & Pal, I. (1987). EEG alpha map series: brain micro-states by space-oriented adaptive segmentation. *Electroencephalography and Clinical Neurophysiology*, *67*(3), 271-288. https://doi.org/10.1016/0013-4694(87)90025-3

Lehmann, Dietrich, Faber, P. L., Galderisi, S., Herrmann, W. M., Kinoshita, T., Koukkou, M., … Koenig, T. (2005). EEG microstate duration and syntax in acute, medication-naïve, first-episode schizophrenia: a multi-center study. *Psychiatry Research: Neuroimaging*, *138*(2), 141-156. https://doi.org/10.1016/j.pscychresns.2004.05.007

Lendner, J. D., Helfrich, R. F., Mander, B. A., Romundstad, L., Lin, J. J., Walker, M. P., … Knight, R. T. (2020). An electrophysiological marker of arousal level in humans. *eLife*, *9*, e55092. https://doi.org/10.7554/eLife.55092

Lendner, J. D., Niethard, N., Mander, B. A., van Schalkwijk, F. J., Schuh-Hofer, S., Schmidt, H., … Helfrich, R. F. (2023). Human REM sleep recalibrates neural activity in support of memory formation. *Science Advances*, *9*(34), eadj1895. https://doi.org/10.1126/sciadv.adj1895

Li, Y., Shi, W., Liu, Z., Li, J., Wang, Q., Yan, X., … Wang, G. (2021). Effective Brain State Estimation During Propofol-Induced Sedation Using Advanced EEG Microstate Spectral Analysis. *IEEE Journal of Biomedical and Health Informatics*, *25*(4), 978-987. https://doi.org/10.1109/JBHI.2020.3008052

Lilly, J. M., & Olhede, S. C. (2012). Generalized Morse Wavelets as a Superfamily of Analytic Wavelets. *IEEE Transactions on Signal Processing*, *60*(11), 6036-6041. https://doi.org/10.1109/TSP.2012.2210890

Lina, J.-M., O'Callaghan, E. K., & Mongrain, V. (2019). Scale-Free Dynamics of the Mouse Wakefulness and Sleep Electroencephalogram Quantified Using Wavelet-Leaders. *Clocks & Sleep*, *1*(1), 50-64. https://doi.org/10.3390/clockssleep1010006

Lopes, R., & Betrouni, N. (2009). Fractal and multifractal analysis: A review. *Medical Image Analysis*, *13*(4), 634-649. https://doi.org/10.1016/j.media.2009.05.003

Ludwig, P. E., Reddy, V., & Varacallo, M. A. (2025). Neuroanatomy, Neurons. Dans *StatPearls*. Treasure Island (FL) : StatPearls Publishing. Repéré à http://www.ncbi.nlm.nih.gov/books/NBK441977/

Luo, W., & Guan, J.-S. (2018). Do Brain Oscillations Orchestrate Memory? *Brain Science Advances*, *4*(1), 16-33. https://doi.org/10.26599/BSA.2018.9050008

Lupi, E., Antonio, G. D., Angiolelli, M., Sacha, M., Kayabas, M. A., Alboré, N., … Fousek, J. (2024). A Whole-Brain Model of the Aging Brain During Slow Wave Sleep. *eNeuro*, *11*(11). https://doi.org/10.1523/ENEURO.0180-24.2024

Mallat, S. (2009). *A wavelet tour of signal processing: the sparse way* (3rd ed). Amsterdam Boston : Elsevier/Academic Press.

Mallat, S. G. (1989). A theory for multiresolution signal decomposition: the wavelet representation. *IEEE Transactions on Pattern Analysis and Machine Intelligence*, *11*(7), 674-693. https://doi.org/10.1109/34.192463

Mallat, S. G., & Zhang, Z. (1993). Matching pursuits with time-frequency dictionaries. *IEEE Transactions on Signal Processing*, *41*(12), 3397-3415. https://doi.org/10.1109/78.258082

Mander, B. A., Zhu, A. H., Lindquist, J. R., Villeneuve, S., Rao, V., Lu, B., … Walker, M. P. (2017). White Matter Structure in Older Adults Moderates the Benefit of Sleep Spindles on Motor Memory Consolidation. *Journal of Neuroscience*, *37*(48), 11675-11687. https://doi.org/10.1523/JNEUROSCI.3033-16.2017

Marshall, L., Helgadóttir, H., Mölle, M., & Born, J. (2006). Boosting slow oscillations during sleep potentiates memory. *Nature*, *444*(7119), 610-613. https://doi.org/10.1038/nature05278

Martin, N., Lafortune, M., Godbout, J., Barakat, M., Robillard, R., Poirier, G., … Carrier, J. (2013). Topography of age-related changes in sleep spindles. *Neurobiology of Aging*, *34*(2), 468-476. https://doi.org/10.1016/j.neurobiolaging.2012.05.020

Massimini, M., Huber, R., Ferrarelli, F., Hill, S., & Tononi, G. (2004). The Sleep Slow Oscillation as a Traveling Wave. *Journal of Neuroscience*, *24*(31), 6862-6870. https://doi.org/10.1523/JNEUROSCI.1318-04.2004

McConnell, B. V., Kronberg, E., Teale, P. D., Sillau, S. H., Fishback, G. M., Kaplan, R. I., … Bettcher, B. M. (2021). The aging slow wave: a shifting amalgam of distinct slow wave and spindle coupling subtypes define slow wave sleep across the human lifespan. *Sleep*, *44*(10), zsab125. https://doi.org/10.1093/sleep/zsab125

McFarlane, J. M. (2024). Sleep and Why We Need Sleep. Repéré à https://opentextbc.ca/psychologymtdi/chapter/sleep-and-why-we-need-sleep/

Michel, C. M., & Koenig, T. (2018). EEG microstates as a tool for studying the temporal dynamics of whole-brain neuronal networks: A review. *NeuroImage*, *180*, 577-593. https://doi.org/10.1016/j.neuroimage.2017.11.062

Milz, P., Pascual-Marqui, R. D., Achermann, P., Kochi, K., & Faber, P. L. (2017). The EEG microstate topography is predominantly determined by intracortical sources in the alpha band. *NeuroImage*, *162*, 353-361. https://doi.org/10.1016/j.neuroimage.2017.08.058

Muehlroth, B. E., & Werkle-Bergner, M. (2020). Understanding the interplay of sleep and aging: Methodological challenges. *Psychophysiology*, *57*(3), e13523. https://doi.org/10.1111/psyp.13523

Murphy, M., Riedner, B. A., Huber, R., Massimini, M., Ferrarelli, F., & Tononi, G. (2009). Source modeling sleep slow waves. *Proceedings of the National Academy of Sciences*, *106*(5), 1608-1613. https://doi.org/10.1073/pnas.0807933106

Nagabhushan Kalburgi, S., Kleinert, T., Aryan, D., Nash, K., Schiller, B., & Koenig, T. (2024). MICROSTATELAB: The EEGLAB Toolbox for Resting-State Microstate Analysis. *Brain Topography*, *37*(4), 621-645. https://doi.org/10.1007/s10548-023-01003-5

Niethard, N., Brodt, S., & Born, J. (2021). Cell-Type-Specific Dynamics of Calcium Activity in Cortical Circuits over the Course of Slow-Wave Sleep and Rapid Eye Movement Sleep. *Journal of Neuroscience*, *41*(19), 4212-4222. https://doi.org/10.1523/JNEUROSCI.1957-20.2021

O'Byrne, J., & Jerbi, K. (2022). How critical is brain criticality? *Trends in Neurosciences*, *45*(11), 820-837. https://doi.org/10.1016/j.tins.2022.08.007

O'Reilly, C., Gosselin, N., Carrier, J., & Nielsen, T. (2014). Montreal Archive of Sleep Studies: an open-access resource for instrument benchmarking and exploratory research. *Journal of Sleep Research*, *23*(6), 628-635. https://doi.org/10.1111/jsr.12169

Ostlund, B., Donoghue, T., Anaya, B., Gunther, K. E., Karalunas, S. L., Voytek, B., & Pérez-Edgar, K. E. (2022). Spectral parameterization for studying neurodevelopment: How and why. *Developmental Cognitive Neuroscience*, *54*, 101073. https://doi.org/10.1016/j.dcn.2022.101073

Pani, S., Fraschini, M., Figorilli, M., Tamburrino, L., Ferri, R., & Puligheddu, M. (2021). Sleep-related hypermotor epilepsy and non-rapid eye movement parasomnias: Differences in the periodic and aperiodic component of the electroencephalographic power spectra. *Journal of Sleep Research*, *30*(5), e13339. https://doi.org/10.1111/jsr.13339

Pani, S. M., Saba, L., & Fraschini, M. (2022). Clinical applications of EEG power spectra aperiodic component analysis: A mini-review. *Clinical Neurophysiology*, *143*, 1-13. https://doi.org/10.1016/j.clinph.2022.08.010

Pascual-Marqui, R. D., Lehmann, D., Faber, P., Milz, P., Kochi, K., Yoshimura, M., … Kinoshita, T. (2014, 15 novembre). The resting microstate networks (RMN): cortical

distributions, dynamics, and frequency specific information flow. arXiv. https://doi.org/10.48550/arXiv.1411.1949

Patel, A. K., Reddy, V., Shumway, K. R., & Araujo, J. F. (2025). Physiology, Sleep Stages. Dans *StatPearls*. Treasure Island (FL) : StatPearls Publishing. Repéré à http://www.ncbi.nlm.nih.gov/books/NBK526132/

Peterson, E. J., Rosen, B. Q., Belger, A., Voytek, B., & Campbell, A. M. (2023). Aperiodic Neural Activity is a Better Predictor of Schizophrenia than Neural Oscillations. *Clinical EEG and Neuroscience*, *54*(4), 434-445. https://doi.org/10.1177/15500594231165589

Pinotsis, D. A., Moran, R. J., & Friston, K. J. (2012). Dynamic causal modeling with neural fields. *NeuroImage*, *59*(2), 1261-1274. https://doi.org/10.1016/j.neuroimage.2011.08.020

Pulver, R. L., Kronberg, E., Medenblik, L. M., Kheyfets, V. O., Ramos, A. R., Holtzman, D. M., … McConnell, B. V. (2024). Mapping sleep's oscillatory events as a biomarker of Alzheimer's disease. *Alzheimer's & Dementia*, *20*(1), 301-315. https://doi.org/10.1002/alz.13420

Purcell, S. M., Manoach, D. S., Demanuele, C., Cade, B. E., Mariani, S., Cox, R., … Stickgold, R. (2017). Characterizing sleep spindles in 11,630 individuals from the National Sleep Research Resource. *Nature Communications*, *8*(1), 15930. https://doi.org/10.1038/ncomms15930

Raichle, M. E. (2015). The Brain's Default Mode Network. *Annual Review of Neuroscience*, *38*(Volume 38, 2015), 433-447. https://doi.org/10.1146/annurev-neuro-071013-014030

Rasch, B., & Born, J. (2013). About Sleep's Role in Memory. *Physiological Reviews*, *93*(2), 681-766. https://doi.org/10.1152/physrev.00032.2012

Raymond, G. M., & Bassingthwaighte, J. B. (1999). Deriving dispersional and scaled windowed variance analyses using the correlation function of discrete fractional Gaussian noise. *Physica A: Statistical Mechanics and its Applications*, *265*(1), 85-96. https://doi.org/10.1016/S0378-4371(98)00479-8

Rosenblum, Y., Bogdány, T., Nádasy, L. B., Chen, X., Kovács, I., Gombos, F., … Dresler, M. (2025). Aperiodic neural activity distinguishes between phasic and tonic REM sleep. *Journal of Sleep Research*, *34*(4), e14439. https://doi.org/10.1111/jsr.14439

Rosenblum, Y., Bovy, L., Weber, F. D., Steiger, A., Zeising, M., & Dresler, M. (2023). Increased Aperiodic Neural Activity During Sleep in Major Depressive Disorder. *Biological Psychiatry Global Open Science*, *3*(4), 1021-1029. https://doi.org/10.1016/j.bpsgos.2022.10.001

Rosenblum, Y., Jafarzadeh Esfahani, M., Adelhöfer, N., Zerr, P., Furrer, M., Huber, R., … Dresler, M. (2025). Fractal cycles of sleep, a new aperiodic activity-based definition of sleep cycles. *eLife*, *13*, RP96784. https://doi.org/10.7554/eLife.96784

Samaha, J., & Cohen, M. X. (2022). Power spectrum slope confounds estimation of instantaneous oscillatory frequency. *NeuroImage*, *250*, 118929. https://doi.org/10.1016/j.neuroimage.2022.118929

Scally, B., Burke, M. R., Bunce, D., & Delvenne, J.-F. (2018). Resting-state EEG power and connectivity are associated with alpha peak frequency slowing in healthy aging. *Neurobiology of Aging*, *71*, 149-155. https://doi.org/10.1016/j.neurobiolaging.2018.07.004

Scargle, J. D. (1982). Studies in astronomical time series analysis. II. Statistical aspects of spectral analysis of unevenly spaced data. *The Astrophysical Journal*, *263*, 835-853. https://doi.org/10.1086/160554

Scheeringa, R., Petersson, K. M., Kleinschmidt, A., Jensen, O., & Bastiaansen, M. C. M. (2012). EEG Alpha Power Modulation of fMRI Resting-State Connectivity. *Brain Connectivity*, *2*(5), 254-264. https://doi.org/10.1089/brain.2012.0088

Schneider, B., Szalárdy, O., Ujma, P. P., Simor, P., Gombos, F., Kovács, I., … Bódizs, R. (2022). Scale-free and oscillatory spectral measures of sleep stages in humans. *Frontiers in Neuroinformatics*, *16*. https://doi.org/10.3389/fninf.2022.989262

Schönauer, M., & Pöhlchen, D. (2018). Sleep spindles. *Current Biology*, *28*(19), R1129-R1130. https://doi.org/10.1016/j.cub.2018.07.035

Schönwald, S. V., de Santa-Helena, E. L., Rossatto, R., Chaves, M. L. F., & Gerhardt, G. J. L. (2006). Benchmarking matching pursuit to find sleep spindles. *Journal of Neuroscience Methods*, *156*(1), 314-321. https://doi.org/10.1016/j.jneumeth.2006.01.026

Seeley, W. W., Menon, V., Schatzberg, A. F., Keller, J., Glover, G. H., Kenna, H., … Greicius, M. D. (2007). Dissociable Intrinsic Connectivity Networks for Salience Processing and Executive Control. *Journal of Neuroscience*, *27*(9), 2349-2356. https://doi.org/10.1523/JNEUROSCI.5587-06.2007

Skrandies, W. (2007). The Effect of Stimulation Frequency and Retinal Stimulus Location on Visual Evoked Potential Topography. *Brain Topography*, *20*(1), 15-20. https://doi.org/10.1007/s10548-007-0026-1

Staresina, B. P., Niediek, J., Borger, V., Surges, R., & Mormann, F. (2023). How coupled slow oscillations, spindles and ripples coordinate neuronal processing and communication during human sleep. *Nature Neuroscience*, *26*(8), 1429-1437. https://doi.org/10.1038/s41593-023-01381-w

Steriade, M. (2006). Grouping of brain rhythms in corticothalamic systems. *Neuroscience*, *137*(4), 1087-1106. https://doi.org/10.1016/j.neuroscience.2005.10.029

Stevens, A., & Kircher, T. (1998). Cognitive decline unlike normal aging is associated with alterations of EEG temporo-spatial characteristics. *European Archives of Psychiatry and Clinical Neuroscience*, *248*(5), 259-266. https://doi.org/10.1007/s004060050047

Tallon-Baudry, C., & Bertrand, O. (1999). Oscillatory gamma activity in humans and its role in object representation. *Trends in Cognitive Sciences*, *3*(4), 151-162. https://doi.org/10.1016/S1364-6613(99)01299-1

Tarailis, P., Koenig, T., Michel, C. M., & Griškova-Bulanova, I. (2024). The Functional Aspects of Resting EEG Microstates: A Systematic Review. *Brain Topography*, *37*(2), 181-217. https://doi.org/10.1007/s10548-023-00958-9

Tchumatchenko, T., & Clopath, C. (2014). Oscillations emerging from noise-driven steady state in networks with electrical synapses and subthreshold resonance. *Nature Communications*, *5*(1), 5512. https://doi.org/10.1038/ncomms6512

Tomescu, M. I., Rihs, T. A., Rochas, V., Hardmeier, M., Britz, J., Allali, G., … Michel, C. M. (2018). From swing to cane: Sex differences of EEG resting-state temporal patterns during maturation and aging. *Developmental Cognitive Neuroscience*, *31*, 58-66. https://doi.org/10.1016/j.dcn.2018.04.011

Tomescu, Miralena I., Rihs, T. A., Becker, R., Britz, J., Custo, A., Grouiller, F., … Michel, C. M. (2014). Deviant dynamics of EEG resting state pattern in 22q11.2 deletion syndrome adolescents: A vulnerability marker of schizophrenia? *Schizophrenia Research*, *157*(1), 175-181. https://doi.org/10.1016/j.schres.2014.05.036

Tröndle, M., Popov, T., Pedroni, A., Pfeiffer, C., Barańczuk-Turska, Z., & Langer, N. (2023). Decomposing age effects in EEG alpha power. *Cortex*, *161*, 116-144. https://doi.org/10.1016/j.cortex.2023.02.002

Unser, M. A., & Blu, T. (1999). Construction of fractional spline wavelet bases. Dans M. A. Unser, A. Aldroubi, & A. F. Laine (Éds), (pp. 422-431). Communication présentée au SPIE's International Symposium on Optical Science, Engineering, and Instrumentation, Denver, CO. https://doi.org/10.1117/12.366799

Van De Ville, D., Britz, J., & Michel, C. M. (2010). EEG microstate sequences in healthy humans at rest reveal scale-free dynamics. *Proceedings of the National Academy of Sciences*, *107*(42), 18179-18184. https://doi.org/10.1073/pnas.1007841107

VanderPlas, J. T. (2018). Understanding the Lomb–Scargle Periodogram. *The Astrophysical Journal Supplement Series*, *236*(1), 16. https://doi.org/10.3847/1538-4365/aab766

Villar Ortega, E., Buetler, K. A., Aksöz, E. A., & Marchal-Crespo, L. (2024). Enhancing touch sensibility with sensory electrical stimulation and sensory retraining. *Journal of*

NeuroEngineering and Rehabilitation, *21*(1), 79. https://doi.org/10.1186/s12984-024-01371-4

von Ellenrieder, N., Frauscher, B., Dubeau, F., & Gotman, J. (2016). Interaction with slow waves during sleep improves discrimination of physiologic and pathologic high-frequency oscillations (80–500 Hz). *Epilepsia*, *57*(6), 869-878. https://doi.org/10.1111/epi.13380

von Ellenrieder, N., Gotman, J., Zelmann, R., Rogers, C., Nguyen, D. K., Kahane, P., … Frauscher, B. (2020). How the Human Brain Sleeps: Direct Cortical Recordings of Normal Brain Activity. *Annals of Neurology*, *87*(2), 289-301. https://doi.org/10.1002/ana.25651

Voytek, B., Kramer, M. A., Case, J., Lepage, K. Q., Tempesta, Z. R., Knight, R. T., & Gazzaley, A. (2015). Age-Related Changes in 1/f Neural Electrophysiological Noise. *Journal of Neuroscience*, *35*(38), 13257-13265. https://doi.org/10.1523/JNEUROSCI.2332-14.2015

Vysata, O., Kukal, J., Prochazka, A., Pazdera, L., & Valis, M. (2012). Age-Related Changes in the Energy and Spectral Composition of EEG. *Neurophysiology*, *44*(1), 63-67. https://doi.org/10.1007/s11062-012-9268-y

Wainio-Theberge, S., Wolff, A., Gomez-Pilar, J., Zhang, J., & Northoff, G. (2022). Variability and task-responsiveness of electrophysiological dynamics: Scale-free stability and oscillatory flexibility. *NeuroImage*, *256*, 119245. https://doi.org/10.1016/j.neuroimage.2022.119245

Wei, Y., Ramautar, J. R., Colombo, M. A., te Lindert, B. H. W., & Van Someren, E. J. W. (2018). EEG Microstates Indicate Heightened Somatic Awareness in Insomnia: Toward Objective Assessment of Subjective Mental Content. *Frontiers in Psychiatry*, *9*. https://doi.org/10.3389/fpsyt.2018.00395

Wen, H., & Liu, Z. (2016). Separating Fractal and Oscillatory Components in the Power Spectrum of Neurophysiological Signal. *Brain Topography*, *29*(1), 13-26. https://doi.org/10.1007/s10548-015-0448-0

Wendt, H., & Abry, P. (2007). Multifractality Tests Using Bootstrapped Wavelet Leaders. *IEEE Transactions on Signal Processing*, *55*(10), 4811-4820. https://doi.org/10.1109/TSP.2007.896269

Wendt, H., Abry, P., & Jaffard, S. (2007). Bootstrap for Empirical Multifractal Analysis. *IEEE Signal Processing Magazine*, *24*(4), 38-48. https://doi.org/10.1109/MSP.2007.4286563

Weng, L., Jülich, S. T., & Lei, X. (2025). Linear and nonlinear features of EEG microstate associated with insomnia. *Sleep Medicine*, *133*, 106645. https://doi.org/10.1016/j.sleep.2025.106645

Wiemers, M. C., Laufs, H., & von Wegner, F. (2024). Frequency Analysis of EEG Microstate Sequences in Wakefulness and NREM Sleep. *Brain Topography*, *37*(2), 312-328. https://doi.org/10.1007/s10548-023-00971-y

Wilson, L. E., da Silva Castanheira, J., & Baillet, S. (2022). Time-resolved parameterization of aperiodic and periodic brain activity. *eLife*, *11*, e77348. https://doi.org/10.7554/eLife.77348

Xu, J., Pan, Y., Zhou, S., Zou, G., Liu, J., Su, Z., … Gao, J.-H. (2020). EEG microstates are correlated with brain functional networks during slow-wave sleep. *NeuroImage*, *215*, 116786. https://doi.org/10.1016/j.neuroimage.2020.116786

Yuan, H., Zotev, V., Phillips, R., Drevets, W. C., & Bodurka, J. (2012). Spatiotemporal dynamics of the brain at rest — Exploring EEG microstates as electrophysiological signatures of BOLD resting state networks. *NeuroImage*, *60*(4), 2062-2072. https://doi.org/10.1016/j.neuroimage.2012.02.031

Zanesco, A. P., King, B. G., Skwara, A. C., & Saron, C. D. (2020). Within and between-person correlates of the temporal dynamics of resting EEG microstates. *NeuroImage*, *211*, 116631. https://doi.org/10.1016/j.neuroimage.2020.116631

Zeitlhofer, J., Anderer, P., Obergottsberger, S., Schimicek, P., Lurger, S., Marschnigg, E., … Deecke, L. (1993). Topographic mapping of EEG during sleep. *Brain Topography*, *6*(2), 123-129. https://doi.org/10.1007/BF01191077

Zerouali, Y., Lina, J.-M., Sekerovic, Z., Godbout, J., Dube, J., Jolicoeur, P., & Carrier, J. (2014). A time-frequency analysis of the dynamics of cortical networks of sleep spindles from MEG-EEG recordings. *Frontiers in Neuroscience*, *8*. https://doi.org/10.3389/fnins.2014.00310